THE PETROUS PORTION OF THE HUMAN TEMPORAL BONE:

POTENTIAL FOR FORENSIC INDIVIDUATION

A Dissertation

by

JASON MATTHEW WIERSEMA

Submitted to the Office of Graduate Studies of
Texas A&M University
in partial fulfillment of the requirements for the degree of

DOCTOR OF PHILOSOPHY

August 2006

Major Subject: Anthropology

THE PETROUS PORTION OF THE HUMAN TEMPORAL BONE:

POTENTIAL FOR FORENSIC INDIVIDUATION

A Dissertation

by

JASON MATTHEW WIERSEMA

Submitted to the Office of Graduate Studies of
Texas A&M University
in partial fulfillment of the requirements for the degree of

DOCTOR OF PHILOSOPHY

Approved by:

Chair of Committee,	Lori E. Wright
Committee Members,	Sheela Athreya
	Darryl de Ruiter
	Gary McCord
Head of Department,	David L. Carlson

August 2006

Major Subject: Anthropology

ABSTRACT

The Petrous Portion of the Human Temporal Bone:

Potential for Forensic Individuation.

(August 2006)

Jason Matthew Wiersema, B.A., Texas State University;

M.A., California State University, Chico

Chair of Advisory Committee: Dr. Lori E. Wright

In this dissertation I evaluate the potential of the morphology of the petrous portion of the human temporal bone as seen on axial CT scans of the head as a means to generate identifications of fragmentary human skeletal remains. The specific goals are threefold: (1) To investigate variability in the shape of the petrous portion of the human temporal bone using two-dimensional morphometric analysis; (2) to evaluate the reliability of the resultant method in forensic identification; and (3) to consider the results within the framework of Bayesian theory in light of recent rulings regarding the admissibility of forensic testimony.

The data used in this research were collected from axial CT images of the cranium. Two sets of images were collected for each of the 115 individuals in the sample so that Euclidean distance comparisons could be made between images of the same individual and images from different individuals. I collected

two-dimensional coordinate data from 36 landmarks on each of the CT images and calculated the distances between each of the coordinate points to generate the data used in the statistical analyses.

I pared down this set of measurements using two different models (referred to as the biological and PCFA models). The measurement sets of both models were then compared to one another using nearest neighbor analysis, to test their relative efficiency in matching replicate images to one another. The results of both models were highly accurate. Three incorrect nearest neighbor matches resulted from the biological model and 5 from the PCFA model. The errors appear to have been the result of variation in the axial plane between the first and second scans.

The results of the nearest neighbor comparisons were then considered within the context of Bayes' Theorem by calculating likelihood ratios and posterior probabilities. The likelihood ratios and posterior probabilities were very high for both models, indicating that: 1) there is significant individual variability in the measurements of the petrous portion used in this research, and 2) this variation represents a high level of potential accuracy in the application of this method in the identification of forensic remains.

ACKNOWLEDGEMENTS

I owe a large number of people a great deal of gratitude for their contributions to the success of this dissertation and to my graduate career. The members of my committee, Dr. Lori Wright, Dr. Sheela Athreya, Dr. Darryl de Ruiter and Dr. Gary McCord were obviously instrumental in the completing of this research, but also went far beyond what was required of them in offering assistance and guidance. Dr. Lori Wright deserves particular gratitude for her unwavering confidence and support of my progress. It was often her confidence that convinced me that I could proceed. Dr. David Carlson, the Chair of the Anthropology Department deserves many thanks. He was always eager and available to provide methodological and statistical assistance, and his input is evident throughout this dissertation. Dr. Gil Naul, Chairman of the Department of Radiology at Scott and White Hospital in Temple deserves thanks for providing me with the CT images on which my research was based and for making the process of acquiring those images significantly less complex than it would otherwise have been.

David Glassman, my mentor as an undergraduate, whose unique brand of honest advice is still spookily meaningful today, deserves much gratitude. Dr. Turhon Murad also has been the source of significant knowledge and advice over the years, and I thank him for that. I also wish to extend my gratitude to Dr Wei-Jung Chen, Associate Professor at the Texas A&M University Health

Science Center whose patience, as well as his professional and personal guidance during my employment in his laboratory made the last three years both more efficient and more enjoyable.

I would also like to thank Dr. Eric Bartelink for what, once again was the ideal environment in which to be a graduate student and write a dissertation. Again, nothing works like a little friendly competition to motivate me, or maybe it was guilt when he was working and I wasn't. Either way, it worked, thanks Fartolin. Cassady Yoder deserves thanks for her support during the process as we progressed through various stages of this process at the same time. Geoff Denny, my neighbor and friend, will take a long time to repay for all of his help. I extend my gratitude for his help with excel and SPSS, I'm not sure my computer would have survived without it. I'd also thank him also for the coffee, meals, and all of the various other things he did at just the right time to help me out.

To my mom and dad, thanks isn't enough, your moral support has been crucial during this process, especially when I wasn't sure I could finish. Oh, and thanks to them for bailing me out of my various monetary crunches over the years. Without their help, I would never have finished. Everyone should be so lucky as to have parents like mine. Thanks to my brother, Jared Wiersema for bragging on me all the time, it was nice to know I had him on my side. I also extend many thanks to Alanna Koos for her steadfast support, and periodic motivational speeches. I didn't want to listen at the time, but I'm glad I did now. I realize now, when I think of those speeches just how well she knows me.

TABLE OF CONTENTS

Page

CHAPTER Page

Page

LIST OF FIGURES

FIGURE Page

FIGURE Page

LIST OF TABLES

TABLE Page

CHAPTER I

INTRODUCTION

Personal identification is of primary importance in forensic investigations involving decomposed human remains. Frequent complications of the identification process can result from a vast number of taphonomic influences, particularly in mass disaster and human rights investigations. Remains are often heavily fragmented and commingled due either to myriad destructive circumstances in the case of mass disasters or by intentional efforts to hinder identification efforts in the case of human rights-related criminal activity.

The forensic scientist has at his/her disposal a variety of techniques which yield more or less definitive identifications, but these techniques are often vulnerable to taphonomic complications. For example DNA identification is generally preferred for individual identification, however, on many occasions it is not possible because the DNA has been destroyed by taphonomic influences, or because there is not an antemortem DNA sample to which comparisons can be made.

The literature is inundated with published attempts to find means of extracting diagnostic information directly from fragmentary skeletal remains. Most of these efforts have focused on developing methods from areas of the skeleton that are of known diagnostic significance. Unfortunately, the most

---

This dissertation follows the style of *American Journal of Physical Anthropology*.

individually diagnostic portions of the skeleton, such as the midface and frontal sinuses, are often those that are most susceptible to taphonomic destruction. Even dental remains are often not complete enough for identification due to destruction of the surrounding skeletal matrix. Thus, in spite of the efficacy of these techniques under ideal conditions, with the exception of dental remains, they are rarely of practical utility in mass disaster and human rights investigations.

A different approach is proposed here. Rather than further developing techniques for identification based on portions of the skeleton that harbor known diagnostic value in spite of their low representation in mass disaster, human rights and even archaeological settings, this investigation will focus on establishing the as yet undiscovered diagnostic value of a portion of the skeleton which most frequently survives taphonomic destruction.

The petrous portion of the temporal bone is widely considered to be the densest bony structure in the human skeleton (Shipman et al., 1985; Schwartz, 1995). The consequent resistance of the petrous portion to taphonomic destruction is broadly appreciated in the forensic (Kalmey and Rathbun, 1996; Noren et al., 2005), bioarchaeological (Waldron, 1987) and paleoanthropological literature (Kimbel et al., 1984; Kennedy, 1991; Aiello and Dean, 2002; Harvati, 2003). Although recently some scholars have begun to explore it superficially, little effort has been invested in extracting information of individually, sexually, or ancestrally diagnostic value from this portion of the skeleton.

The goals of this dissertation are threefold: (1) to empirically investigate variability in the shape of the petrous portion of the human temporal bone using two-dimensional morphometric analysis, (2) to evaluate the reliability of the resultant method in identification of individual remains, and to estimate the probabilities of identification and misidentification associated with it, and (3) to consider the utility of the method within the framework of Bayesian theory in light of recent rulings regarding the admissibility of forensic testimony.

This analysis is based on the morphometric comparison of the petrous portion of the temporal bone as seen on repeated axial CT images taken from 115 adult individuals (50 males and 65 females). The sample is composed of two images each taken from living hospital patients, with no visible signs of pathological change. These repeated scans serve as proxy ante- and postmortem imagery.

I collected two-dimensional coordinate data from each of the images, and converted the coordinates to distance data to circumvent problems associated with head movement in the collection of measurements directly from the images. The subsequent statistical analyses are based on the measurement distances rather than the coordinate data. I define 36 landmarks on the petrous part of the temporal bone. Though they demarcate named anatomical features, most of the landmarks have not been used in morphometric analyses of this type, and thus I assigned acronyms to them. Approximately 640 total distances connect these 36 landmarks, meaning that 640 measurements are available for the

development of a final measurement set with which the value of the petrous portion of the temporal bone as an identifier could be evaluated. I examine the repeatability of the measurements to evaluate the precision and reliability of both the landmark and distance data.

As in most research involving morphometric skeletal analysis, the bulk of the methodology employed in this dissertation is related to the selection of an appropriate measurement set to address this particular set of hypotheses. There is significant debate as to the most appropriate means to select phylogenetically meaningful sets of linear measurements of the cranium (Athreya and Glantz, 2003). The debate focuses on the relative importance of the statistical independence of cranial measurements and their biological relevance. Although the debate is focused on the implications of this dichotomy for the accuracy of statistical techniques that assume independence of the test variables (Athreya and Glantz, 2003), this is also an important concept in non-phylogenetic applications of cranial morphometrics, including the present one.

The goal of the present research is to select the most effective and efficient measurement set for use in the identification of unknown fragmentary skeletal remains. This requires the successful incorporation of biological characteristics of the petrous portion into a statistically discriminatory scheme. It has been demonstrated that the components of the skull traditionally thought to represent independent units of variation are in fact interrelated, both in the structural and developmental (Enlow, 1990), and statistical (Lande and Arnold,

1983; Winkler and Kirchengast, 1993) contexts. Thus, it is likely that the specific structural and developmental dimensions of the petrous portion also covary. If based solely on biological criteria selection of measurements for this research may preclude the extraction of statistically meaningful data, not because of a violation of the assumptions of a particular statistical technique, but rather because what are thought to be important biological distinctions may not be statistically meaningful. This is problematic considering that the method's accuracy is ultimately statistically-based. On the other hand, is it appropriate to select a set of measurements based solely on the results of a statistical analysis without regard to the biological characteristics of the petrous portion?

To address this issue, I developed two models of data reduction: (1) based on the developmental and structural characteristics of the petrous portion, and (2) based on principal components factor analysis of the entire measurement set. Each model is described in detail in Chapter V, as are the measurement sets that result from each. Finally, nearest neighbor comparisons of the summed measurement values for each individual were used to evaluate the relative accuracy of the two measurement sets in the association of ante- and postmortem CT images of the petrous portion.

Chapter II provides detailed background of the relevant legal and methodological issues in forensic identification with specific emphasis on the identification of fragmentary skeletal remains, and discusses precedents for the current research. Chapter III presents historical and technical background to CT

technology, its advantages, uses and limitations. It also describes the solutions to those limitations, and more specifically how I accommodate them in the current research.

Chapter IV describes the anatomy of the petrous part of the temporal bone and discusses the process by which the temporal bone evolved, and the ontogenetic influences according to which it varies. This chapter gives a basis for understanding the logic behind the landmark and measurement selection processes.

Chapter V discusses the materials and methods employed in the data collection process. Chapter VI describes the process by which I evaluate the repeatability of the data, as well as data reduction methodologies, and analyses of variation in the petrous portion related to sex, age, and the duration of time between scans. The results of these analyses are also presented in Chapter VI for the sake of continuity. The nearest neighbor analysis statistical design is presented in Chapter VII and the results are described in the context of likelihood ratios and posterior probabilities.

Finally Chapter VIII provides a detailed discussion of the results in the context of existing literature regarding Bayesian statistics and current law regarding the admissibility of forensic testimony. It also includes a discussion of the limitations of the method and details the directions for future research.

CHAPTER II

BACKGROUND OF FORENSIC IDENTIFICATION

Identification is one of the most significant contributions made by the forensic scientist. This is true in both small-scale homicide or accident investigations, and in investigations involving large numbers of human remains. Traditionally, forensic scientists have referred to two types of identifications – presumptive and positive– and this distinction has become more important with the recent increase in large-scale death investigations. Whereas the presumptive identifications of single individuals based on associated personal effects or general skeletal characteristics is often considered appropriate, identification by these means is often inappropriate or impossible in the case of large numbers of commingled and fragmentary remains. A good example of this is the identification of victims of the recent war crimes in Bosnia and Kosovo. The victim population was both commingled and homogenous: in Bosnia most of the victims buried in mass graves were men of European ancestry between 18 and 50 years old. These characteristics render presumptive identifications essentially useless. Simmons (2006) recently demonstrated that the practice of presumptive identification has led to large numbers of mis-identifications of the victims in both Bosnia and Kosovo. The issue is essentially that it is inappropriate to apply individual level techniques to a population level problem.

Mass disasters including aviation accidents and terrorist attacks also complicate presumptive identifications by fragmenting and commingling the remains of the victims. So, though the population may not be homogenous, most of the identifying characteristics have been sufficiently fragmented as to render them useless.

The forensic community is heavily invested in developing novel and robust techniques for positive identification in these contexts, and the law pertaining to forensic opinion has undergone a concomitant transformation. Identification techniques must now be scientifically and statistically robust and repeatable, rather than presumptive and may not rely solely on the discretion of the investigator.

The next section of this chapter discusses of the law as it pertains to the admissibility of scientific testimony, in particular testimony regarding forensic individuation. There is an intimate relationship between advances in the techniques of forensic identification and changes in the admissibility of scientific testimony, and the design of the current research is intended to satisfy the most current requirements of the law. A review of the existing literature in the field of forensic identification with particular attention to radiographic methods of identification follows and relevant research from outside of the forensic literature is also discussed.

FEDERAL GUIDELINES FOR THE ADMISSION OF FORENSIC EVIDENCE

Federal guidelines regarding the admissibility of forensic testimony have become more rigorous in recent years. For this reason, research in forensic identification is also undergoing a transformation that must be considered in the development of novel techniques. There has been a longstanding debate as to the admissibility of specific kinds of forensic evidence in court and the standards have varied in large part based on the Supreme Court's periodic response to the status quo.

The "Frye Rule" (1923) was the first effort on the part of the federal court system to standardize the admissibility of forensic evidence, while increasing objectivity in forensic testimony. The rule simply stated that any scientific evidence presented "must have gained general acceptance in the particular field in which it belongs" (Frye, 1923), and it stood for decades as the standard for the acceptance of forensic evidence, in large part because of its ease of application. However, interpretation of the ruling was historically variable, and this eventually led to the enactment of the *Federal Rules of Evidence* in 1975. These rules stood as the first standardized set of guidelines for the use of forensic evidence in criminal testimony, and stated:

> If scientific, technical, or other specialized knowledge will assist the trier of fact to understand the evidence or to determine a fact in issue, a witness qualified as an expert by knowledge, skill, experience, training or education may testify thereto in the form of opinion or otherwise (Federal Rules of Evidence, 1975).

The language of this ruling still clearly permitted considerable subjectivity in its interpretation. For instance, the *Frye* standard was not mentioned in the *Rules of Evidence*, and confusion arose as to the relative jurisdiction of the two rulings.

In 1993 the *Daubert vs. Merrell-Dow Pharmaceuticals* case exposed these contradictions and precipitated a further judgment of the Supreme Court. The case specifically addressed the issue of whether or not the *Federal Rules of Evidence* superceded the *Frye* ruling. Ultimately the court ruled that: (1) the Rules of Evidence did in fact supercede Frye, and that (2) a singular acceptance rule was not appropriate because it precluded legitimate minority opinion in the form of emerging scientific research. In addition, the court emphasized the application of the language of *Rule 702* of the *Federal Rules of Evidence* in establishing the standard for admissibility of forensic evidence. *Rule 702* states that scientific knowledge: (1) must be based on the scientific method, rather than subjective belief or speculation, and (2) must be relevant to the current scientific inquiry (*Daubert vs. Merrell-Dow,* 1993).

The court established a series of guidelines for satisfying the requirements of *Rule 702*. The first of these guidelines is that the content of forensic scientific testimony must be testable by the scientific method. The second guideline requires that the opinions presented in scientific testimony have been peer reviewed, that is, published in a peer-reviewed journal. Thirdly the guidelines require the association of established reliability and error rates

with forensic scientific testimony. The fourth guideline is vague in its language, and simply requires that methods or opinions presented in scientific testimony have achieved general acceptance within the relevant scientific community.

The most recent ruling with regard to the admissibility of forensic scientific testimony was made in 2000 and is an amendment to the *Federal Rules of Evidence.* This amendment reads:

> If scientific, technical or other specialized knowledge will assist the trier of fact to understand the evidence or to determine a fact in issue, a witness qualified as an expert by knowledge, skill, training or education may testify thereto in the form of opinion or otherwise, *if (1) the testimony is based upon sufficient facts or data, (2) the test is the product of reliable principals and methods, and (3) the witness has applied the principals and methods reliably to the facts of the case* (emphasis added to signify amended portion) (Amendment to Federal Rules of Evidence, 2000).

Whereas traditional forensic testimony was based on the assumption of "discernible uniqueness" and the idea that the trained eye can distinguish individual differences, the Daubert ruling instead requires that a scientific technique or method not be considered admissible unless it is "generally accepted as reliable in the relevant scientific community" (Saks and Koehler 2005: 892). To achieve this acceptance, it must have been published and peer reviewed and represent something other than the opinion of a single expert.

Implicit in this transformation of the rules of forensic testimony is the assumption that methods will not achieve "general acceptance" without demonstrable objectivity, generally in the form of rigorous statistical evaluation, and presentation of associated reliability and error estimates. The specific

implication of this ruling with regard to the admissibility of techniques of forensic identification is that it is no longer sufficient to simply submit, based on opinion, that the variation that characterizes a particular biological characteristic is sufficient to preclude confusion of its configuration between individuals. The courts now require rigorous demonstration of these opinions.

United States vs. Plaza (2002) stands as the most visible of the cases in which the Daubert guidelines have influenced the proceedings of a federal court case. The judge in this case suggested that the technique used for fingerprint identification in the case did not meet the Daubert requirements. The evidence was eventually admitted, but the case represents a significant precedent considering the longstanding role of fingerprint examination as the "gold standard" for forensic identification.

METHODS FOR PERSONAL IDENTIFICATION OF HUMAN REMAINS

Personal identification has become important in a variety of research contexts. Novel techniques for the identification of the living and of the dead are published routinely in an array of journals ranging in interest from biometrics to forensic anthropology. Unfortunately, little overlap exists between the varied perspectives. For example forensic scientists have not capitalized significantly on the development of algorithms and other methods aimed at identifying unknown living individuals by biometrics researchers. This research is relevant in that it provides methodological precedents for achieving the rigorous standards of admissibility required by the courts in recent years. The remainder

of this chapter reviews recent publications in forensic identification and biometrics, and discusses their relevance to the current research.

TECHNIQUES FOR RADIOGRAPHIC IDENTIFICATION FROM THE SKELETON

The most direct precedent for the present work lies in the widespread use of conventional radiography, and the more limited use of CT and MRI imaging in the identification of individual remains. There is a long and extensive history of the application of radiography in the identification of decomposed human remains. The vast majority of radiographic identifications are made using x-rays of the dentition, but numerous publications describe individual identifications made using radiographic imaging of various other parts of the postcranial skeleton including the leg and foot (Owsley and Mann, 1989), pelvis (Moser and Wagner, 1989; Owsley and Mann, 1992), and the hand and wrist (Greulich, 1960), as well as features of the cranium, including the mastoid sinuses (Rhine and Sperry, 1991), nasal sinuses (Culbert and Law, 1927), cranial suture patterns (Chandra-Sekharan, 1985), and frontal sinuses (Mayer, 1935; Schuller, 1943; Asherson, 1965; Ubelaker, 1984; Yoshino et al., 1987; Reichs and Dorion, 1992; Reichs, 1993; Christensen, 2004).

The frontal sinuses have received considerable attention as a highly variable and individualistic character of the human skull (Mayer, 1935; Schuller, 1943; Asherson, 1965; Ubelaker, 1984; Yoshino et al., 1987; Reichs and Dorion, 1992; Reichs, 1993) and are of the most relevance to this investigation. Articles

discussing the radiographic evaluation of the frontal sinuses in personal identification have been published on several occasions (Mayer, 1935; Asherson, 1965; Camps, 1969; Ubelaker, 1984; Marlin et al., 1991). However, the majority of these publications are case reports and they do not present techniques for future application, nor do they satisfy the requirements of the Daubert guidelines. For example, Quatrehomme and Fronty (1996) suggests simple superimposition of ante-and postmortem conventional radiograph images as a viable technique for personal identification from the frontal sinus. He acknowledges the considerable difficulty associated with the correct orientation of the skull for postmortem imaging, but does not address the subjectivity associated with the method. Quatrehomme and Fronty's method is typical of these articles, which present a case, or series of cases, in which "identifications" were made based on matches perceived by the observer (Mayer, 1935; Ubelaker, 1984; Marlin et al., 1991).

Kirk et al. (2002) published the results of a survey of 39 cases in which identifications were made in Ontario, Canada, based on non-metric comparison of frontal sinus configuration. Only three of the 39 cases were considered unidentifiable using the frontal sinus because of poor film quality and the remaining 36 produced "conclusive postmortem to antemortem pattern matches" (Kirk et al., 2002: 318). The identifications were made based on uniqueness, as perceived by the viewer, between superimposed ante- and postmortem antero-posterior radiographs of the skull. They also refer to the "quantitative"

association of sixteen cases. This quantification involved measurement of the maximum vertical and horizontal dimensions of the sinuses. “Any discrepancy between antemortem and postmortem values greater than 5mm was classified as a metric nonmatch” (Kirk et al., 2002). Although less subjective than the identifications made solely on the basis of simple superimposition of ante and postmortem imagery, this technique is hardly quantified in terms of providing statistical information as to the strength of the associations or error rates associated with its use.

More comprehensive systems for classifying and/or identifying crania according to variability of the frontal sinuses have been presented by Yoshino et al. (1987), Yoshino et al. (1989), Schuller (1943), Reichs (1993), and Reichs and Dorion (1992). Yoshino et al. (1987) developed a potentially repeatable methodology for personal identification from conventional radiographs of the frontal sinuses. The method involved the development of a code number from the classification of six independent characteristics of the frontal sinuses. Based on the categorization of the asymmetry between the left and right sinuses, the superiority in size of one side over the other, the outline of the superior borders of the sinuses, the number of partial divisions of each sinus, and the number of supra-orbital cells, the code was a series of numbers that was statistically unlikely to be derived from more than a single individual by virtue of its length and the number of possible combinations represented by all of its possible variations. Yoshino used the skulls of 35 Japanese adults (21 males and 14

females) to develop the technique. They tested the technique on a single forensic case and concluded that the technique is of “considerable value in cases in which dental remains are not available” (Yoshino et al., 1987: 298).

Reichs and Dorion (1992) and Reichs (1993) modified this technique for use with axial CT scans of the skull. Their argument is essentially that future use of CT imaging will far outweigh the use of fronto-occipital radiographs, and that identification techniques based on radiographs will someday become obsolete. Thus instead of conventional radiography, they developed a method similar to that of Yoshino et al. (1987) using axial CT imaging. They evaluated a slightly different series of characteristics than Yoshino et al. (1987) that were more effectively imaged on CT scans, including bilateral dimension, bilateral asymmetry, superiority of side, distribution of partial bony septations, number of partial bony septations, distribution of complete bony cells, and number of complete bony cells. They suggested that scoring these attributes on several consecutive CT slices added to the length of the code derived, and therefore, to its statistical uniqueness. Unfortunately, neither Reichs and Dorion (1992) nor Reichs (1993) tested the method with a sample large enough to provide meaningful optimism for its future utility.

PROBLEMS WITH EXISTING RADIOLOGICAL METHODS

There are a number of problems that plague attempts to use radiographs in the identification of fragmentary remains. The first is the lack of antemortem radiographs to which comparisons of surviving elements can be made, and the

inverse low survival rate of those elements for which antemortem radiographs do frequently exist. The question is twofold: (1) with what regularity can one expect to find radiographic images that portray a particular portion of the skull sufficiently, and (2) do the elements for which there are commonly radiographs available provide the investigator with useful information? The frontal sinus region, for example, is demonstrably useful as a means to identify individuals from skeletal remains, and fronto-occipital radiographs of them are fairly common, but it is also a region of the skull that is not particularly resistant to taphonomic destruction.

The second problem is repeatability. Repeatability is dependent on the objectivity of the methodology employed, and objectivity is difficult to establish when using methods dependent on the investigator's individual assessment of subjective characteristics, such as a particular shape, level of symmetry, or side dominance. For example, the features of the frontal sinuses evaluated in the publications by both Yoshino et al. (1987) and Reichs and Dorion (1992) are arbitrary at best. There is a need for more easily reproducible character evaluations. Some authors have tried to increase the objectivity of radiographic methods by various means. As mentioned above, Kirk et al. (2002) attempted to add quantitative robusticity to the radiographic analysis of frontal sinuses by recording the maximum width and length of the sinuses in a sample of 39 crania, in addition to the more subjective variables used in other investigations. Reipert et al. (2001) completed an investigation that aimed to "improve the objectivity of

X-ray comparison for the identification of unknown individuals" by using a computer program named FoXSIS to reduce subjectivity in the analysis of the frontal sinuses. CT data were collected for 30 skulls, and using the FoXSIS program, were converted to virtual X-ray representations of the skulls. According to the authors, the primary advantage of the program was that its use of digital measurements of the features of the skull allowed for a quantification of the "probability of identity" without reliance on the more subjective, and less repeatable measures of identity such as side dominance, shape, and symmetry levels.

There is also a problem with techniques that are based on the assumption that it is statistically improbable for two individuals to have the same or similar codes just because there are a large number of possible combinations. This is problematic (at least with the techniques outlined above) because no effort is made to weigh the various characters relative to one another. For example, it is much more likely for an individual to have a single or very few septations of the frontal sinus than for them to have six or seven, thereby increasing dramatically the statistical probability that two individuals may indeed have the same code for that particular trait. This is a problem with many of the characteristics considered by both Reichs (1993) and Yoshino et al. (1987).

Christensen (2004) published the most objective and statistically robust analysis of the frontal sinuses to date. She used elliptical Fourier analysis (EFA), a geometric morphometric technique that imposes a set of coordinate

data points to a closed curve, to quantify the superior border of the frontal sinuses. The coordinate data were then used to quantify the outlines by generating a set of coefficients that represent a numerical reproduction of the curve. She traced the superior border of the frontal sinuses of 808 individuals and "closed" the curve inferiorly by connecting the inferior-most extensions of the left and right sides of the curve with a straight horizontal line. The Euclidean distances between the EFA generated outlines were compared as a means to test the accuracy with which they could be used to associate the correct images. The Euclidean distances between repeat images from the same individual were significantly smaller than the distances between individuals. She used typicality statistics to evaluate the statistical strength of the associations with good results. The probability of making an incorrect association between two outlines using her method is very small, and she concludes that "there is a quantifiable and significant difference between the shapes of individual frontal sinus outlines" (Christensen, 2004: 291). This research is the first in the long history of articles evaluating the frontal sinus that makes an attempt to satisfy the requirements of the Daubert guidelines.

NON-RADIOGRAPHIC IDENTIFICATION METHODS

Research in fields outside of the forensic sciences, including biometric research, is relevant to and potentially useful in advancing the field of forensic identification. In the classic sense, the term biometrics refers broadly to research concerned with the development of statistical methods pertinent to data

analysis problems in any of the biological sciences. Statistical methods for the analysis of data from sources varying from human clinical trials, to epidemiology, to agriculture fall within the realm of classical biometric research. More recently, and particularly since September 11th, 2001, the term has acquired another meaning, referring specifically to the emerging field that is devoted to the development of technologies aimed at the identification of living individuals using individually variable biological traits, including fingerprints, hand shape, retinal, and/or iris patterning and facial shapes.

When broadly considered, there are a number of concepts that are basic to research in biometric recognition that are of theoretical and practical relevance to forensic identification, particularly with regard to meeting the requirements of the Daubert guidelines. For example, the distinction between identification and verification is important in biometric recognition. Whereas identification implies the attachment of an identity to a particular set of data without any expectation as to who the data represent, verification involves, as the name implies, confirmation that a particular set of data is correctly associated with a suspected identity. This is a distinction that is of considerable relevance in forensic science. Similarly, classification of a particular data set to reduce the sample to which it requires comparison is common in biometric recognition, and normally precedes identification. For example, classifying an unknown fingerprint image as a whorl, loop or arch prior to identification minimizes the comparative sample, reduces error risk, and reduces the

statistical power necessary to make subsequent identification by excluding a large proportion of individuals. This concept also holds considerable potential usefulness in forensic identification.

Methodologically, biometric researchers adhere to a useful set of guidelines according to which one can evaluate the value of a potential biometric identifier. Some of those guidelines are also meaningful to forensic identification of the type proposed here. According to Maltoni et al. (2003), a viable identifier must be:

(1) universal: meaning that all individuals must have the identifier;

(2) distinctive: meaning that all persons must retain a individual variant of the biometric;

(3) permanent: meaning that the identifier must remain reasonably unchanged over time, and;

(4) collectible: meaning that the identifier must be quantifiable so as to facilitate efficient and unbiased comparison.

Additionally, the biometric identifier must achieve a level of statistical robusticity sufficient to allow reasonable confidence in its reliability and effectiveness (Maltoni et al., 2003).

Much of the process of fingerprint identification is analogous to the process by which identifications are made based on comparisons of ante- and postmortem radiographic images, in that fingerprint images of known individuals are compared to the image taken from the remains of an unknown individual who is either living or dead, and involves the identification and comparison of

analogous features between the image sets. There are three competing approaches to fingerprint identification in biometric research:

(1) correlation-based matching, which involves the superimposition of two images and the correlation between the analogous discrete characters. The correlations are then computed to correct for a variety of different displacements and rotations,

(2) ridge and feature-based matching: a technique which is generally used in cases where image quality is poor, and which involves the use of more complex, and more error prone algorithms based on ridge and feature shapes, rather than discrete points, and

(3) minutiae-based matching: which involves extraction of minutiae (discrete characteristics) from the fingerprints to be compared. The minutiae are then stored as two independent sets of points in the two dimensional plane. Ultimately the process involves finding the alignment of the two images that allow for the matching of the greatest number of minutiae.

Each of these three approaches has advantages in different contexts, but the minutiae based matching approach is the most amenable to testing in this investigation for several reasons. First, it is based on the collection of two dimensional coordinates of discrete points; second, it is best suited to comparisons between incomplete images and images whose characters do not overlap entirely; and third, it is the methodology that has long been used by forensic fingerprint examiners and stands as the standard according to which fingerprint evidence is accepted in courts of law.

Consideration of minutiae-based fingerprint matching techniques

Every fingerprint matching problem involves the comparison between a template and input fingerprint (Maltoni et al., 2003). Minutiae-based matching

techniques involve the representation of the images to be compared as feature vectors (one dimensional arrays) whose elements are the fingerprint minutiae. These vectors are simplified representations of the otherwise complex fingerprint images based on a few points rather than the entire range of detail, and result in less error from extraneous detail. Each minutia essentially represents a location in space, and this location is generally represented as a triplet $m=\{x,y,\theta\}$, where x and y represent the two dimensional coordinates and θ would represent the minutia angle. For the sake of this investigation, x and y would represent the two-dimensional coordinate of a particular characteristic of the petrous temporal bone in a CT film, and θ would represent the character angle, rather than the minutiae angle. Figure 1.1 is a graphic illustration of fingerprint minutiae. The circles represent the x and y coordinate of individual minutiae and the lines emanating from the circles represent the minutia angle (θ).

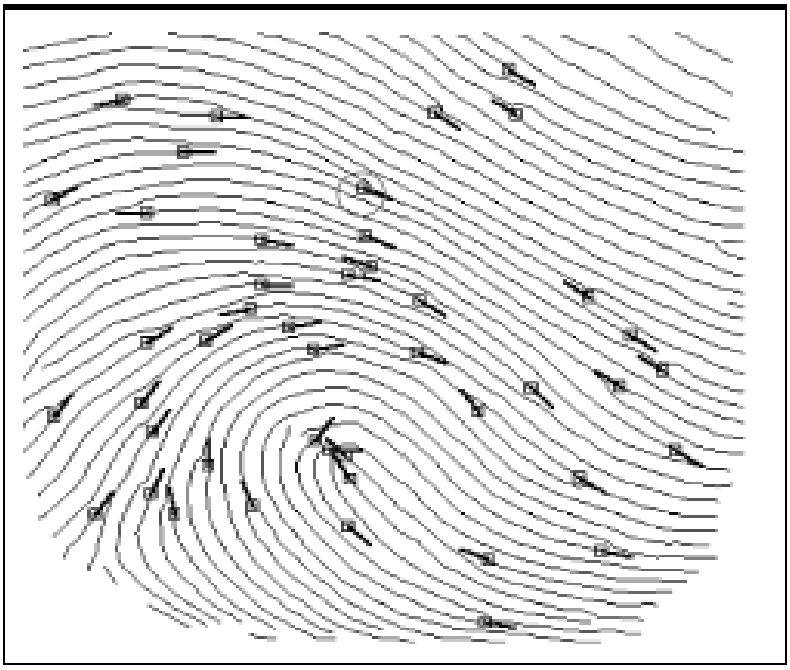

Figure 1.1. *A graphic representation of a series of minutiae on a fingerprint image.*

To apply this model to radiographic comparison, the ante- and postmortem images are compared in the same way as fingerprint images. If the antemortem image is designated as A, the postmortem image as P, and the individual characters to be compared, as c, the problem is then best represented as:

$$A=\{c_1, c_2,.....c_a\}$$

$$P=\{c_1, c_2,....c_b\}$$

where a and b represent the number of characters in the ante and postmortem images respectively. Each character is defined as: $c_1 =\{x_1, y_1, \theta_1\}$ for example. Two characters are considered to "match" if the character distance between

them (cd) is smaller than a particular threshold value c_o, and the difference between the angles (ca) of the two characters is smaller than an angle threshold (a_o). In the following equation, c_q and c_r represent individual characters for which a potential match is being evaluated (Maltoni et al., 2003).

Thus the two characters, c_q and c_r match if these requirements are met:

$$cd(c_q, c_r) = \sqrt{(x_q-x_r)^2+(y_q-y_r)^2} \leq a_o, \text{ and}$$

$$ca(c_q, c_r) = \min(|\theta_q - \theta_r|, 360^o - |\theta_q - \theta_r| \leq \theta_o$$

A number of equations can be used to verify a match, which are intended to correct for issues of image orientation and distortion, problems which are of much lesser concern in CT image matching than in fingerprint matching.

Discussion of models for identification based on facial geometry

Face recognition research has become increasingly prevalent in recent years with the advent of computer imaging and funding in response to terrorist attack. There are three main components that are nearly pervasive in the existing methods of facial recognition: the model, the normalization/subspace correction method, and the particular classifier that is employed. Two broad types of models predominate in face recognition research; eigenface models and statistical appearance models. The eigenface models use principal components analysis to convert a complex multidimensional facial image to a lower dimensional feature special representation of the image. The resultant algorithms are based on vector representations of facial images. These vector -

based images are then converted to lower dimensional subspaces which, as less complex representations of the human face, are less susceptible to intra-class variation. These statistical appearance models are more shape dependent, and as such are more subject to error and are likely unnecessarily complex for adaptation to this investigation.

CHAPTER III

BACKGROUND OF COMPUTED TOMOGRAPHY

The utility of a particular medium in the identification of individual skeletal remains is directly related to the availability of that medium, in other words the likelihood that antemortem data will be available for comparison to the same type of evidence collected from the deceased. In its various forms, radiography is frequently used in the diagnosis of a myriad of diseases, and for this reason, has become increasingly common in the antemortem record. In recent years, the invention of new radiographic modalities has increased the ease and accuracy with which various clinical diagnoses can be made, and there has been a concomitant increase in the employment of these radiographic techniques as means to make forensic identifications.

However, the petrous part of the temporal bone has been the subject of surprisingly little research as far as development of techniques for individual identification using radiographic imagery. At least in part, this is due to its relatively poor representation on most types of radiographic imagery. In recent decades, however, a variety of imaging modalities have become available for use in clinical evaluation of the petrous part of the temporal bone, including polytomography, angiography, magnetic resonance imaging (MR), and computed tomography (CT). Portions of the petrous part of the temporal bone

are also seen incidentally on radiographs intended to portray other portions of the skull or cervical spine.

The most significant problem associated with the use of plain radiographic imaging of the petrous portion of the temporal bone is related to the properties of the x-ray beam that passes through the skull, and the composition of the image that results. Unlike, CT and MR imagery, the images resulting from plain radiography are not cross-sectional, and as a result, the features through which the x-ray beam passes appear superimposed. This complicates the visualization of small individual features. It has also been demonstrated that abnormalities seen on plain radiographs often correlate poorly with the actual dimensions of intracranial abnormalities (Schaffer et al., 1980; Taylor, 1982; Virapongse et al., 1982). For these reasons, conventional radiography has largely been replaced by MRI and CT as the most frequently used techniques in cranial imaging, and is limited presently, to use in diagnosing acute sinusitis and cranio-facial trauma, both of which are better demonstrated with CT when available.

Computed tomography scanning provides the most accurate graphic representation of bony and air space anatomy and has also replaced polytomography in imaging of soft tissue abnormalities because of its lesser susceptibility to artifact and greater image accuracy. Another advantage of CT imaging is the decreased level of radiation to which it exposes patients, particularly the lenses and globes of the eyes. It is the imaging superiority of CT

under a variety of circumstances that has resulted in an exponential increase in its usage relative to other radiographic modalities, and a consequent increase in its pervasiveness in the antemortem record. The result is a considerable and ever increasing number of antemortem CT images that a forensic scientist can expect to be available for comparison. The typical hospital in a moderate sized city performs between 30 and 50 routine head CT scans per week (Dr. Gill Naul, personal communication). This chapter will: (1) define CT technology, both mechanically and historically, (2) discuss the advantages of CT relative to other modalities, both in the clinical and forensic settings, (3) discuss its limitations, (4) outline the solutions to those limitations, and finally, (5) relate the advantages and limitations of its use in the forensic sciences generally, and the present research specifically.

Computed tomography (CT) was invented in 1972 by British engineer Godfrey Hounsfield of EMI Laboratories, England, and independently by Allan Cormack of Tufts University during the same year (Haaga et al., 1994). The earliest CT systems were dedicated to head imaging only and "whole body" systems with larger patient openings became available in 1976. CT was widely available by about 1980. As in traditional radiography, CT employs ionizing radiation, projected through the body onto a photographic plate. The CT apparatus, however, allows for the acquisition of images from many different angles. CT scans result in digital data, which are then processed by a computer and used to create cross-sectional images of selected body tissues, organs, or

bones. Early CT systems often required several hours to assemble a single image, and these images were restricted to the axial (horizontal) plane of the body. This is the derivation of the original term Computed Axial Tomography or "CAT scan". Modern CT scanners are much faster, and provide images of far greater detail. The first CT scanner developed by Hounsfield in his lab at EMI took several hours to acquire the raw data for a single scan or "slice" and took days to reconstruct a single image from this raw data. The latest multi-slice CT systems can collect up to 4 slices of data in about 350 ms and reconstruct a 512 x 512-matrix image from millions of data points in less than a second (Kalendar, 2006). An entire chest (40 8 mm slices) can be scanned in five to ten seconds using the most advanced multi-slice CT system (Kalendar, 2006).

The CT scanning process consists of moving the CT apparatus around a stationary patient by means of a mobile table, which moves the patient through a circular shaped scanner (Kalendar, 2006). The scanning portion of the machine is then rotated around the selected portion of the patient's body. The CT apparatus rotates a narrow x-ray beam around a stationary patient, and the portion of the x-ray energy transmitted through the body is quantified on the opposite side of the body. Tissues of the body absorb variable amounts of energy based on their physical properties, particularly density. The apparatus uses a series of simultaneous mathematic equations to quantify the amount of x-ray energy absorbed by each of the tissue areas. A numerical density value is attributed to each volume unit. These densities are then translated by digital-

analog converter from numerical units into shades along a gray scale. CT slices through the body consist of collections of large numbers of these units according to the pattern represented by the variation in tissue densities within the area exposed to radiation within that slice. Slice thickness can typically vary from 1.5 to 10mm based on the clinical goal of the scan (Hsieh, 2003). Conventional CT technology typically requires several seconds for the acquisition of the slice and for the subsequent computer interpretation. Newer technologies are making the process considerably shorter, which by minimizing artifacts related to patient movement, enhances both the comfort of the patient and the quality of the images (Kalendar, 2006).

The resultant data are adjusted according to specific parameters called "windows." The term window refers to the range of grey shades incorporated into an image. Adjustment of the window settings allows for the better visualization of variable tissue types. This process is discussed in detail in later paragraphs. The cross sectional images that result are then interpreted by a radiologist, either on printed films or on digital computer images. The higher resolution and enhanced diagnostic utility that result constitute the main advantage of computed tomography over traditional x-ray technology. The use of a cross sectional perspective allows the doctor to more accurately locate an injury or tumor in relation to the surrounding anatomy, and to more accurately estimate its size and severity. Another advantage of CT technology is the ability to visualize a variety of tissue types on a single image, including bones, soft

tissues and blood vessels. This enhanced detail often eliminates the need for invasive exploratory surgery and surgical biopsy.

Computed tomography usage is generally divided into two categories, CT of the head and CT of the body. The uses of body CT vary widely and include cancer diagnosis, diagnosis and treatment of spinal problems, evaluation of skeletal injuries, measurement of bone mineral density for the detection of osteoporotic bone loss, identification of traumatic injuries to internal organs, and the diagnosis and treatment of vascular diseases. Head CT is used in a variety of diagnoses, including recognizing blood clots, detecting some varieties of brain tumors, diagnosis of problems associated with the eyes and the optic nerves, detecting fractures of the bones around the eyes or foreign objects in the eye, evaluating cranial sinuses for inflammation or other changes, investigating problems associated with the bone and joints of the temporomandibular joints, detection of enlarged brain cavities, locating potential skull fractures, identifying brain damage resulting from traumatic injury, and finally, in investigating the petrous part of the temporal bone as related to middle ear and auditory nerve problems. CT provides information that aids in the evaluation of symptoms such as confusion, paralysis, numbness, vision problems, vertigo or headaches that might indicate a brain injury, brain tumor, aneurysm, or bleeding within the skull. If bleeding is known to have begun, CT is also useful in assessing its severity, and the prognosis of potential surgical intervention. CT is also routinely used to

evaluate the extent of damage caused by a stroke and to determine the effectiveness of stroke treatment.

CAPABILITIES AND LIMITATIONS OF COMPUTED TOMOGRAPHY

A working understanding of the capabilities and parameters of CT technology is a prerequisite to its effective usage as a tool for forensic identification. Correct interpretation of CT imagery is contingent upon detailed knowledge of both the usage parameters and the characteristics of the resultant image. The image produced by a computed tomography apparatus is essentially a dense series of absorption values that appear on the image as a "grid of evenly spaced squares, the vertical and horizontal lines being the matrix size" (Hounsfield, 1976: 3). As with any digital modality, the image produced by a CT scanner is comprised of an array of a limited number of picture units, and as in all digital imagery, these units are referred to as pixels. Each pixel is the two dimensional representation of a specific unit of volume that is referred to as a voxel. Modern medical CT scanners develop images with a matrix of pixels that is of fixed size.

The pixel size can be varied based on the field of view (FOV), i.e. the area encompassed by a particular image. As a result, each voxel varies based on the pixel size and the thickness of the image slice. The pixel size determines the x and y dimensions of the voxel, and the slice thickness represents its size in the z dimension. Zoom reconstructions are often used in imaging of detailed morphology. Zoom reconstructions involve decreasing the size of the field of

view, and allow reduction of the pixel size to half of the spatial resolution or less, thereby preventing the pixel size from limiting the image resolution. Exploratory scans of the complete cranium are best seen with a matrix size of 512x512 pixels, a relatively small field of view of 102x102mm or less, and typically 5mm axial slices. The scans in this research were taken according to these parameters. Typical head scans are used to locate small tumors or fractures, and as a result, reduction of picture grain is of primary concern. Small matrix settings are best for visualizing soft tissue anomalies, whereas a larger matrix (512x512) is better suited for the visualizing bony detail, as in the inner and middle ear areas of the petrous temporal bone. The scans used in this research were taken according to these latter parameters.

A CT number is associated with every pixel. The CT number is the unit of measure of the average density in the voxel. The density is referred to as the attenuation coefficient. CT numbers are expressed as measurements on a scale of 4096 Hounsfield units (H). The Hounsfield scale is defined as the series of values between –1000H, the value for air, and the maximum of 3095 H, for very dense tissues like dental enamel. Water has a Hounsfield value of zero for reference. In order to produce an image from a matrix of CT numbers, each value in the scale is manifest visibly as a separate shade of gray. Since the human eye is not capable of distinguishing 4096 shades of gray, the 4096 shades are reduced to 256 shades by adjusting the window width. Again, window width adjustments involve adjustment of the number of shades of gray

incorporated within an image to maximize the visibility of the density variation in the image. Window width adjustments are made based on both the density of the tissues to be imaged, and their relationship to one another. Greater image clarity can be achieved with effective application of window width parameters. Large window widths are used when there are significant density differences between closely located tissues such as is the case between the brain and cranial bones in head CT. This is because the intermediate shades will give greater detail regarding the actual tissue interface. In the case of images of areas of the body with tissues of similar density, it is best to limit the window width so as to use all of the shades of gray to maximize the density variation within each tissue type, by incorporating fewer shades into the tissue interfaces.

Tissues with CT numbers that are outside of the range set by the window width appear as either white or black areas depending on whether they fall above or below the selected thresholds. The window width can be adjusted by the viewer to determine the setting that facilitates the best visualization of the desired tissues.

CT imaging of the skull varies relative to the symptoms it is being used to diagnose. “The ability of CT to show intracranial lesions has been its first and most important contribution to diagnostic imaging” (Phelps, 2003: 1597). Generalized symptoms require a generalized diagnosis, thus CT is often used as a means to search out lesions causing a variety of symptoms including dizziness, vertigo, non-specific pain, and potential cranial fracture. The temporal

bone is often included incidentally in these images. CT is also often used specifically to image the petrous temporal bone itself in diagnosing inner ear, cranial nerve, mastoid sinus, and/or temporo-mandibular joint problems. CT scans are useful in imaging of the temporal bone itself because a series of thin sections, 1-2mm in thickness combine to form a three dimensional representation that provides a comprehensive illustration of the small and often closely associated structures of the inner ear, as well as the arrangement of the vascular constituents of the petrous portion.

Scans intended to focus specifically on the petrous temporal bone are typically taken at a high window setting between 3000 and 4000HU, and are developed using an algorithm designed to best capture bony detail. The typical CT inspection of the petrous temporal bone begins with a lateral scout view, which helps the radiographer orient the CT beam in relation to the structures to be imaged. Most examinations of the skull, including those of the petrous bone are taken in the axial plane. This facilitates a view of the desired structures with the least obstruction and affords the patient the greatest level of comfort. In the interest of minimizing the exposure of the eyes to radiation, the axial plane has been modified from its strict definition. The orbitomeatal baseline is a standard craniometric reference plane passing through the right and left porion and the left orbitale; drawn on the profile radiograph from the superior margin of the acoustic meatus to the orbitale, the inferior-most point on the eye orbit. The

axial plane employed in CT imagery is instead 30° from the radiographic baseline, and is illustrated in Figure 3.1.

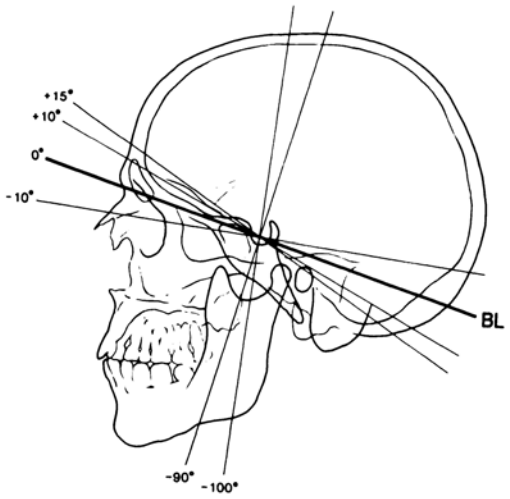

Figure 3.1. *Illustration of the axial plane as use in CT (BL).*

Morphometric uses for CT

CT usage extends beyond qualitative uses and into quantitative ones, with its application as a morphometric tool in both clinical and anatomical research. This research involves extracting of measurements between different landmarks, and in the case of medicine, of the size of anomalous tissues. The accuracy of the measurements taken from CT images is of obvious importance for the accurate interpretation of CT data, and a considerable body of literature is concerned with this issue. Much of the research regarding the accuracy of CT measurements involves the use of “phantoms.” Phantoms are models of known density that are scanned as a means to make inferences about the potential

result of scans of biological material of similar density. This research is intended to determine the highest possible level of accuracy with which linear measurements can be taken from CT and the smallest dimensions measurable with this level of accuracy (Spoor, 1993). There are limitations to the accuracy of measurements taken from CT, which vary in their effect relative to the parameters according to which the image was taken. Slice thickness, matrix size, pixel size, and voxel size must all be taken into account to maximize the accuracy of the smallest measurements taken from CT. Sharp boundaries at tissue interfaces often appear as blurred contours on CT images. The degree of blurring is dependent on a variety of factors including the x-ray beam width, the dimensions of the detectors that interpret the x-rays, and the algorithms used to formulate an image from the raw data (Magnusson, 1987).

Error in the repeated collection of data is a problem that plagues all types of morphometric research. Without demonstrable repeatability, correlations between metric variables cannot be validated. In the case of the current research, the subsequent inability to attach probability estimates to associations made between an individual's CT images would render the technique unusable. It is thus critical that both the landmarks, and the measurements between them be selected to best facilitate the acquisition of repeatable data. Familiarity with the limitations of the media on which a technique is based is important in efforts to maximize repeatability, thus it is necessary to discuss the limitations of CT technology as relevant to measurement accuracy.

Limitations of CT imagery

The limitations of CT have to do with the quality of the picture produced. A variety of factors influence picture quality, most of which are directly related to the capabilities of the machine used, and are consequently becoming less and less problematic with continuing advances in CT technology. Hounsfield was the first to recognize some of these factors in his early research (1976). He referred to three factors in the image acquisition and interpretation process that influence and/or limit the quality of the resultant image: 1) picture grain; 2) picture spatial resolution, 3) and patient dosage. The relationship between the relative influence of these factors is complicated, and each varies in relation to each other.

Picture grain and picture spatial resolution are best described together as their relative influences on the resultant images are intertwined. Picture grain results from the passage of an insufficient number of photons through the imaged tissue and into the detectors on the other side of the body. The resulting graininess is the result of random variation in the amplitude of the individual points in the matrix, and complicates the accurate location of picture points on the image.

Picture spatial resolution, has to do with the number of squares in the image matrix. Resolution is increased as the number of squares increases. To achieve this, the photon beam is directed at a smaller area, and is passed across the selected areas a greater number of times. Problems with picture

grain can be exacerbated by increased resolution because the same amount of information is being spread across a larger number of squares in the matrix. Both picture grain, and picture resolution are significant limitations of CT imagery, though both have been greatly reduced with advances in CT technology in recent years. The relationship between picture grain and picture spatial resolution (matrix size) is complex and can best be expressed mathematically as: $(\text{inaccuracy})^2(\text{resolution})^3\alpha$ (Hounsfield, 1976: 4). This essentially means that a two-fold increase in the matrix size results in an increase of the amplitude at each square by a factor of 2.8. The grain is, however, smaller and not as detrimental to the image. So though the resolution of the image is compromised, the increase in the matrix size has made the variation more fine-grained and thus less disruptive. Techniques of smoothing images to enhance resolution by decreasing amplitude variation actually result in a loss of information, and are not therefore recommended for use with CT intended to visualize very small features.

Patient dosage is the last of the factors recognized by Hounsfield (1976) that limit the quality of the images produced by CT technology. Patient dosage influences the amount of picture grain in a CT image by varying the amount of radiation to which a patient is exposed. In turn, the amount of radiation that penetrates the body is influenced by the density and thickness of the tissue through which it must pass to reach the receiver. For this reason thoracic and abdominal organs are more susceptible to the ill effects of dosage related

picture grain than is the head. The only way to enhance resolution is by decreasing grain, and because grain is the result of deficient numbers of photons reaching the receiver, only increased radiation exposure can reduce or eliminate grain. In the interest of minimizing patient radiation exposure, picture grain will likely remain a complication of CT imagery.

Measurement accuracy

Each of the limitations discussed above results from the interaction of the properties of the tissue to be imaged and the user settings employed. These limitations also influence the accuracy with which measurement data can be collected from CT imagery. Even sharp boundaries at tissue interfaces appear as blurred contours on CT imagery. This blurring affects the ease and repeatability with which the actual interface can be located for measurement. The degree of blurring is dependent on several factors including x-ray beam width, the dimensions of the detector that collects the x-rays, and the algorithms used to formulate an image from the raw data (Magnusson, 1987). These interactions have considerable implications for the use of CT imagery in both clinical evaluation and forensic comparison. It is necessary to demonstrate either that a standardized solution will be used to increase the repeatability of measurements taken from CT imagery, or to select a measurement set that is not significantly influenced by these problems. The remainder of this chapter provides a discussion of the specific sources of error in measurements taken from CT. Following this, I discuss the solutions presented in the literature to the

problems associated with extracting repeatable measurements of small dimensions on CT imagery, and various means to circumvent these problems through the selection of a less susceptible measurement set.

The thickness of the individual slices can have a significant influence on the CT image produced and on its subsequent interpretation. The general rule regarding the thickness of slices taken is that using the smallest possible thickness minimizes partial volume imaging and facilitates extraction of the best possible spatial resolution perpendicular to the scan.

Partial volume averaging refers to the concept of averaging the different densities within a single voxel. The range of CT numbers that represent the various shades of gray in a single voxel must be averaged in order to attain a single CT number that is most representative of the entire slice. The thinner the slice, the fewer the number of CT numbers that need to be averaged, the less the effect of partial volume averaging, and theoretically, the more accurate is the single resultant value.

Tissue density can vary considerably across the thickness of a slice, and this variation increases with an increase in slice thickness. For this reason slice thickness is an important consideration in maximizing measurement accuracy. Tissue interfaces are represented as a descending or ascending array of CT numbers according to the shades of gray they represent. The angle of the slope of this array is directly related to the fuzziness of the interface and the accuracy with which measurement landmarks can be placed. For instance, the interface

of a foramen with the surrounding tissue may vary slightly in its position across the thickness of a slice if it is not oriented directly perpendicular to the slice plane. Thus, this partial volume averaging is enhanced in thicker slices. This is why tissue interfaces with steeper slopes (i.e. those which transition quickly from dark to light) incorporate fewer CT numbers, and thus less chance for error. The nearest approximation of the actual tissue interface lies at what is termed the "half maximum height" (HMH) of the array of CT numbers that represent the interface along the thickness of the slice (Seibert et al., 1980; Ulrich, 1980; Baxter and Sorensen, 1981; Eubanks et al., 1985; Magnusson, 1987). HMH corresponds to the average of the CT numbers along the slope of transition from one side of the interface to the other. Spoor (1993) suggested that "the size of objects larger than 1.0mm can be measured with an error range of +/-1mm by positioning the measurement points at half maximum height (HMH) of the CT number transition profile of the tissue interface" (Spoor, 1993: 19). As far as measurement accuracy is concerned, the implication of this is that in order for the measurement of the distance between two tissue interfaces to be accurate, each end point must be placed at the HMH for the local array of CT numbers (at each interface), rather than placed at the discretion of the observer. This method is known as measuring the full width of a feature at half maximum (Baxter and Sorensen, 1981; Spoor, 1993).

In turn the accuracy of HMH determinations is susceptible to the above stated limitations of CT picture quality and the distinct representation of the

image as a matrix of pixels. Picture quality is a determinant of HMH accuracy because it influences the width, height, and slope of the interfaces. The slope in particular has considerable influence on accurate determination of the HMH. A steep transition slope along an interface will introduce less error than will a more gradual slope because the transition involves a greater variation in density along the transition.

Spatial resolution influences the width of the CT number transition at the interface, thus an increase in the spatial resolution improves the accuracy with which the HMH of a particular interface can be located. The contrast, or density distinction of the tissues that meet at a particular interface also influence the accuracy with which an interface can be located. The higher the contrast or distinction between the tissues at the interface, the more accurately the HMH can be located. Another factor that complicates the accurate calculation of the HMH is that tissue interfaces are rarely perpendicular to the scan plane. This contributes to greater variation in the density along the thickness of a slice (Goodenough et al., 1981).

The slice index or interval is also important in CT imagery. CT slices are arranged in one of two ways: they either overlap one another, or are contiguous. The slice index for contiguously scanned images is the same as the thickness of the slice, whereas in overlapping slices, the slice index is half or less of the slice thickness. The slice index is essentially the net value associated with a particular slice, following corrected for slice overlap. Contiguous slices are more

frequently used in exploratory examinations, and thus represent the most frequently available data set for forensic comparison. The scans used in this research use 5mm contiguous slices.

Other factors that can influence measurement accuracy are artifacts in the image plane, noise in the image plane, and the use of different convolution filters. Artifacts interfere with the regular pattern of the CT number transition along the interface, thereby complicating the calculation of the HMH CT number. Image noise has a similar effect. If individual pixels within the interface are in the same density range as the noise, the result is a disruption of the regular pattern of the CT number transition along the interface. This is especially troublesome with interfaces between tissues of similar densities. Each of these limitations is of particular concern in the measurement of very small dimensions. The width of the CT number transition along an interface is very important to determine for this reason. This number represents the minimum distance between two separate interfaces that can be measured using their HMH numbers. Values smaller than this result in the interference of the HMH numbers for the opposing interfaces with one another. The CT numbers between the interfaces do not reach the actual value of the tissue they represent and the end result is that measurement of the distance between the interfaces is consistently overestimated. If the contrast at the two interfaces is similar and the tissue between them is roughly homogenous, as is often the case with foramina in the skull base, the CT number array that results from interference includes an

extreme value (either minimum or maximum) that is the same distance from both interfaces. This number can be used to accurately locate the center of a landmark for measurement.

Window width and center parameters can also influence measurement data taken from CT images, particularly the apparent size of the feature. Baxter and Sorensen (1981) used cylindrical and spherical phantoms to determine the level of error associated with both size and CT number estimation from CT. The cylinder, when scanned in a plane perpendicular to the x-ray beam, was used to approximate a feature for which there was no density variation over the course of the slice thickness. A sphere was used to represent the maximum density variation possible within a single slice. The phantoms allowed the authors to isolate the sources of significant error in both CT number and apparent object size. Specifically, they found that CT numbers cannot be accurately determined for spheres that have a diameter of less than the thickness of a single slice, implying that the diameter of spheres of this size cannot be determined accurately with a single window setting (Baxter and Sorensen, 1981). However, they were able to accurately estimate the diameter of spheres narrower than the thickness of a slice by centering the sphere in the slice and using the full width at half maximum profile to locate the center, and thus, the borders of the element (Baxter and Sorensen, 1981).

Various authors have tested the half maximum height method of locating tissue interfaces using CT imagery of various parts of the body including the

femur (Rubin et al., 1992; Feng et al., 1996), dental enamel (Spoor et al., 1993), the lungs (Checkley et al., 1984; Webb et al., 1984), and more generally, cortical bone geometry (Rho et al., 1995, Sumner, 1988). Each of these authors suggests that portions of the body with more consistent contrast distinctions facilitate easier and more accurate identification of tissue interfaces. This bodes well for the current research as the brain is a more homogenous tissue than most muscle or organ tissue. When compared with bone, the distinction between bone and brain is readily isolated.

Spoor (1993) evaluated the accuracy of linear measurements from CT images by using phantoms. The phantoms were polyurethane plastic with holes of varying diameters drilled in them. He evaluated both diameter measurements and center-to-center measurements, and concluded that calculation of both HMH and the extreme CT number are reliable means for the accurate interpretation of tissue interfaces and center points, respectively. He concluded that the critical minimum interface distance required to accurately calculate the HMH is 1.1mm, meaning that significant error is introduced in the measurement of features of less than 1.1mm in diameter, or if there is less than 1.1mm between two interfaces. He also found that in holes of less than 2.5mm, the CT numbers do not reach the true density value of the contents. This allowed for the calculation of the extreme CT number as a center measurement point. Comparison of the error rates between measurements taken using this method,

and those taken arbitrarily by two observers, show that error rates are reduced dramatically using these quantitative methods.

Koehler et al. (1979) determined that window center has a more considerable influence on apparent dimensions of structures in the CT image than does the window width setting. They also suggest that the greater the density difference (and subsequently CT number difference) between the tissues on either side of an interface, the greater the potential for error, and conversely, for the smaller the lesion imaged, the greater chance for error. Importantly, Koehler et al. note that the window setting that is most conducive to accurate extraction of measurements from CT images does not necessarily correspond to the setting which is of the most diagnostic utility (1979: 193). Koehler et al. (1979) list several considerations to take into account when taking serial measurements from CT scans: (1) that partial volume effects should be minimized by selecting a slice that best represents the full extent of a particular feature, (2) that accurate window settings must be made specifically for the particular tissue imaged, and (3) that this data should accompany the image itself upon curation.

Various inter and intra-observer error studies provide a more practical evaluation of the extent to which measurements taken from CT images are accurate representations of the actual tissues (Christiansen et al., 1986; Hildebolt and Vannier, 1988; Matteson et al., 1989; Waitzman et al., 1992; Richardson et al., 1993). Rather than addressing the issues of measurement

error as a related to either partial volume imaging, window settings, or other problems related to density variation along tissue interfaces, these articles instead focus on repeatability as an observer dependent variable. They suggest that with the correct selection of window setting, particularly the window center setting, accurate measurement data can be extracted without regard to problems associated with partial volume averaging, and the resultant blurring of tissue interfaces (Koehler et al., 1979).

Much of this work has been dedicated to the validation of cranial metric data extracted from CT images (Christiansen et al., 1986; Hildebolt and Vannier, 1988; Matteson et al., 1989; Waitzman et al., 1992; Richardson et al., 1993). Christiansen et al. (1986) compared measurements taken from CT representations of a sample of human mandibles to measurements taken directly from the mandibles themselves. They investigated error levels associated with observer bias by having each of the specimens and their CT representations measured on two occasions by personnel of varied levels of radiological training and found that error levels for each of the experiments were within the acceptable range (0.4mm to 0.9mm) (Christiansen et al., 1986). Waitzman et al. (1992) evaluated inter- and intra-observer reproducibility of measurements of the facial skeleton taken from CT. Measurements taken from a sample of five skulls were compared to measurements obtained from CT images of the same skulls. The result was “excellent agreement” between the measurements taken from the skulls themselves and those taken from the CT

images (Waitzman et al., 1992). The percent differences between the measurements taken from the CT images and directly from the skulls ranged from 0.1 to 3.0 percent, with a mean of 0.9 percent. The combined percent difference for the 40 measurements taken was less than one percent. They also found that the smallest dimensions had the highest rates of error, though the difference was not significant (Waitzman et al., 1992).

In order to evaluate quantitatively the anatomical fidelity of 3D images created using computer programs such as 3D Doctor, Hildebolt et al. (1990) used a comparison of measurements taken directly from crania using calipers both to measurements taken from the original CT slices, and to the same measurements taken from 3D reconstructions made from the CT slices. The authors found few statistically significant differences between the measurement techniques, but acknowledge that small sample size (n=5) may have masked variation that was present. However in spite of the scarcity of statistical support, they also claim that there are “substantive differences between the techniques” (Hildebolt et al., 1990: 286). They suggest that the distinction is based on the assumption that, if a substantive difference did not exist, then one should expect the same level of error to result from comparison of measurements taken from CT to those taken by caliper as between repeat measurement by caliper. They note that this is not the case. The authors find that the mean differences are consistently larger when comparison is made between CT and caliper measurement than between measurement data extracted at different times

using calipers. Whereas the mean differences between repeat caliper measurements exceeded 1mm for only one measurement, all but four (of 114) measurements varied by at least 1mm between measurements sets taken from CT (either slice data or 3D reconstruction) and caliper measurements. In addition, CT slice measurement error exceeded 2mm for 15 measurements, seven exceed 3mm, three exceed 4mm, and one exceeded 5mm. The measurements taken from 3D reconstructions faired better, only five varied from the caliper measures by more than 2mm and one by more than 3mm. In spite of the lack of statistical support the authors suggest that measurements taken from 3D reconstructions are more true to the dimensions of the tissue being scanned than are caliper measurements taken directly from the skulls. They also suggest that measurement landmarks are more easily located on 3D reconstructions than on slices.

Hildebolt et al. (1990: 293) suggest that a more appropriate methodology would involve the location of coordinate data from which measurement values could then be extracted (Hildebolt et al., 1990: 293), although they did not attempt this. This methodology is supported and described by Richtsmeier et al. (1995). Their study evaluated the precision, and repeatability of locating landmarks on CT images. The average error in the location of landmarks on both 3D reconstructions and CT slices was less than 0.5mm. Repeatability data indicated that less than 2% of the variation in their sample was the result of measurement error using the coordinate method. They also recommend against

comparing measurement data collected from CT to conventional anthropometric data, suggesting instead, that “since the CT data are sufficiently precise and accurate, studies using CT data exclusively are justified” (Richtsmeier et al., 1995: 226).

Considerable literature is dedicated to CT imaging of the temporal bone itself, specifically as it relates to the various functional, and embryological zones of the cranial base, including the inner and middle ear, the cerebello-pontine angle, and the temporo-mandibular joint. A number of very important articles address image quality in CT of the temporal bone specifically. Some of these papers discuss the evaluation of the resolution of CT imagery of the temporal through direct comparison of CT images to macro-anatomic sections (Beatty et al., 1981, Littleton et al., 1981; Chakeres and Spiegel, 1983). Others compare CT images of temporal bone morphology to casts of the temporal bone (Wilbrand 1984; Muren and Ytterbergh, 1986). Most investigators advocate the use of high-resolution (320 x320 or 512 x512 pixel matrix) images reconstructed with a bone algorithm (Brogan and Chakeres, 1989). Two image subsets are used in the current research, both are visualized in 512 x 512 pixel matrices, but the images in one subset have 5mm thick slices, and the other have 1mm thick slices. The 5mm slices are more typical of what might be available to the forensic anthropologist for comparison to CT images taken postmortem because 3 to 5mm slices are used in exploratory CT scans that aim to study both bony and soft tissue components of the head.

IMPLICATIONS FOR THE PRESENT RESEARCH

In the current research, the choice of a dataset represents a compromise between the use of the most ideally suited, and the most commonly available CT data. It also represents an effort to generate a method for individual identification that is most readily repeatable (and least complicated). I attempted to maximize the accuracy and efficiency of the analysis, while mitigating the limiting influences sufficiently to facilitate the repeatability of those analyses. In the following paragraphs I briefly address the extent to which the above factors influence this particular research, and the manner in which I deal with each of them. A more detailed description of the steps in this process is presented in Chapter V.

Though each of the limitations listed above can potentially confound the use of CT imagery to identify individual skeletal remains, there are ways to circumvent their negative effects. In the broadest sense, the best means to maximize the repeatability of this method is methodological standardization, particularly with regard to user settings. For instance, it is important to emulate the antemortem window width and contrast settings as closely as possible in postmortem imagery. In other words, the settings of the postmortem image should be the same as those used during antemortem examination of that person.

Use of the DICOM image format allows for post-scan correction of problems associated with variation between ante- and postmortem window

settings in instances in which the postmortem image settings were not identical to the antemortem settings. DICOM is an acronym for Digital Imaging and Communication in Medicine, and refers to a cooperative standard that facilitates efficiency and usability in medical imaging (ACR-NEMA, 1988). The DICOM Standards Committee is an agency whose mandate is to create and maintain international standards for the communication of biomedical and diagnostic information in the medical use of digital media, and the DICOM standard is intended to maintain international compatibility and efficiency in medical imagery. This standard is used worldwide and, in addition to facilitating compatibility, provides the highest level of postmortem user manipulation (ACR-NEMA, 1988). For instance, DICOM images facilitate post scan adjustment of various of the user settings, including the window width and scale (Clunie and Carrino, 2001). This information is critical to circumventing problems associated with the variable image quality of CT scans discussed in the previous chapter (Clunie and Carrino, 2001).

There is more than one solution to the problem of measurement repeatability. The cautionary articles cited above each described error in the measurement of the smallest dimensions. Spoor's (1993) research involves measurement of the bony labyrinth and demonstrates that measurements of more than 1mm can be considered accurate and repeatable using the HMH method. Hildebolt (1990) demonstrated that slightly larger measurements could be repeatably measured without calculation of the HMH. The present research

incorporates measures that are significantly larger than those that are most susceptible to error associated with partial volume error and density variation; the smallest measurement used in this research has a mean value of 25mm. Additionally, for this type of research, measurement error does not necessarily have to be completely eliminated, as long as it is duplicated. Whereas effective clinical evaluation of anomalies seen on CT is dependent on the ability to eliminate measurement error, this research need only duplicate whatever error there may be in the original measurement used for comparison.

In spite of the fact that determination of HMH may not be necessary when using measurements of sufficient size, I have devised a method for standardizing the placement of the landmarks used in this research. The 3D Doctor program used to collect the coordinate data for this research has an automatic segmentation procedure, which automatically traces selected tissue boundaries based on the grayscale range at the interface. In fact, it places the boundaries at the middle most shade of gray along a particular array, thus approximating the HMH of that boundary. This process removes much of the error that may have otherwise been introduced in visually placing the points. Even if the boundaries are not placed at exactly the HMH, they provide a means to standardize the interface location, thus standardizing the data.

The limitations associated with picture quality must also be addressed in forensic applications of CT imaging. Assessment of both resolution and picture grain is critical to the successful postmortem adjustment of the CT user settings

in replicating the antemortem image as closely as possible. Postmortem CT scans are not as susceptible to either picture grain or resolution complications because: (1) radiation exposure is not limited by risk to the patient and (2) soft tissue is often not present, the end result of both being that soft tissue interference is less likely to cause amplitude variation and consequent graininess. Picture quality is also less disruptive in imaging of the skull because there is little soft tissue interference in axial imaging of the head (Haaga, 1994). Twenty times the x-rays pass through the skull as do through the abdomen thereby significantly reducing picture grain (Haaga, 1994).

In conclusion, computed tomography is a reliable medium for the forensic comparison of ante- and postmortem images of the petrous portion of the human temporal bone. Its primary advantages are the resolution of the images its produces, the ease with which images can be reproduced, and its prevalence in the antemortem record. Chapter IV provides a description of the anatomy of the petrous portion as seen on CT imagery, and its specific application in this research is described in Chapter V.

CHAPTER IV

ANATOMY, ONTOGENY, AND EVOLUTION OF THE HUMAN TEMPORAL BONE

A detailed knowledge of both the anatomy and ontogeny of the petrous temporal bone and its constituents is a prerequisite to its potential employment as an individuating characteristic in forensic investigations. The temporal bone is one of the most structurally intricate bones in the skeleton in terms of its anatomy, as it is the site of a variety of functional responsibilities including hearing, balance, anchoring the masticatory apparatus, providing passage for various nerves and blood vessels into the brain, and providing attachment sites for some of the neck musculature.

Anatomical descriptions of the temporal bone are generally one of two types, but both are of utility to this research. Classical discussions of temporal bone anatomy are based on the embryological development of the bone, and hence, divide the bone into regions that are distinct from one another during various periods of the growth process. However, clinicians often prefer to consider the anatomy of the temporal bone, particularly the petrous temporal bone, as a combination of functional rather than embryological components (Davidson, 2002). The following description of the temporal bone combines elements of both of these perspectives. I first use an embryological perspective is used to describe the temporal bone as a whole. On the other hand, I discuss

the components of the ear from a functional perspective, to better illustrate the complexity of relationships between structures that often involve more than one of the embryological regions of the temporal bone.

ANATOMIC REGIONS OF THE ADULT HUMAN TEMPORAL BONE

The temporal bone is made up of four distinct regions: the squamous, mastoid, tympanic and petrous parts, each of which are readily visible on the external surface of the dry skull, and which represent independent ossification centers. The squamous portion of the temporal bone is the nearly vertical, flat portion of the bone that constitutes the portion of the lateral border of the skull above the zygomatic arch. The squama articulates along its superior border with the parietal at the squamosal suture, and in concert with the parietal bones acts as the attachment site for the temporalis muscles. The sutural superior border of the squamous temporal bone is beveled internally and overlaps the inferior border of the parietal bone with which it articulates. In humans this is the only suture in the skull that displays this morphology, and its form is likely related to the alleviation of stresses associated with mastication (Rak, 1978, Mao et al., 2003). At its posterior extent, the parietal notch marks the location where the temporal, parietal and occipital bones articulate. Internally, the surface of the squamosal portion is demarcated with the grooves for the middle meningeal vessels, and externally by the groove for the middle temporal artery. These sets of vessels contribute to the blood supply of the middle and inner ear respectively. The zygomatic process of the temporal bone extends anteriorly

from its root located directly superior to the external auditory meatus to articulate with the zygomatic process of the zygomatic or malar bone. Immediately inferior to the zygomatic process, and anterior to the external auditory meatus is the glenoid or mandibular fossa, which is the point of articulation for the mandible and is a site of considerable variability relative to functional factors and dietary diversity. The fossa is bordered anteriorly by the articular eminence, and posteriorly by the postglenoid process. The petrotympanic fissure is located immediately posterior to the postglenoid process and separates it from the tympanic region. Anterior to the glenoid fossa, the temporal articulates with the sphenoid.

The mastoid parts of the temporal bone are home to the mastoid processes, the large bilateral bony sites for the attachment of the sternocleidomastoid muscles. The mastoids mark the posterior-inferior extent of the temporal bone and, as a result of their function as muscle attachments, are rugose and irregular in appearance. On the infero-medial surface of the temporal bone are the mastoid notches. The mastoid foramen, which are located on the lateral surface of the bone, are variable in their location and morphology.

Lying between the mastoid processes and the petrotympanic fissures are the tympanic portions of temporal bone. These are small plates of bone that encircle the aperture of the external auditory meatuses. The vaginal processes are another small plate of bone that lie just inferior to the external auditory

meatuses and surround the base of the styloid processes. They merge medially with the petrous portion near the carotid canal.

The petrous portion is the most complex part of the temporal bone. It projects anteriorly and medially, as the inferior most segment of the temporal bone. The petrous portion houses the organs of the ear, and provides a conduit for much of the vascular and nervous supply to the head and as such it has a complex and highly variable anatomy. The internal carotid artery and jugular vein pass through the cranial base according to variably serpentine pathways. The internal carotid artery passes through the carotid canal directly into the cranial cavity, and the jugular vein drains blood from the cranial cavity through the jugular canal, which is located just postero-laterally to the carotid canal. The styloid process is located immediately lateral to the jugular fossa, and is generally accompanied by a stylomastoid foramen that accommodates a portion of the facial nerve. The posterior wall of the petrous portion of the temporal bone is in humans nearly vertical from its medial to lateral extents. Near the medio-lateral center of the posterior wall lies the opening of the internal auditory canal, which carries the facial, and auditory nerves, as well as the internal auditory artery to the inner ear.

FUNCTIONAL REGIONS OF THE PETROUS PORTION OF THE HUMAN TEMPORAL BONE

It is particularly useful to have a detailed knowledge of the anatomy of each part of the petrous bone when reorienting fragmentary petrous elements is

necessary. Additionally, various features of the temporal bone, including foramina, represent valuable measurement landmarks for the current research. Nearly all of these internal structures are associated with the maintenance of hearing and balance. Thus, the petrous portion is essentially the structural container for the components of the middle and inner ear. For this reason, a functional description of the petrous bone most adequately relates structure and function of this segment of the temporal bone, and the individual components are best described in relation to their placement along the ear canal. Functionally, the ear is divided into six components: the internal auditory canal, the inner ear, the middle ear and mastoid process, the intra-temporal facial nerve, the surrounding petrous bone, and the external auditory meatus.

The external auditory meatus (EAM) of humans is generally around 2.5 cm in length, the medial two-thirds of which is osseous and the lateral third cartilaginous (Gulya and Scuknecht, 1995). The junction between the bony and cartilaginous parts of the EAM is its narrowest location, and the variation in diameter at this junction (particularly on CT images) is considerable (Casselman, 1996). The osseous part is oriented in an infero-anterior direction. The tympanic membrane is angled in its orientation relative to the axis of the petrous bone and as a result, the EAM is usually about 6mm longer antero-posteriorly than superior-inferiorly (Gulya and Scuknecht, 1995). The anterior wall of the EAM is occasionally pneumatized. The tissue of the tympanic membrane is continuous with the skin that lines the osseous canal, and is much thinner in

cross section (0.2mm) in the osseous portion of the canal than in the fibro-cartilaginous portion. In combination with the typically thin cross section of the posterior bony wall of the meatus, this makes this a clinically important area, both in terms of its susceptibility to infection, and the propensity of the underlying periosteum to respond in the form of exostoses, often thought to be stimulated by to chronic exposure to cold water (Adams, 1951; Kennedy, 1986). Exostoses appear as localities of laminated bony tissue, and are clinically silent until they are quite large in size. Since these growths are both radio-opaque, and develop independently of other pathology, they may be useful in forensic comparison of radiographs or CT imagery.

Middle ear

The middle ear (tympanic cavity) is demarcated laterally by the tympanic membrane, and is best described as irregularly shaped. It is generally conical at its lateral boundary as a result of the articulation of the manubrium of the malleus and the umbo (the small depression in the tympanic membrane at which the malleus attaches). It measures approximately 15mm both antero-posteriorly and supero-inferiorly at its medial extent. Lateral to a constriction that lies nearly in the medio-lateral center of the cavity, the remainder of the cavity extends in a smaller antero-posterior dimension. The vertical diameter of the tympanic membrane of humans is generally between 8.5 and 10mm, while the antero-posterior diameter is usually between 8 and 9mm, indicating the nearly round configuration of the EAM at its intersection with the middle ear in humans (Gulya

and Scuknecht, 1995). The tympanic membrane is a complicated structure, being variable in its density and tension across its supero-inferior length. This has structural and functional implications for the malleus, the ossicle to which it is attached.

The three ear ossicles –the incus, malleus, and stapes– are located within the middle ear and are suspended by ligaments and membranes in a complex matrix that allows for the physical transmittal of sound from the tympanic membrane to the inner ear (Anson et al., 1948). The lateral-most ossicle is the malleus, which is commonly referred to as hammer-like in shape. It is approximately 5mm long, and it is characterized by its prominent head, which has a facet for the incus on one side. From the head of the malleus extends a spur of bone, from which three processes project, the anterior spur, posterior spur, and the manubrium. The anterior process is thought to have little functional significance in humans as it is frequently resorbed without hearing loss (Gulya and Scuknecht, 1995). The malleus is anchored to the wall of the petrotympanic fissure in such a way that the ossicles are able to rotate in concert with one another, despite the ligamentous anchoring of the incus to the fissure.

The incus is the largest of the ossicles commonly referred to as the anvil. It is composed of a body, short and long processes, and a lenticular process. The body is marked by a facet for articulation with the head of the malleus within the epitympanum. In addition to the ligamentous linkage between them, the

shape of the articulation between the malleus and incus restricts the relative movement of each in order to facilitate normal hearing (Anson et al., 1960). The short crus of the incus occupies the posterior incudal recess posterior to the body, and the long process is oriented inferiorly and ends as the lenticular process. The lenticular process articulates with the head of the stapes. The incus is anchored by three ligaments: the posterior incudal ligament, posteriorly, and the posterior and lateral incudomalleal ligaments, anteriorly. The posteromalleal ligament ossifies on occasion (Gulya and Scuknecht,1995). Ontogenetically, otitis media can have a considerable effect on the long process of the incus, and it can sometimes be highly pneumatized as a result (Gulya and Scuknecht, 1995), though not usually to an extent sufficient to be visible on CT.

The most medial of the ossicles is the stapes, which is also the smallest of the three. It consists of a head, anterior crus, and posterior crus, which come together to form a stirrup shape. In concert with the annular ligament, the footplate of the stapes acts to seal the oval window, and is highly variable in shape. The head of the stapes articulates with the lenticular process of the incus. The stapedial processes are individually variable in thickness and curvature (Anson and Bast, 1958). The articular ends of each of the ossicles are lined with cartilage, making the joints between them movable in the same way as most of the other joints in the body. Articular discs may be present between the ossicles as well, but seem to have little or no clinical significance. Each joint articulates within a synovial capsule. These joints perform well in resistance to

disarticulation by physiological stress, but are easily disrupted by direct contact (Castellote et al., 1997).

In spite of their variable morphology and arrangement, which depends on the morphology of the surrounding tympanic cavity, the ossicles are typically of little forensic value once decomposition has begun. The soft cartilaginous tissues that connect them both to the surrounding bones and to each other distort and eventually decompose entirely. In fact, the ossicles are often lost entirely in skeletonized remains. Even when the ossicles are not lost, their antemortem arrangement is often not preserved for comparison to postmortem films. In addition, the ossicles and the joints between them are susceptible in the living to distortion by relatively minor and short-lived insults, especially infection (Chakeres and Weider, 1985; Bluestone, 2000). This susceptibility to degenerative change also makes both their morphology and their relative arrangement unreliable for forensic comparison. Figure 4.1 illustrates the normal morphological configuration of adult human ear ossicles.

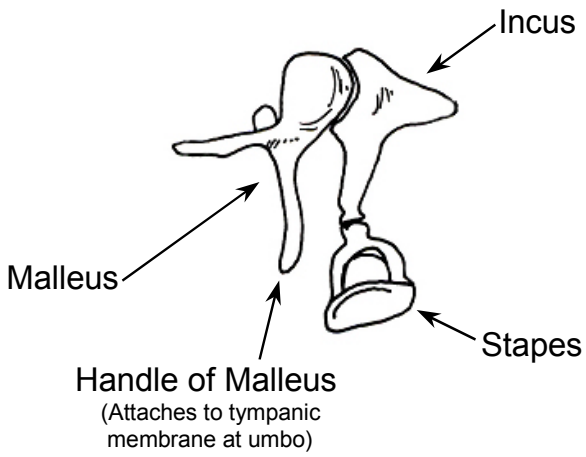

Figure 4.1. *Articluated ear ossicles (medial view).*

Blood supply to the ossicles is complex and debated. The major supply to the lateral ossicles (malleus and incus) comes from branches of the anterior tympanic artery rather than the middle meningeal artery as was previously thought. This branch of the anterior tympanic artery, referred to as the ossicular artery, (Nager and Nager, 1953) branches within the upper petrotympanic fissure and typically enters the middle ear cavity in accompaniment with the chorda tympani nerve. The ossicular artery then divides into two branches, one for the malleus and one for the incus soon after its entrance into the middle ear cavity. The branches are aptly named the malleolar and incudal arteries. The stapes, as the likely result of its small size, has a unique, and limited blood supply. Nager and Nager (1953) found that only the thickened margin of the footplate, and the neck and head were inundated with blood vessels, the remainder of the bone being nourished either by diffusion or osmosis (Nager and

Nager, 1953: 931). The vessels that do reach the stapes are branches of the very complex mucosal network in the middle ear. Various of the vessels in this network anastomose in a complex pattern in the fossula of the stapes, thereby communicating with one another at the neck, tympanic aspect of the footplate, and across the obturator foramen of the ossicle (Anson et al., 1948).

Various features of the tympanic cavity are useful as measurement landmarks, and in the correct orientation of fragments of the petrous for comparison to antemortem records. For this reason I describe the morphology of the tympanic cavity here in detail. Clinicians divide the tympanic cavity broadly into the mesotympanum, epitympanum, protympanum, and hypotympanum, which are of utility in this research because they allow for the standardization of CT slice selection based on the presence or absence of the landmarks associated with each. The tympanic cavity is pneumatized, and linked to the pharynx by the eustachian tube. It is also linked posteriorly to the mastoid air cells. The root of the styloid process and the jugular bulb visibly influence the inferior surface of the cavity. The mastoid surface of the cavity is the location of a variety of anatomical features. The facial recess, chordal eminence, pyramidal eminence, incudal fossa, and foramen for the chorda tympani nerve are all visible features of the posterior wall. The epitympanic cavity opens into the mastoid antrum superiorly.

The mesotympanum is the portion of the tympanic cavity located just medial to the tympanic membrane. The epitympanum represents about a third

of the tympanic cavity, and incorporates the space superior to a line drawn horizontally from the upper boundary of the tympanic membrane. The head of the malleus, as well as the body and short process of the incus, are located within the epitympanum. The portion of the tympanic cavity that lies inferior to line drawn horizontally from the inferior margin of the tympanic annulus is referred to as the hypotympanum. Finally, the protympanum is the portion of the middle ear cavity that is located anterior to a coronal plane through the anterior boundary of the tympanic annulus. Each of these cavities is variable in shape, especially the hypotympanum, which is also variable in its depth. This variability is incorporated into the measurement set used in the current research.

The walls of the tympanic cavity contain numerous features that are also useful as measurement landmarks, and are again useful in the correct orientation of fragments of the petrous bone prior to forensic comparison. For example, the contour of the anterior wall corresponds to the course of the internal carotid artery just anterior to it. The superior aspect of the anterior wall is the location of the opening of the eustachian tube, immediately above which the groove for the tensor tympani muscle is located. The anterior wall narrows inferiorly and is formed by the by the thin bony walls of the carotid canal. This wall is often surrounded by pneumatized cells.

The tegmen tympani comprises the superior margin of the tympanic cavity, and stands as the only, and a very thin boundary separating the middle ear from the overlying cranial cavity. A portion of the tegmen tympani is

dehiscent in a small percentage of the population (Kim et al., 2003). The lateral wall of the tympanic cavity is largely membranous, composed of the tympanic membrane or eardrum. The membrane is encircled by the bony tympanic ring. Portions of the lateral boundary are also comprised of the scutum, a layer of bone extending from the squama. The floor, or inferior wall, of the tympanic cavity is largely composed of the superior boundary of the underlying jugular bulb, which often has an irregular appearance as a result of overlying pneumatized cells. The root from which the styloid process extends is located in the posterior third of the floor of the tympanic cavity.

The posterior wall of the tympanic cavity, also referred to as the mastoid wall, is wider superiorly than inferiorly and is complex in its anatomy. Inferiorly, tympanic air cells connect to the pyramidal eminence to which the stapedius muscle attaches. Lateral to the pyramidal eminence is the chordal eminence. The chordal, pyramidal and styloid prominences of the posterior wall of the tympanic cavity are connected by three ridges of bone. The chordal ridge connects the chordal eminence to the pyramidal eminence, the styloid ridge extends between the styloid prominence and the chordal eminence, and the pyramidal ridge joins the styloid prominence to the pyramidal eminence. The chorda tympani passes into the middle ear through a foramen in the chordal eminence named the iter chordae posterius. The recess located between the chordal and pyramidal eminences is the facial recess. The incudal recess marks the superior limit of the facial recess and is the point of articulation between the

posterior wall of the tympanic cavity and the short process of the incus. The epitympanic recess opens superiorly into the mastoid antrum.

The medial wall is perhaps the most complex of the boundaries of the middle ear cavity (Toth et al., 2006). The sinus tympani, round window niche and oval window niche are all located on the medial wall. The subiculum, and the promontory, which is the bony eminence overlying the basal turn of the cochlea, are also visible on the medial wall. The prominence overlying the facial canal is also visible as it traverses the medial wall on its way to the mastoid wall. The sinus tympani is located between the ponticulus (a bony ridge connecting the promontory and pyramidal eminence superiorly) and the subiculum (another ridge that connects the styloid eminence superiorly to the posterior margin of the round window niche inferiorly). The round window niche is a bony depression located anteriorly to the subiculum. Antero-superior to the round window niche is the promontory, a bony elevation that accommodates the basal turn of the cochlea. The oval window niche is located antero-superiorly to the ponticulus, and postero-superiorly is the facial canal prominence which passes from the medial wall to the mastoid wall of the tympanic cavity to the stylomastoid foramen.

These niches in the walls of the tympanic cavity are of clinical significance because they are the location for the oval and round windows, as well as the sinus tympani, and thus have been described in detail in the literature (Paprocki et al., 2004; Toth et al., 2006). They are also of utility in the current research as

both potential measurement landmarks and as anchors around which fragments of the petrous bone can be correctly oriented. The oval window is more specifically located in the posterior part of the medial wall in the mesotympanum. It houses the stapes and falls immediately inferior to the facial nerve and superior to the promontory. The cochleariform process is located just anterior to the oval window, and the ponticulus, sinus tympani, and pyramidal eminence are each located posteriorly to the oval window niche. The round window niche is a depression located postero-inferiorly to the promontory and superiorly to the hypotympanum. The subiculum separates the round window from the sinus tympani.

The sinus tympani is the third niche in the medial wall of the tympanic cavity and is bounded medially by the bony labyrinth and laterally by the pyramidal eminence and facial nerve. More specifically, it is inferior to the lateral semicircular canal of the inner ear, and anterior to the posterior semicircular canal. The wall of the jugular bulb and the styloid eminence are located just inferior to the sinus tympani. As are the oval and round windows, the sinus tympani is variable in its depth and morphology. The facial recess is a depression in the posterior, rather than the medial wall of the tympanic cavity located between the facial nerve canal medially and the tympanic bone laterally.

The subarcuate fossa is located posterior to the middle ear, and is visible on the external surface of the posterior wall of the petrous pyramid. It is the opening into the petromastoid canal through which the subarcuate vein passes

on its way to the superior semicircular canal. The fossa usually appears as a shallow depression located posterior and superior to the opening of the internal auditory canal.

Inner ear

The inner ear cavity houses the components of the bony labyrinth. This is another portion of the internal petrous anatomy that is of diagnostic value both on CT imagery, and by visualizing its influence on the surface anatomy of the petrous portion. Developmentally, the bony labyrinth is an embryological derivative of the otic capsule. The labyrinth is typically about 20mm in length (Anson and Donaldson, 1972; Gulya and Scuknecht, 1995), and is made up of the cochlea, vestibule, and semi-circular canals.

In maturity, the osseous cochlea resembles a coiled snail shell, hence its name. The coil winds two and one half turns around a structure referred to as the modiolus (Gulya and Scuknecht, 1995). The antero-lateral extension of the internal auditory canal is the anatomical location of this coiled portion of the labyrinth in the adult ear. The anterior portion of the cochlear canal is referred to as the scala vestibule, and is divided from posterior portion by the spiral lamina. The portion of the cochlear canal posterior to the spiral lamina is referred to as the scala tympani. The two scala communicate at an apex referred to as the helicotremia. There is a second, smaller spiral lamina that encompasses the external wall of the basal turn of the cochlea. In its entirety, the cochlea measures about 5mm in its supero-inferior dimension. It is visible on CT as an

opaque oval shape located just laterally to the lateral most extension of the internal auditory canal.

The cochlea articulates with the vestibule, which is the central chamber connecting the cochlea with the semi-circular canals. It is typically about 4mm in diameter (Gulya and Scuknecht, 1995). There are openings in the walls of the vestibule for communication with both the cochlea (on the anterior wall) and semicircular canals (on the posterior wall). On the lateral wall is the oval window, which opens into the previously discussed tympanic cavity. There is also an opening for the vestibular aqueduct on the postero-inferior aspect of the vestibule. The vestibule is visible as an oblong opacity with its axis oriented approximately 45° from the sagittal plane.

There are three orthogonally-oriented semicircular canals: the lateral, posterior, and superior, the lumen of each of which is approximately 1mm in cross section. The canals are located just posterior to the vestibule, creating an overall axis of the labyrinth that approximates the long axis of the petrous bone. The canals intersect at ampullae, each of which is approximately twice the diameter of the remainder of the canals. There is a common crus at which the posterior and superior canals intersect, just anterior to the vestibule. However, either directly, or through ampullae, each canal is in communication with the vestibule. The orientation of the canals places them in an orthogonal spatial relationship to one another. Portions of the labyrinth translate onto the surface anatomy of the petrous. The semi-circular canals in particular have surface

anatomy that is plainly associated with them. For instance the arcuate eminence is the surface accommodation for the extension of the superior semi-circular canal, and the posterior semicircular canal seems to determine shape of the posterior wall of the petrous bone in the form of an as yet unnamed eminence. I do not discuss the numerous soft tissue constituents of the inner ear because they are not visible on CT imagery and are not present in decomposed skeletal remains. Each of the semicircular canals is clearly visible on CT, as are the intersections between them. These intersections represent particularly repeatable landmarks on which measurements of the inner and middle ear can be based. Figure 4.2 illustrates the morphological relationship of the various components of the inner ear.

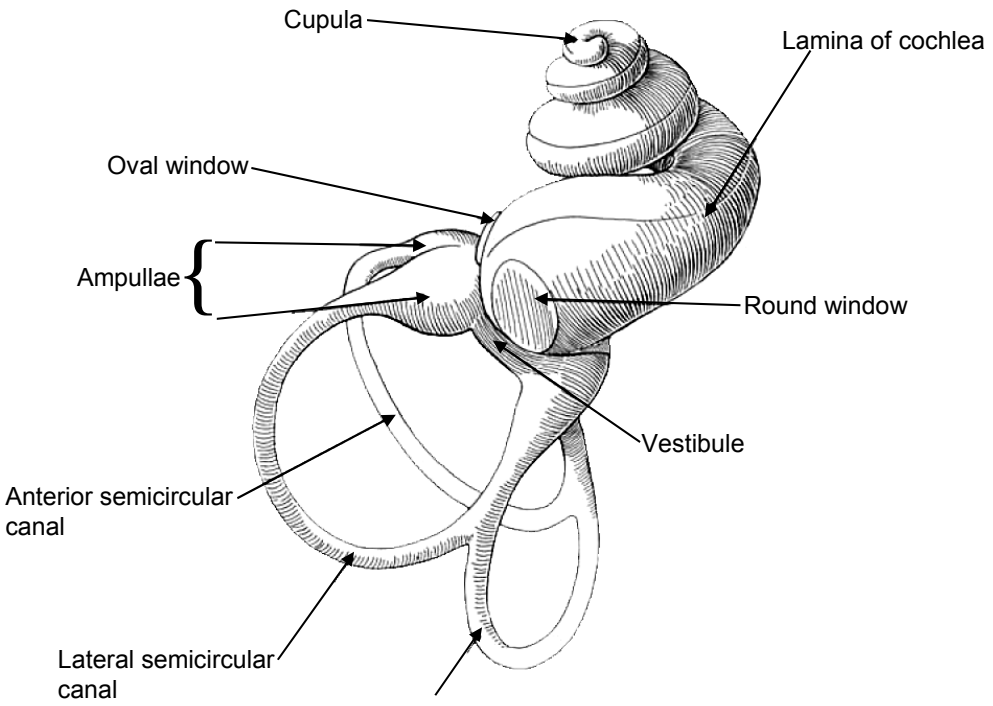

Figure 4.2. *Inner ear including the vestibule, cochlea and semicircular canals.*

Blood and nervous supply to the inner ear are furnished in large part through the internal auditory canal (IAC). The morphology of the internal auditory canal is highly variable and clearly visible on CT imagery. The IAC is a bony canal located nearly in the center of the petrous temporal bone that opens onto the posterior wall of the petrous pyramid, and extends antero-laterally to its articulation with the cochlea. Anatomically, it consists of three distinct regions: the fundus, canal, and porus. The fundus is the lateral-most extension of the canal that is in contact with the medial aspect of the bony labyrinth. The canal itself is located between the fundus and the porus. The porus is the inlet of the IAC, which opens onto the vertical posterior wall of the petrous part of the

temporal bone. The IAC acts as the neurovascular conduit from the posterior cranial fossa into the petrous bone and inner ear. It provides transport for the facial, cochlear, and vestibular nerves, as well as the nervus intermedius, and labyrinthine artery and vein. Both the dura and arachnoid membranes extend into the canal laterally to the lamina cribrosa, the lateral extent of the fundus at its articulation with the labyrinth. The canal is divided transversely by a bony ridge called the falciform crest. The falciform crest separates the superior and inferior compartments of the canal, which carry different portions of the IAC's neuro-vascular contents. The upper compartment is further subdivided into an anterior compartment (containing the facial nerve and nervus intermedius), and a posterior compartment (which contains the superior vestibular division of the subdivided vestibulo-cochlear nerve). The lower compartment then carries the cochlear nerve anteriorly and the inferior division of the vestibular nerve. The inferior, superior, and posterior margins of the porus of the IAC are often referred to collectively as the semilunar lip, and are of clinical significance in their frequent remodeling due to neoplasms located within the canal.

The size and shape of the IAC are often influenced by the extent of pneumatization of the surrounding bone, particularly in the apex region of the petrous portion. The average antero-posterior length of the IAC is also variable, but averages about 8mm (Portmann et al., 1975). This variable length is likely related to the variation in the angle of the IAC in relation to the various structures around it. Portmann et al. (1975) noted that the IAC is between 80° and 90°

from the sagittal plane in 58% of the individuals in their radiographic study, and between 91° and 100° in 37% of individuals in their sample. They attribute variability in this angle to localized variation in the surrounding pneumatized bone. Several articles have been published in the forensic literature that argue that variation in the angle between the IAC and long axis of the petrous bone is correlated to the sex of the individual (Kalmey and Rathbun, 1996; Graw et al., 1999; Noren et al., 2005). The “lateral angle” is typically greater than 45° in females and less than 45° in males (Graw et al., 1999). Noren et al. attribute the greater angle in females to the relatively smaller medio-lateral dimension of the female petrous bone in their sample (Noren et al., 2005). Each of these studies achieved accuracy rates in excess of 80% in the classification of individuals to sex by measurement of the lateral angle.

The IAC is relatively symmetrical in diameter, but not in its length. The relative constancy of the diameter of the IAC has been attributed to the invariable constraints of its neurovascular contents, whereas the length and angle of the IAC is influenced by the more variable structure of the pneumatized medial portion of the petrous bone (Portmann et al., 1975). The postero-medial to antero-lateral contour of the walls of the IAC is variable. The canal ranges from uniformly cylindrical in diameter, to more conical in shape, tapering in diameter nearer the fundus. Less commonly, the IAC tapers in the other direction, though usually only slightly, and in yet other individuals it displays an “hourglass” shaped contour (Gulya and Schuknecht,1994). This hourglass

shape is often the result of localized anterior and/or posterior cupping in the walls of the IAC (Sakashita and Sando, 1995).

The jugular and carotid foramina provide passage for blood vessels to and from the brain through the petrous bone. These foramina are variable in their location and morphology, and thus, they are valuable in the present research. They are also both clearly visible on CT imagery. The internal carotid artery is housed within the carotid canal as it passes through the petrous bone. The internal carotid artery gains entry into the petrous on the inferior aspect through the carotid canal immediately medial to the styloid process and anterior to the middle ear and cochlea. The artery travels superiorly to the level of the middle ear and then takes a sharp antero-medial turn to course beneath the Eustachian tube. Then, the artery takes another superior turn and enters the cranial cavity between petrous process of the sphenoid and the lingula of the sphenoid. The entire course of the carotid artery within the petrous portion of the temporal bone is clearly visible on CT images, but is perhaps most reliably evident as a circular opacity just medial to the styloid process.

Blood drains from the brain through a series of dural venous sinuses. These sinuses are lined with endothelium and are located between the periosteal and meningeal layers of the dura. The superior sagittal sinus begins at the crista galli, travels along the superior margin of the brain, and terminates near the internal occipital protuberance at the confluence of sinuses. The straight occipital, and transverse sinuses intersect the superior sagittal sinus at

the confluence. The inferior sagittal sinus follows the cerebral falx, and is considerably smaller than the superior sagittal sinus. The inferior sagittal sinus and the great cerebral vein combine to form the straight sinus, which runs posteriorly along the falx cerebri until it unites with the transverse sinuses at the confluence of sinuses on the posterior cranial wall. The transverse sinuses extend laterally from the confluence of sinuses within grooves that traverse the occipital bones. The blood first drains into the lateral sinuses, and then courses laterally and anteriorly toward the posterior boundary of the petrous part of the temporal bone. The sinuses then track medially and inferiorly along an s-shape (forming the sigmoid sulcus), and eventually drain into the jugular veins. The sigmoid sulci are clearly visible as the postero-lateral projections of the petrous pyramids. The jugular foramina form at the medial extent of the sigmoid sulci of the infra-cranial surface of the mastoid portion of the temporal bone. The petrous bones are notched to form the jugular fossae, which contain the superior bulbs of the jugular veins. The foramina travel anteriorly, laterally, and inferiorly between the petrous and occipital bones, and their antero-lateral borders pass just posterior to the carotid canals. Thus, the foramina lie medial to the external auditory meatuses and are nearly level with their inferior borders. The foramina are traditionally thought to be completely or partially subdivided by the jugular spines into the antero-medial pars nervosae, and postero-lateral pars vasculari. However, recent publications have suggested that these compartments are frequently subdivided by dural bands rather than actual bony spicules (Tekdemir

et al., 1998). Nevertheless, these subdivisions are unequal in size; the pars vascularis is considerably larger. The inferior petrosal sinus and an ascending branch of the glossopharyngeal nerve (cranial nerve IX) travel in the pars nervosa. The inferior petrosal sinus then drains the cavernous sinus and travels through the petro-occiptal fissure to exit the pars nervosa and drain into the internal jugular vein beneath the jugular foramen. The pars vascularis contain the jugular bulbs, as well as the vagus (X) and spinal accessory (XI) nerves, and some lymph vessels. Branches of the vagus nerve called the auricular branches of Arnold, exit the lateral wall of the jugular foramina and travel to the external ear via the mastoid canaliculi. The entrance to the tympanic canaliculi for the tympanic branches of the glossopharyngeal nerves into the tympanic cavity are located on the ridge of bone separating the jugular foramina from the carotid foramina. Antero-medially from the jugular foramina, the articulations between the petrous temporal and occipital bones extend forward and medially toward the apices of the petrous bones and foramen lacerum.

Endocranially, the jugular foramen lies between the posterior border of the petrous temporal bone and the jugular notch in the occipital bone. The jugular tubercle, a ridge on the occipital bone is located just medial to the foramen endocranially and abuts a groove for the ninth, tenth, and eleventh cranial nerves passing to the intermediate division of the jugular foramen. The variable presence of a notch for the ninth cranial nerve has been recently described. Tekdemir et al. (1998) describe a notch between the internal

acoustic meatus and the hypoglossal canal that they identified on CT scans as a glossopharyngeal recess, rather than a cochlear recess or triangular depression as it had been previously described. This notch was associated with variation in the path of the IX nerve within the jugular foramen. In 18.75% of specimens the nerve made a genu and then passed through a complete bony canal, and an additional 12.5% made the same genu, but then passed through an incomplete bony canal. The nerve made the same genu in all remaining specimens, but did not then pass through a bony canal at al. Tekdemir et al. describe considerable variation in the location of the canals for the tympanic and auricular nerves. They also describe the canal as being an "acute-angled" triangle, of which the apex was pointed antero-medially" (Tekdemir, 1998: 560).

Embryology

The development of the temporal bone requires the complex interaction of several different embryonic tissues. The process initiates with the development of the membranous labyrinth in the tympanic region of the developing skull between weeks three and 25 of gestation. Neural crest cells contribute to the development of a neuroectodermal placode that gives rise to the labyrinth beginning in the third week. This stage in the development of the ear occurs within bilateral dorsolateral thickenings at the level of the myencephalon region of the hindbrain. The placode cells that form the ears arise from the neuronal folds in a manner similar to the cells of the neural tube, but differ in that they remain in the surface ectoderm once the neural tube

closes, rather than being incorporated directly into the tube itself. Beginning at week seven, the ossification centres for the squamous portion of the temporals arise, by intermembranous ossification from the mesenchyme, followed by the first ossification center for the tympanic region, which appears at around week nine. Between the ninth and fifteenth weeks development centers around the formation of the otic capsule. During this time the ossification centers that form the tympanic ring also begin to fuse (Anderson 1960). The developing otic capsule will eventually account for most of the petrous and mastoid parts of the temporal bone; it develops endochondrally from paraxial mesoderm with the mesenchyme that is derived from the neural crest. This process involves the dropping of each of the placodes beneath the surface of the ectoderm, forming the earliest stage of the otic capsule, referred to as the otic/auditory vesicle. In the next few weeks, a portion of the vesicle is separated from and forms the endolymphatic appendage. The remaining part of the vesicle is further separated into dorsal and ventral parts. The dorsal part ultimately develops into the vestibule, utricle, and semicircular ducts, and the ventral part develops into the cochlea, cochlear duct, and the saccule. The membranous labyrinth is completely formed by week 25. By week 30, the tympanic cavity is nearly complete, with the exception of its lateral wall, and by week 35, the posterior segment of the tympanic ring fuses to the squamous portion of the bone.

The petromastoid portion increases in pneumatization during this time as well. The styloid process and auditory ossicles develop endochondrally from

pharyngeal arch tissue during this time, as the middle ear spaces develop from various of the embryonic grooves and pouches. The primordium of the tympanic cavity and auditory tube first appear at around 5 weeks. Both of these structures develop from the tubotympanic recess, a depression in the primitive pharynx that develops from the first and second pharyngeal pouch. The external auditory meatus eventually arises from the first pharyngeal groove. The ear ossicles also develop from the pharyngeal arch tissue near this area (in the pharyngeal groove between the tubotympanic recess and the external surface). The cartilaginous otic capsules begin to appear as buldges in the base of the cartilaginous cranium between the 8th and 9th weeks. These capsules develop from the mesenchyme tissue that surrounds the otic vesicles, and ultimately divide into cochlear and canalicular parts separated by a sulcus. At the same time, they become associated with the both the basioccipital and the sphenoid bones. The subarcuate fossa, endolymphatic foramen, and the beginnings of the semicircular canals begin to develop from the canalicular part shortly thereafter. The internal auditory meatus forms as a wide canal around the VIIth and VIIIth nerves also at around this time.

Shortly after this process, the lateral and superior boundaries of the capsule begin to appear with the earliest development of the mastoid process and tegmen tympani (Bast, 1930). Neither the facial nerve nor the carotid artery has been incorporated into the capsule at this time. Until the 11th week, the capsule undergoes a transformation that involves both the development and the

resorption of the capsule. While portions of the capsule continue to incorporate the developing structures of the middle ear, part of the capsule resorbs to facilitate the development of the fluid filled cavities within which the membranous labyrinth will arise. This process ends with the completion of the capsule that surrounds the semicircular ducts at around 11 weeks.

During the enlargement of the tympanic cavity, the tympanic membrane begins to develop with contributions from the epithelium of the cleft, the mesenchyme in which the ossicles are embedded, and from the epithelium of the pouch. The ossicles continue their development from a mass of blastemal cells attached to the first and second arches. Each of the ossicles is represented by a cartilaginous precursor by the 8th week (Anson et al., 1948). Contrary to the classical view that all three ossicles developed from a common mesenchymal origin, the head of the malleus and body and short crus of the incus arise from the first arch tissue, but the manubrium and long crus of the incus, and the head and crura of the stapes arise from the second arch (Anson et al., 1948). In addition, the footplate of the stapes develops from the otic capsule, and a portion of the malleus develops by an intramembranous process. The ossicles each reach their adult size and morphology by the 15th fetal week, and the ear has reached essentially adult form prior to the second half of fetal life. At about the 9th week, the styloid process begins its inferomedial extension from the chondrocranium. This happens as the cartilage of the second pharyngeal arch attaches to the otic capsule. At this point, most of the internal

components of the temporal bone associated with the structures of the inner and middle ear exist as cartilaginous precursors to their adult forms, but have yet to ossify.

Ossification of the temporal bone varies dramatically between the various regions of the bone. Whereas the osseous labyrinth, auditory ossicles, tympanic ring and surrounding otic capsule attain their adult size and morphology by fetal midterm, and undergo no subsequent change either in size or shape, the tympanic, mastoid, and squamous parts change dramatically postnatally, in association with the growth and development of the remainder of the cranium. Once the cartilaginous precursors to the otic capsule and its constituents have reached their adult size, the ossification process begins. The bony labyrinth is the first part of the petrous bone to begin to ossify (by endochondral ossification), followed by the otic capsule and some of the surrounding extracapsular regions.

The capsular portion of the petrous portion of the temporal bone is unique in that it develops from primitive, avascular bone, rather than the haversian bone that comprises the remainder of the petrous bone (Bast,1930; Spoor, 1993; Bonaldi et al., 1997). As a result, the bone of the otic capsule is not subject to the same remodeling processes that the remainder of the temporal bone and cranium undergo (Bast, 1930; Scheuer and Black, 2000). The ossification process of the otic capsule involves as many as 14 different ossification centers, and spans only a short period (generally between 16 and 23 fetal weeks). The

bone from the various ossification centers fuse with one another such that no suture lines are visible. Changes in the size and shape of the bony otic capsule are no longer detectable beyond the 24th fetal week. At birth, only two parts, the petromastoid and squamotympanic remain, and these fuse together by the end of the first year. The anterior and posterior tympanic tubercles also begin to develop during the first year.

Ossification proceeds in the remainder of the petrous bone such that it is recognizable as a petrous bone by about midterm. Early in the ossification of the petrous, the semicircular canals are exposed superiorly, and the internal acoustic meatus is smaller and narrower than the subarcuate fossa posterior to it. The round window, facial foramen, and walls of the middle ear are each present in the earliest stages. In addition to the exposure of the semicircular canals at this point, each of the walls is incomplete, and the carotid artery is not yet incorporated into the inferior surface, instead passing within a groove. Ossification in the area of the jugular foramen tends to move posteriorly toward the future mastoid portion. The rest of the ossification process of the extracapsular parts of the petrous bone continues by extension of the surrounding periosteum, forming the roof of the middle and inner ears, tegmen tympani, antrum, and walls of the auditory tube by about week 23. The floor of the middle ear ossifies between weeks 24 and 29 from the extension of the jugular plate. The internal auditory meatus increases in size relative to the subarcuate fossa, along with the development of the carotid canal, jugular fossa,

auditory tube and mastoid into late fetal life. By week 30, ossification of the tympanic cavity is complete, followed at about 35 weeks, by pneumatization of the extracapsular parts of the petrous bone. The pneumatization process accelerates with the replacement of amniotic fluid with air following birth, and continues through childhood, and at the petrous apex, until early adulthood.

The first ossification of the tympanic part of the petrous temporal bone begins at about week 9, between the first and second pharyngeal arches. Four separate centers of ossification arise around the future tympanic ring in a semi-circular pattern. By midterm, the tympanic ring is recognizable in isolation, but is deficient superiorly at the tympanic incisure. By the 35th week, the ring has achieved roughly its adult size and proportions, and has begun to fuse to the squamous part of the petrous bone. At birth, the ring is attached firmly to the squamous part at the root of the zygomatic anteriorly, and the scutum posteriorly. During this time, ossification of the squamous part of the temporal bone has proceeded (from about the 7th week) from a single center at the base of the zygomatic process. The squamous portion is recognizable by about midterm as a thin plate of bone located just laterally to the upper parts of the incus and malleus with a serrated border and the initial emergence of the zygomatic process. The styloid process has also begun to ossify endochondrally, in concert with the other regions of the petrous portion of the temporal bone. This process begins at the base of the styloid process, referred

to as the tympanohyal and continues at several centers, through about the fourth year of childhood.

Following birth, the first five years are broadly characterized by growth in size of the various parts of the temporal (Eby et al., 1986). In particular the mastoid bone increases greatly in size during this time. By the time fetus has reached the perinatal period the squamous and tympanic segments have fused together tentatively, as have the petrous and mastoid portions, but the two resultant segments generally remain independent at birth (Eby et al., 1986). Early in the perinatal period, these two segments begin to fuse. The fusion of the squamotympanic and petromastoid segments takes place simultaneously at a number of locations, beginning with the medial surface of the squamous part to the lateral edge of the tegmen tympani. This is later referred to as the internal petrosquamous suture (Dahm et al., 1993). The development of the petrosquamous suture continues with the fusion of the mastoid and squamous parts, and often remains visible into adulthood. The most inferior portion of the tympanic ring then fuses to the semilunar crest along the inferior border of the tympanic cavity.

Bone growth around the tympanic ring following its fusion to the tympanic cavity proceeds laterally around its circumference. This eventually results in the development of the bony external auditory meatus (Anson et al., 1955). Early in this process a second foramen referred to as the foramen of Huschke arises beneath the original meatus, and disappears again with further lateral

ossification of the meatus at around 5 years in most individuals. Lateral growth of the meatus continues into childhood, and changes its orientation relative to the rest of the cranium, from an original horizontal alignment to a more vertical orientation by the fifth year. Enclosure of both the base of the styloid process and the internal carotid artery progress in concert with the lateral extension of the meatus as well. Various parts of the superior and inferior border continue the process of ossification into puberty (Anson et al., 1955). A significant decrease in growth activity occurs at about 6 months, after which the greatest growth in size of the temporal bone occurs in the mastoids (Simms and Neely 1989; Bach-Petersen and Kjaer, 1993). The length of the mastoid grows during two separate periods, gradually until about 7 years, and more dramatically during puberty (Dahm et al., 1993). Though gradual growth continues in the external auditory meatus until adulthood, the vast majority of its gain in size occurs before the sixth month. On the other hand, the squamous part grows rapidly along with the cranial vault during the first four years, and continues at a much slower pace until adulthood (Eby et al. 1986; Dahm et al., 1993). The progression by which the styloid process grows and ossifies to the surrounding petrotympanic bone is variable, contributing to the variable size and shape of the styloid process in adult crania (Simms and Neely, 1989).

EVOLUTION OF THE HUMAN TEMPORAL BONE

Comparative anatomy among the vertebrates

From a comparative anatomical perspective, the temporal bone represents a small piece of a larger mosaic of change that characterizes the evolution of the mammalian skull. In fact the skull itself has a variable definition in comparative anatomy, referring in its broadest sense to the complex of bones that comprise the skeletal components of the head, and more specifically, a highly specific set of bones that varies according to the class of animal observed. The transition of some reptiles to novel environmental constraints and subsistence patterns precipitated adaptations of the cranial complex. Various of the bones of the skull underwent transitions in both function and anatomy in response to these variables. The temporal bone is part of the mammalian response to these changes. The focus of research into the form and function of the temporal bone relates to its role in the evolution of mastication, hearing and balance.

The unique components of the mammalian temporal bone are its fused otic capsules, tympanic bullae, and squama. Considerable variability in each of these components is seen in the mammals, but the constituents, and their pattern remain generally the same. For example the tympanum varies greatly among mammals, forming a bulla in some, and not in others, but is nevertheless present in all mammals. The walls of the tympanic cavity are comprised to variable degrees by extensions of surrounding bones. The tympanum usually

contains two bones of its own, the ectotympanic (often referred to simply as the tympanic), and the entotympanic. The ectotympanic is a dermal bone that forms most, if not all of the entire ring of bone that supports the tympanic membrane. The ectotympanic also contributes to the walls of the external auditory meatus. The entotympanic, on the other hand is a cartilage-derived bone that is a derived characteristic in mammals, and is not present in lower vertebrates. This bone comprises most, or all of the walls of the mammalian tympanic bulla.

The most important transitions that distinguish the mammals from the rest of the vertebrates have to do with the auditory and vestibular complexes, and incorporate changes of the masticatory apparatus, specifically, the mandible. Most of the elements of the skull that are diagnostic of the mammals have analogs in the more primitive vertebrates. The auditory and vestibular systems of the mammalian ear complex are essentially modified phylogenetic remnants of the branchial apparatus of aquatic and amphibious organisms that use the system as a means to monitor their spatial orientation in the water. Each of the components of the human inner ear has an analog in the fish and amphibians. The fluid-filled ampullae that appear along the lateral line of fish and act as a motion sensing system in the water gave rise to the first semicircular canal in the hagfish. The hagfish begins the succession of organisms that is generally referred to in explanations of the evolutionary development of the mammalian ear (Janvier, 1996). These primitive fish have a recognizable utricle, and

superior and posterior semicircular canals. This condition represents the first true vestibular system.

The cartilaginous fish, including sharks, were the first to develop all three semicircular canals in the Cambrian period (542 mya-488 mya). They were also the first to incorporate their labyrinth into an enclosed capsule that is specifically associated with the cranium. However, the canal system in the cartilaginous fishes differs from that of mammals in that the canals communicate with the outside environment through endolymphatic spaces. The semicircular canal system was first closed to the outside environment, and filled with endolymph rather than seawater in the teleosts during either the Ordovician or Devonian period (416 mya-359 mya)(Webster et al., 1992). Interestingly, many of these changes are recapitulated in the ontogeny of the human temporal bone.

The evolution of auditory function in mammals differs from that of all other vertebrates (Popper and Fay, 1992). Mammals bear the most resemblance to, and are believed to have evolved from the therapsids, a class of reptiles from the Permian and Triassic periods about 250 million years ago (Romer and Parsons, 1986). Several components of the mammalian ear have anatomical analogs in the reptiles that are not associated with hearing. Evolution transformed the reptilian first mandibular arch into ear ossicles in the mammals, rather than into jaws as is the case in all other vertebrates. The mammalian incus evolved from the much larger reptilian quadrate, and the stapes is the remnant of the columella auris of reptiles (derived from the hyoid arch). The

malleus of mammals is essentially analogous to a reduced articular bone of the lower ancestral vertebrates. In fact, the articulation between the incus and the head of the malleus is derived from the articulation between the lower jaw and the quadrate in non-mammalian vertebrates. The removal of this articulation to the inner ear in mammals necessitated the development of a different point of articulation between the bones of the mammalian jaw.

The remainder of the non-mammalian lower jaw, the dentary, represents the entire mammalian jaw, and articulates directly with the squamosal adjacent to the ossicles (previously part of the jaw articulation). The transformation of the reptilian jaw is thought to have taken place in the therapsids, which are mammal-like among the reptiles (Hyman, 1961; Romer and Parsons, 1986). The general trend is toward greater significance of the dentary. The dentary increases in its posterior extension beneath the squamosal, close to the primitive location of the jaw articulation, and superiorly beneath the temporal region where it eventually develops an attachment site for the temporal muscles (Romer, 1967). Concomitant changes characterize the other elements of the primitive jaw in a trend toward their movement from the reptilian jaw complex to the mammalian middle ear auditory apparatus. These changes are part of a broader reconstruction of the masticatory complex that characterizes the evolution of the mammals in relation to their greater dependence on a consistent food source as a means to attain a more steady body temperature (Romer and Parsons, 1986: 272). The end result is a pattern seen only in mammals, in

which the jaw articulation is comprised, both superiorly and inferiorly, of intramembranous bones as opposed to endochondral bones (Colbert and Morales, 1991).

Paleoanthropology

The temporal bone is the site of considerable scholarship in paleoanthropology, both because of its resistance to taphonomy and its variable structure and orientation through hominid evolution (Weidenreich, 1943; Le Gros Clark, 1947; Tobias, 1967; Dean and Wood, 1981; White et al., 1981; Kimbel et al., 1984; Lockwood et al., 2002; Sherwood, 2002; Harvati, 2003; deRuiter et al., 2006). There are a number of trends that characterize the evolution of the hominid temporal bone, and a number of changes to other parts of the skull that are undoubtedly related to temporal bone change, that can not be ignored. Hominid evolutionary change in the cranium is characterized by: (1) an increase in cranial capacity, (2) decreased prognathism, (3) forward movement of the foramen magnum, (4) a decrease in basioccipital length and hence cranial base length, (5) more horizontal orientation of the foramen magnum in concert with a horizontally expanded nuchal area with reduced musculature, (6) flexion of the cranium in the sagittal plane and (7) movement of face beneath the vault (Aiello and Dean, 2002). Each of these trends involves changes throughout the skull, including the temporal bone.

The petrous portion itself is the site of significant gross morphological variations in form that signify anatomical distinctions between the cranial bases

of modern humans and their ancestors (Spoor et al., 1994). The anatomy of the hominid skull is a morphological mosaic that is reflective of changes associated with an increase in brain size, changes in posture associated with bipedal locomotion and changes in the masticatory system (Aiello and Dean, 2002). It is often difficult to differentiate the relative influence of each of these factors on morphology of the hominid cranium.

As viewed in norma basilaris, the cranial base, effectively displays the majority of the changes associated with trends listed above. Its form is dictated primarily by the relationship between brain size and cranial base length, and to a lesser degree facial size, facial orientation, and posture (Aiello and Dean, 2002). Whereas pongids have the least flexed crania, hyperprognathism, and low petromedian angles, modern humans are characterized by maximum cranial constriction, lesser prognathism, wider petromedian angles, and marked “rolling up” of the cranial base especially in the spheno-occipital portion. Our ancestors tend to fall into various places in along this morphocline. Thus, with the exception of the robust specimens, the australopithecines most resemble pongids, but have made considerable divergence in each category toward the human condition. On the other hand *Homo erectus* and *Homo habilis,* with their less prognathic profiles, and wider petromastoid angles, lie within the human range.

Of course, phylogeny is never that simple. *Paranthropus boisei,* which is classified as a member of the australopithecine genus, and who has largely

plesiomorphic features, lie well within the human ranges of several features, including the greater shortening of their cranial base, and *Homo*-like glenoid fossa structure (Tobias, 1967). This does not necessarily indicate their closer relationship to humans, but rather of some sort of parallel evolutionary process that has resulted in similar morphologies for different reasons (Dean and Wood, 1981; Aiello and Dean, 1990). The range of variation in the dimensions of cranial base of *A. robustus* has recently been expanded to reflect sexually dimorphic variation (deRuiter et al., 2002).

Change in the structure of the temporal bone falls into several categories: (1) a reduction in the length of the petrous pyramids over time, (2) more transverse orientation of the petrous pyramids over time, (3) a more lateral placement of the vascular and nervous foramina in relation to the sagittal plane over time, (4) a deepening of posterior fossa, and related change in shape of posterior wall of the petrous pyramids over time (nearly vertical in humans-20-30 degrees off vertical in pongids), (5) significant changes in the depth, width and medial border of the mandibular fossa, (6) changes in the form of the tympanic bone, and (5) an increase in diameter of EAM (Dean and Wood, 2002; Harvati, 2003).

Each of these characteristics varies in concert with each of the others. Wider petromedian angles are typically associated with orthognathic facial profiles, and there seems to be a link between these two, and a third and common factor, cranial base length (Tobias, 1991). Slight lateral adjustment in

the orientation of the petrous pyramids is often accompanied by a shortening of the petrous bones, and a general shortening of the cranial base, especially in the spheno-occipital region (Tobias, 1991). There is also a relationship between brain size and the shape of the posterior cranial fossa, and hence, the variability in the orientation of the petrous bone. Dean and Wood (1981, 1982) and Aiello and Dean (1990) hypothesized that the size of the posterior cranial fossa, and hence the orientation of the petrous bones, is directly correlated to the size of the brain, specifically the cerebellum. Spoor and Zonnefeld (1998) on the other hand, suggest that coronally oriented petrous pyramids instead correlate with increases in brain volume relative to basicranial length.

Australopithecines

The cranial base morphology of the australopithecines is in many ways intermediate between that of the great apes and hominids, but overall maintains a greater resemblance to the great apes, in its long low morphology. The foramen magnum is located more anteriorly relative to the bitympanic line than in apes, but not nearly as far as is the condition in humans (Aiello and Dean, 2002). There has also been considerable widening of the various distances between the bilateral landmarks of the australopithecine cranial base relative to the great apes, but again not nearly as much as in humans. The area for muscle attachment on the nuchal portion of the skull is reduced in the australopithecines relative to the great apes, but the overall australopithecine

basioccipital musculature remains closer to the apes than to humans (Aiello and Dean, 2002).

Kimbel et al. (2004) refer to the temporal bone of *Australopithecus afarensis* as primitive in relation to even the other australopithecines. The petrous bones in the australopithecines are oriented antero-posteriorly as in the apes in spite of the movement of the foramen magnum, maintaining the approximately 60° rotation off the bicarotid line that characterizes ape morphology (Aiello and Dean, 1990). Tobias measured the angle of the petrous differently as the petro-median angle, but his result was the same. He attributes a petro-median angle of 38° to *A. afarensis*, which is nearer the great ape condition than that seen in *Homo* (Tobias, 1991). The morphology of the glenoid fossa in *A. afarensis* is described as shallow, bounded by a hint of articular eminence (White et al., 1981). The most recently described specimen (AL 442) is described as "expand[ing] the range of variation in this suite of features…" with an articular eminence that is "while certainly low by comparison to *A. boisei or Homo*, strongly delimited and set off from the roof of the mandibular fossa" (Kimbel et al., 2004: 217). Both authors agree though that overall this is a primitive morphology. "If we envision the human and great ape glenoid regions as situated at opposite ends of a morphocline, then the *A afarensis* glenoid morphology occupies the most generalized position on the morphocline of any australopithecus species" (Kimbel et al., 2004: 217).

The australopithecine tympanic element is pleisomorphic in that it is horizontally oriented, tubular in cross section, with an undifferentiated crista petrosa. The tympanic element and postglenoid process also occupy different planes, an orientation that is ubiquitous among the great apes and is considered primitive. The *Australopithecus afarensis* temporal bone displays an overall more primitive morphology than *Australopithecus africanus.*

The *Paranthropus* cranium is very wide across the tympanic plates and between the lateral extensions of the zygomatic arches. This morphology reflects their large and unique masticatory complex (Aiello and Dean, 2002). Other features of the cranial base vary from the rest of the australopithecines independently from the masticatory differences. The foramen magnum of *Paranthropus* is located considerably farther anterior than in the rest of the australopithecines for example. Indeed, It is farther forward than in Homo, being well in front of the bi-tympanic line. The foramen magnum is characteristically heart-shaped in *Australopithecus boisei* (Tobias, 1967). The reduced muscle markings of both the nuchal and basioccipital regions in paranthropus set them apart from either the great apes or the gracile australopithecines (Tobias, 1967; Aiello and Dean, 2002).

The petrous bones in the robust australopithecines lie in the same axial plane as the tympanic plate. Overall, the petrous bones in all of the Paranthropus specimens are oriented in a pattern much more like *Homo* than either the great apes or the remainder of the australopithecines (Lieberman et

al., 2000). They are oriented at approximately 45° from the coronal plane, and 35° from the tympanic plane, placing them in a much more medio-lateral relationship to the rest of the cranial base. In SKW 18/SKW 52, the petrous bones are oriented at approximately 40° from the coronal plane (de Ruiter et al., 2006).

The glenoid fossa of the robust australopithecines is located approximately half way beneath the braincase. The fossa differs from the gracile australopithecines in that it is antero-posteriorly shorter even though it is of similar width. The fossa is deeper in *A. robustus* with a larger articular eminence. The post-glenoid eminence is smaller and merges with the tympanic plate. The glenoid fossa in *A. boisei* is unique among the robust australopithecines in that it is even more forshortened and derived, and there is typically only 10mm separating the articular eminence from the post-glenoid process (Tobias, 1967). The derived morphology of the *A. boisei* temporomandibular joint suggests that it accommodated considerable transverse movement of the mandible. The medial limit of the fossa in *A. boisei* is characterized by an extensive medial glenoid plane that does not restrict medial movement of the mandibular condyle as the entoglenoid process does in the great apes. Rather, this morphology allows for the transverse movement of the condyle within the fossa (Tobias, 1967). Overall, much of the *A. robustus* petrous endocranial surface anatomy is indistinguishable from moderns, including morphology of the subarcuate fossa, orifice of the cochlear canaliculus,

and the slit like configuration of the orifice of the aqueduct of the vestibule (de Ruiter et al., 2006).

The morphology of the robust australopithecine tympanic element also approximates the morphology that characterizes modern humans. The tympanic plate is upright in orientation, with increased infero-superior depth. The orientation of the tympanic axis is markedly oblique. There is also a further reduction of the gaps between the coronal planes and the anterior face of the mastoid relative to the remainder of the australopithecines. The crista petrosa is sharp and projecting in shape, and there is significant reduction in the size of the post-glenoid and eustachian processes.

As noted above, *Australopithecus boisei* is unique with regard to temporal bone morphology. These specimens show very large mandibular fossa, both medio-laterally and antero-posteriorly. In fact "it is in *A. boisei* that we encounter a truly metamorphosed glenoid region, one that diverges sharply from the relatively plesiomorphic glenoid region of all other australopithecine species…" (Kimbel et al., 2004: 160). Other unique features of the *A. boisei* glenoid fossa include very deep articular fossae, a mediolaterally restricted preglenoid plane that is also steeply inclined superiorly, an articular eminence that "twists about its transverse axis so that it medially faces almost completely posteriorly" (Kimbel et al., 2004: 160), and an entoglenoid process that is "rocked backward" so that its apex is oriented posteriorly, and overlaps the tympanic element, thus creating the "medial glenoid plane" (Kimbel et al., 2004: 160). Kimbel et al.

(2004) go on to say that *A. boisei* represents the most derived position on the morphocline of the australopithecine glenoid region**,** at the opposite end of which is *A. afarensis*. *A. boisei* shows a greater degree of vertical relief from the sagittal view, than *A. robustus* or the other australopithecines. Overall, *A. robustus* is more plesiomorphic in glenoid and tympanic morphology than is *A. boisei* (Kimbel et al., 2004: 165), and with the exception of the lateral extension of the tympanic, the *A*. *boisei* cranial base, closely resembles *Homo*. "*A. boisei* can be located at the extreme derived end of the morphocline by virtue of its uniquely transformed glenoid region: coincidence of the summit of the articular eminence and posterior edge of the temporal foramen; lateral to medial twisting of the articular eminence such that the entoglenoid process points posteriorly; further deepening of the mandibular fossa, with the deepest point positioned above the FH, and flattening of the tympanic plate to form part of the ceiling as well as the posterior wall of the mandibular fossa its inferior margin blending with the anterior face of the pars mastoidea. It "ranks with its face as one of the most autapomorphic cranial regions in the genus *Australopithecus*" (Kimbel et al 2004: 167).

Australopithecus aethiopicus lacks many of the specializations of the glenoid region, and as such is considered as an intermediate between *A. boisei* and the more plesiomorphic *A. afarensis.*

Genus *Homo*

The *Homo* cranium is marked by overall antero-posterior shortening, accompanied by mediolateral widening, an orthogonal facial profile, and maximum sagittal flexion (Aiello and Dean, 2002). As such, the petro-median angle is largest in *Homo* among all hominids, and the medio-lateral length of petrous pyramids is smallest in *Homo*. Additionally, the occipital squama is much larger, and horizontally oriented as a result of the larger brain (Aiello and Dean, 2002). However the musculature of this larger nuchal area is much reduced in comparison to either the apes or the australopithecines (Lieberman et al., 2000). As a result of the enlarged occipital area and the downward drift of the posterior cranial fossa, the posterior wall of the petrous bone in humans is nearly vertical (Aiello and Dean, 2002). The foramen magnum is more anteriorly placed than the great apes and australopithecines, except for the robust australopithecines. In keeping with overall reduction in masticatory musculature, the bizygomatic and bitympanic breadths are greatly reduced in modern humans, but remain of intermediate breadth among early *Homo* remains. The foramina associated with both nervous and vascular supply are all located more laterally in relation to the midline of the cranium. The overall appearance in norma basilaris, of the *Homo* skull, is antero-posteriorly short and wide relative to that of the great apes and australopithecines (Lieberman et al., 2000; Aiello and Dean, 2002).

The *Homo* mandibular fossa is unique in that it is antero-posteriorly compressed, deeper and shorter in lateral view than in the apes or australopithecines. *Homo* and the australopithecines, including *Paranthropus boisei*, are distinguished by length-breadth indices of the mandibular fossa. This variation has been attributed to the "fact that in the ape growth appears to take place in all directions, whereas in man relatively less growth occurs in the anteroposterior axis of the fossa than in other directions" (Petrovits, 1930: 46, cited by Tobias, 1967: 36). Nearly completely underneath the cranial vault, the location of the fossa, is unique to the genus *Homo* (Aiello and Dean, 2002). The Postglenoid process is also greatly reduced in *Homo*. The postglenoid process and tympanic element occupy the same vertically oriented plane. In basal view the lowest extension of the postglenoid process is hidden by the tympanic element. The *Homo* tympanic plate assumes the shape of a vertically oriented plate with sharp upper and lower margins. The plate is concave both medio-laterally and infero-superiorly and forms a single anteriorly directed face.

Homo neanderthalensis

The temporal bone is the site of some of the most diagnostic features of the distinction between Neanderthals and modern humans (Harvati, 2003). Most of these features are non-metric and thus difficult quantify, but are well documented nevertheless. One of the most significant distinctions between Neanderthals and both Homo erectus and modern humans is the size of their mastoid processes, which are considerably smaller than either of the other

Homo species (Boule and Vallois, 1957; Stringer et al., 1984; Stringer, 1985; Dean et al., 1998). The squamous portion of the Neanderthals is superior-inferiorly low and short antero-posteriorly in comparison to modern humans (Boule and Vallois, 1957; Heim, 1976; Harvati, 2003). The zygomatic processes of Neanderthals are more robust, and project farther laterally and posteriorly than in modern humans (Boule and Vallois, 1957; Heil, 1976; Harvati, 2003).

There are also features of the petrous portion of the Neanderthals temporal bone that distinguish it specifically from modern humans, and from *Homo erectus*. For instance, the Neanderthals glenoid process is wide, shallow and medially circumscribed relative to modern humans (Vallois, 1957). The relative location of the external auditory meatus, glenoid fossa, and zygomatic process are also unique in Neanderthal specimens (Vallois, 1969; Stringer, 1984; Harvati, 2003). The EAM is elevated superiorly in relation to these other features giving the Neanderthals temporomandibular region a more compact appearance. The orientation of the tympanic, and the origin of the petrotympanic crest are also different among Neanderthal specimens than in modern humans (Vallois, 1969; Condemi, 1992; Schwartz and Tattersall, 1996; Harvati, 2003). The petrotympanic crest originates at inferior-most projection of the tympanic, and the tympanic bone as a whole is situated in a more coronally oriented plane among Neanderthal specimens than in modern humans. Harvati (2003) recently quantified various of these features using three dimensional geometric morphometrics in an attempt to compare them to modern humans

collectively. Her results indicate that when not corrected for size, Neanderthals fall within the range of modern human variation in the 15 measurements used in her research. Her basic characterization of the shape of the Neanderthal temporal bone is that the lateral-most landmarks of the Neanderthal cranium are significantly more laterally located than modern humans, that the Neanderthal tympanic area is more coronally oriented, and that the mastoid processes are significantly smaller than in modern humans (Harvati, 2003).

She found more specific variation in the shape of the Neanderthal temporal bone using principal components analysis and canonical variates analysis. The two late Paleolithic specimens in her sample were distinguished along one component from both modern humans and the Neanderthals in the more inferiorly located parietal notches, more superiorly located asterion, more posteriorly located anterior margin of the jugular fossa, and more superiorly located petrotympanic crest. There was significant variation between modern humans and Neanderthals along a single principal component (Harvati, 2003). This variation was characterized by a more anterior location of the origin of the petrotympanic crest, a more anteriorly located asterion, more superiorly and anteriorly placed mastoid process extensions, and more inferiorly located juxtamastoid eminences (Harvati, 2003). Canonical variates analysis of the same data also separated Neanderthals from modern based on a similar set of characteristics. There is significant difference in the location of the superior aspect of the zygomatic suture, which is more superiorly located in Neanderthals

than in modern humans, as is auriculare, which is also more laterally located. The articular eminence on the other hand is located more inferiorly (Harvati, 2003). The lateral origin of the petrotympanic crest was again located anteriorly and the crest extended farther posteriorly relative to the modern humans in the sample. Finally canonical variates analysis also indicated that the tip of the mastoid process were located significantly more superiorly relative to modern humans indicating significantly smaller mastoid processes among the Neanderthal specimens (Harvati, 2003). The supramastoid crest is also considered robust in the Neanderthals relative to modern humans (Boule and Vallois, 1957).

The most significant distinction between Neanderthal and modern human temporal bone morphologies illustrated by Harvati is in the placement and orientation of the tympanic. Most of the characteristics of the Neanderthal tympanic are thought to represent traits retained from *Homo erectus* (Harvati, 2003). As in the Asian *Homo erectus* fossils (Andrews, 1984), Neanderthal crania have a petromastoid fissure at the junction of the anterior and posterior portions of the tympanic element (Trinkaus, 1983; Dean et al., 1998). The lateral origin of the crest is laterally located at the inferior-most point of the tympanic tube among the Neanderthal specimens (Harvati, 2003). The orientation of the crest is coronal in comparison to humans and the attached vaginal plate of the styloid process is shorter supero-inferiorly and less plate-like than in modern humans. These results were largely corroborative of previous

non-metric characterizations of Neanderthal temporal bone morphology. However, the canonical variates analysis maximized the difference between the species and demonstrated the extent to which they differ. In fact the canonical variates analysis suggests that there is no overlap in the variation of the characteristics listed above when size is controlled for (Harvati, 2003).

There are a number of publications describing the surface characteristics of *Homo erectus* temporal bone and the features that distinguish it from modern humans and Neanderthals (Andrews, 1984; Kennedy, 1991; Delson et al., 2001), as well as particular variation in the bony labyrinth (Spoor and Zonnefeld, 1994, 1998; Spoor et al., 2003). For example, both modern *Homo sapiens* and *Homo erectus* have larger mastoids than do Neanderthals, but erectus mastoids project dramatically medially as the progress downward as opposed to the vertically downward extension of the mastoids in modern humans (Aiello and Dean, 2002).

Much of the research into the craniometric uniqueness of *Homo erectus* focuses on the extent to which *Homo erectus* crania vary across their range, and the implications of this variation for phylogenetic characterization of this variation (Andrews, 1984; Stringer, 1984; Anton, 2002, 2003; Kidder and Durband, 2004). These articles each suggest that since certain traits were present on Asian *Homo erectus* specimens, and not on African specimens, that the two groups should be considered different species (Andrews, 1984; Stringer, 1984; Kidder and Durband, 2004). Kidder and Durband (2004) that these traits do not

represent species level variation between the Asian and African fossils, and Kennedy (1991) suggests that they are not even autampomorphic of *Homo erectus* in general.

Some of these authors have also addressed variation in cranial thickness between *Homo erectus* specimens (Kidder and Durband, 2004), and between *Homo erectus* and other hominids (Kennedy, 1991). Increased cranial vault thickness has been found to characterize Homo *erectus* specimens relative to modern humans and australopithecines. Thickened cranial vault bone is also found amongst Neanderthal specimens although to a lesser extent than in *Homo erectus (*Kennedy, 1991*)*. Kennedy (1991) argues that the presence of thickened vault bone in groups other than *Homo erectus* prevents the trait from being considered autapomorphic of *Homo erectus*. She argues instead that that cranial thickness in hominoids is related to one of two factors depending on its location on the skull (Kennedy, 1991). She suggests that the increased thickness of the superior portion of the cranial vault is a derived trait, both for *Homo erectus* and for most other hominids except modern humans. However, thickness of the inferior bones of the vault, including the squamous temporal bone, instead reflect retention of pneumatodiploic bone. Interestingly, inferior vault thickness among the *Homo erectus* specimens more closely resembles the australopithecines, and is considerably greater than in the Neanderthals and most other non-modern hominids including modern humans (Kennedy, 1991). Kennedy argues that this trend in vault thickness precludes the classification of

Homo erectus as a valid independent species as it is presently defined, but that "that the challenge to the taxon of *Homo erectus* rests less with the biological reality of such a group than with the present taxonomic configuration of middle and early upper Pleistocene hominids" (1991: 375).

There has also been considerable recent attention given to the pattern of pneumatization that characterizes *Homo erectus* temporal bone specimens particularly as it pertains to the increased thickness of the inferior vault bones of *Homo erectus*. The general trend in temporal bone pneumatization is from a more widespread pattern throughout the various segments of the temporal bone in the apes (Sherwood, 1999), and australopithecines (Sherwood et al., 2002) toward a reduced pattern of pneumatization in the genus *Homo* (Sherwood, 2002). Pneumatization in modern humans, Neanderthals and some *Homo erectus* specimens is generally limited to the mastoid and petrous regions (Turner and Porter, 1922; Schulter, 1976; Schulter-Ellis, 1979; Virapongse et al., 1985). However, the pattern differs in the Chinese *Homo erectus* specimens from Zhoukoidian in that it extends significantly into the squamous portion of the bone (Balzeau and Grimaud-Herve, 2006). The pneumatization also extends farther posteriorly in these specimens. Balzeau and Grimaud-Herve (2006) note a correlation in these specimens between the degree of squamous pneumatization and morphological variation in the vault. These specimens are characterized by wide cranial vaults and narrow occipital bones relative to either the Homo erectus fossils with lesser degrees of squamous pneumatization,

Neanderthal or modern human specimens. There is no associated variation in the overall pattern of vault bone thickness between the groups with greater and lesser degrees of pneumatization (Balzeau and Grimaud-Herve, 2006). However, the specimens with reduced squamous pneumatization also have larger endocranial widths in relative to length in comparison to the Zhoukoudian fossils (Balzeau and Grimaud-Herve, 2006). Balzeau and Grimaud-Herve attribute this variation to "an opportunistic phenomenon [whereby] the cavities extend, [but] the bony structures show resorption while maintaining sufficiently resistant structures" (2006: 13). They suggest that this opportunistic phenomenon indicates that pneumatization of the temporal bone is not a determinant of cranial base shape variation, rather that the cells propagate into available areas based on availability of space resulting from shape variation (Balzeau and Grimaud-Herve, 2006). This pattern is supported by the relatively greater pneumatization of the larger mastoid processes and reduced pneumatization of the thinner squamous portions in modern humans. In other words, variation in pneumatization in hominid evolution results from changes in the morphology of the bones that constrain it, not the other way around. Kidder and Durband (2004) suggest that there is not sufficient metric variation in the dimensions that Balzeau and Grimaud-Herve (2006) associate with variation in pneumatization, to consider the Asian and African *Homo erectus* specimens as different species.

The following discussion considers human temporal variation in the context of hominid evolution. Harvati (2003) refers to the typical modern human "landmark configuration [as being] characterized by a medio-laterally narrow tympanic area and glenoid fossa, a sagittal orientation of the petrotympanic crest, and large mastoid processes" (2003: 332). Lockwood et al. (2002) refers to this as "medio-lateral compression of the tympanic and mastoid parts" of the temporal bone (2002: 453). They also note this compression results in the small overall size of the temporomandibular joint, which in humans is located almost entirely beneath the braincase. This compression however refers only to medio-lateral width of the temporal bones themselves, and thus does not contradict earlier assertions by Dean and Wood (1981) that the human cranial base is broad (Lockwood et al., 2002). Lockwood et al. (2002) point out that the measurements used by Dean and Wood (1981) were largely measurements of the distance between the temporal bones, and refer to the relationship between the two theories as describing temporal bones that are themselves narrow but are laterally located on the cranial base. The breadth of the cranium referred to by Dean and Wood (1981) then results from the coronal orientation of the petrous pyramids in Humans. Compression in the preglenoid plane also results in greater depth of the human mandibular joint relative to the great apes and the other hominoids (Ashton Zuckerman, 1954; Lockwood et al., 2002). Additionally, the entoglenoid and postglenoid processes are small inferiorly relative to the great apes and hominoids.

Lockwood refers to the reduced lateral extension of the tympanic element in humans relative to the great apes and hominids as an apomorphic trait. The human tympanic crest has a more posteriorly located lateral origin at the root of the mastoid process with no tympanomastoid fissure present (Harvati, 2003). This crest continues medially to form the vaginal plate of the styloid process, and then extends obliquely to terminate at the carotid canal (Schwartz and Tattersall 1996; Martinez and Arsuaga, 1997; Harvati, 2003).

The overall lateral view of the human temporal bone has much greater topographic relief than either the great apes or the other hominoids as a result of the more inferior projection of the mastoid processes, depth of the mandibular fossa and steep posterior aspect of the articular eminence (Lockwood et al., 2002). On the underside of the cranium, the petrous element is more coronally oriented in modern humans relative to other hominoids (Dean and Wood, 1981; Strait et al., 1997; Lockwood et al., 2002).

Harvati (2001) suggests that the strong geographic clustering of human temporal bone variation in her sample likely indicative of genetic influence on these dimensions. A few articles address the origin of genetic variation in modern human the temporal bone in the context of ancestral variation (Schulter, 1976; Wescott and Moore-Jansen, 2001). The squamous portion of the temporal bone tends to be lower and longer in Native Americans than in other populations (Schulter, 1976). There is also significant variation in the diameter, depth and shape of the external auditory meatus between the races, which does

not seem to correlate with the pattern of significant variation between the races in biauricular breadth (Schulter, 1976). The relationship between the breadth of the cranium and potentially correlated variation in other characters is interesting in light of the debate regarding the potential causes of variation in mid-vault cranial breadth among other Homo genera, specifically *Homo erectus*. Schulter (1976) also found less significant variation in the inferior projection of the mastoid processes. There is also ancestral variation in the angle between the tympanic plates and the petrous pyramids (Schulter 1976).

There is a consistent pattern of sexual dimorphism among modern humans in the morphology of the temporal bone (Steele and Bramblett, 1988; White, 1991), and Harvati's results lend quantitative support to this notion. Specifically dimorphism in the temporal bone is characterized by smaller mastoid and juxtamastoid processes in females, and antero-posteriorly long zygomatic processes in females relative to males. Harvati's principal components analysis results suggest that this variation is shape rather than size related (2003). As mentioned above there are a number of studies that demonstrate that the angle between the long axes of the petrous portion and the internal auditory canal vary between the sexes (Kalmey and Rathbun, 1996; Graw et al., 2003; Noren et al., 2005).

CHAPTER V

MATERIALS AND MEASUREMENT METHODS

The raw data collected for this research are two-dimensional coordinate data taken from anatomical landmarks located on axial head CT scans. The data analyzed consist of distance measures between coordinate points. I generate these measurements by calculating the Euclidean distances between each of the landmarks. This chapter describes the methods by which both the coordinate and distance data used in this research were collected, reduced, and analyzed.

I begin with a description of the sample and the methods of coordinate data collection I used. It continues with a lengthy discussion of the precision and repeatability of both the landmarks and the measurements between them, as well as the resultant exclusion of insufficiently repeatable data. I then discuss the methods employed to examine variation in these dimensions of the petrous part of the temporal bone related to age, sex, and duration between repeat images. In the interest of continuity, I include the results of this process in this chapter.

MATERIALS ANALYZED

Axial head CT scans of 115 adult individuals (50 males and 65 females) were used in this research. Two sets of images of the cranial base of each of the individuals were analyzed to repeat a comparison of ante and postmortem

imagery. These image sets will be referred to as “repeats” in the remainder of this text. An additional smaller subset of scans from ten individuals was also collected to investigate the influence of variable slice thickness on the outcome of the analysis. The images were provided by Dr. Gill Naul, Head of Radiology at Scott and White Hospital in Temple, Texas, and only include images taken from adults who show no sign of pathological distortion of the petrous part of the temporal bone. Each of the images in the first set is the result of a routine head CT, an exploratory procedure intended to aid in the diagnosis of ailments for which the patients exhibit symptoms, or in the detection of potential injury following a traumatic accident. The images that comprise the second set are either secondary exploratory head CT’s, or are follow-up images taken after a particular treatment regimen.

The CT image sets were provided in DICOM format, and a 3mm scale was included by technicians at Scott and White hospital in each image, which I used to verify that the scale was the same for all individual image sets. The age of each individual in years was provided, as was the sex of each individual. Information regarding the length of time between the first and second scans was also provided. The Internal Review Board at Scott and White Hospital did not permit me to collect information regarding the ancestry of the individuals, preventing the analysis of ancestrally-related variation in the petrous part of the temporal bone. Several of the original scans displayed signs of pathology, either

on the first or second set, and thus I excluded them from the analysis. These individuals are not included in the sample size of 115 individuals.

The matrix size of each of the images is 512x512 pixels. Each image set contains between 20 and 36 slices, and typically encompasses the skull in its entirety, though only the slices that include at least a portion of the petrous part of the temporal bone are relevant to this particular research. The individual slices are 5mm in thickness for each of the individuals in the larger sample, and 1mm in thickness for the smaller subsample of 10 individuals. I acquired the smaller subset to investigate the potential advantages and disadvantages of smaller slices in the analysis of the petrous temporal bone. I hypothesized that the 1mm slices would reconcile some of the problems associated with the complex relationship that exists between slice thickness and the small structures of the petrous temporal bone, and would be thus preferable. However, 1 mm slices are far less frequently used in the clinical setting, and thus rarely available for postmortem analysis. On the other hand, 5 mm slices are routinely used in exploratory cranial imagery and are more frequently available for comparison. For this reason, 5 mm slices represent the bulk of the sample used in this research. The placement of the individual slices are standardized to the extent that certain morphological characteristics are represented on particular slices, and there is limited variability in the location of each slice in relation to the morphology of the skull. The parameters of repeat image collection can also be adjusted to more closely approximate slice location using a scout image. Scout

images are taken in the sagittal plane to facilitate the correct relationship between the head of the patient and the CT apparatus. Together, these procedures reduce variation in slice location between repeat images (Haaga et al., 1994; Kalendar, 2006). Nevertheless, in the current research variation in slice thickness is a likely contributor to the poor repeatability of several landmarks and measurements eliminated during the repeatability analysis.

IMAGE ANALYSIS

I used the 3D Doctor computer program (Able Software, 1993) to complete all graphic manipulation of the images, as well as to collect all coordinate data. The 3D Doctor program is an image rendering, processing and analyzing software package intended for use in clinical diagnosis and surgical planning. The program was originally developed in 1993 by the Able Software Corporation, and is intended to provide a means to visualize two and three-dimensional volume image data, derived from a variety of sources, including Computed Tomography (CT), Magnetic Resonance Imaging (MRI), microscopy, and other imaging modalities. The software employs 3D image segmentation to extract object boundaries from images and uses these data to create both 3D surface and volume rendering of two-dimensional images to allow for two and three-dimensional visualization, object measurement, and quantitative analysis. The 3D Doctor software is uniquely suited for this research because of its capabilities to extract object boundaries, precise object measurement, and quantitative analysis, each of which are intended to limit the amount of error

associated with measurements taken from medical imaging techniques, particularly CT. The software can take into account slice thickness and the resultant fuzziness of boundaries in CT imagery in order to maximize measurement accuracy. The segmentation tool of the 3D Doctor software delineates tissue boundaries at the median shade in the array of shades found at a tissue interface. This closely approximates the half maximum height procedure discussed by Spoor (1993) and others, and helps to reduce error associated with arbitrary placement of landmarks along fuzzy boundaries. The control point tool in the 3D Doctor software facilitates the extraction of coordinate data. It provides x and y values to the nearest $10{,}000^{th}$ of a millimeter and uses the slice number as a representation of the z dimension.

COORDINATE AND MEASUREMENT DATA COLLECTION

My data collection method was intended to circumvent several problems associated with the use of CT to compare of dimensional or measurement data. The most significant of these problems is associated with the repeatability of data collected from images taken at two or more times in a person's life. For instance, it cannot be assumed that measurement data collected from two CT images taken from the same person (even one immediately after the other) will align with one another perfectly. In all likelihood, coordinate data will not match in exact numerical detail between two CT images from the same person. However the use of coordinates as raw data allows one to extract of the relative Euclidean dimensions between points without retaining the actual x, y, and z

values (Richtsmeier et al., 1995). Variation in coordinate values in the x and y dimensions is effectively eliminated for the placement of both the x and y coordinates by computing the distances between points. However, variation in placement of the z dimension (represented only as a slice number) is less easily eliminated. Error in this dimension is largely the result of the interaction of slice thickness and head position and represents a considerable obstacle to the collection of reliable data in the z dimension. Additionally, the slice number, rather than coordinate data, is the only value that can be extracted for the z dimension. For these reasons, I use only the x and y coordinates in this analysis.

As mentioned in Chapter III, only some of the slices in an image set display anatomical detail that is relevant to this analysis. I did not include slices that do not display at least a portion of the petrous portion of the temporal bone. Each of the relevant slices contain some number of the total landmarks collected for this research. Since z dimension data were not included in the analysis, each of the combined landmark sets is effectively a superior-inferiorly “flattened” representation of an otherwise three-dimensional shape. The 3D Doctor program facilitates two-dimensional flattening of the images in linear space by allowing for the development of a single matrix of points that combines the landmarks collected from a series of slices, and does not perform any curvilinear corrections in the process. Control points are placed on each of the landmarks that are visible on a particular slice, and maintain their Cartesian locations in

relation to the remainder of the image as the viewer moves from slice to slice. Figure 5.1 illustrates the result of this process, which is a 2-dimensional array of points with associated x and y coordinates for each one individual in the sample.

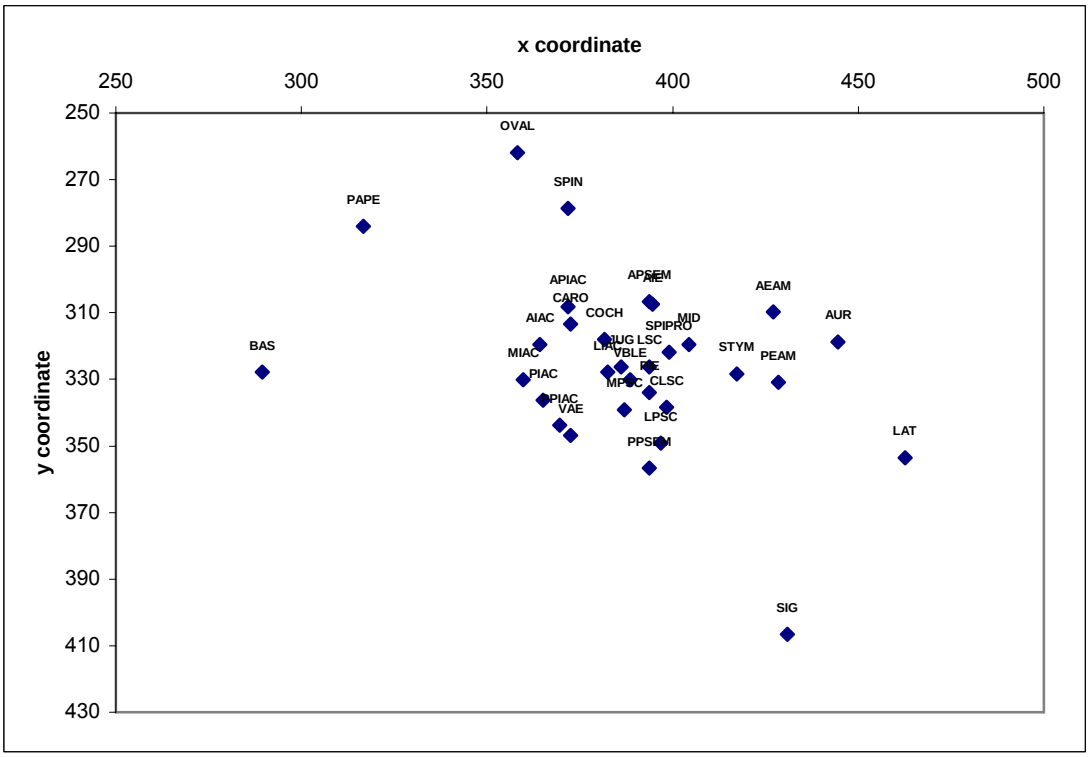

Figure 5.1. *Two-dimensional array of points for a single individual*

The process of landmark selection began with the collection of coordinate data for all landmarks that appeared to be both easily identifiable and repeatable prior to statistical consideration. I surveyed a sample of 50 images from my image set and recorded landmarks that: (1) were present on all images, (2) were circumscribed by easily identifiable tissue interfaces, (3) were associated with identifiable anatomical features of the petrous part of the temporal bone, and (4)

appeared, in their entirety either on a single slice, or could be located in reliable association with another landmark (e.g. the anterior border of the petrous triangle at the level of the semicircular canals). This resulted in the collection of coordinate data for 36 landmarks per individual. These landmarks broadly represent the smallest dimensions of the middle and inner ears, and the largest dimensions of the contour of the petrous part of the temporal bone as a whole. The definitions and acronyms for the original 36 landmarks are listed in Table 5.1.

The Euclidean distances between each of the 36 landmark points were calculated in millimeters using the Excel software package (Microsoft 2003). This process resulted in the calculation of 640 measurements. The complete list of measurements is presented in Appendix I. These measurements are the data on which the rest of this research is based.

TABLE 5.1. Landmark locations and labels

Location	Label	Definition
Junction between the lateral and superior semicircular canals	LSC	Center point of the ampulla located at the junction of the lateral and superior semicircular canals (seen as a distinct circular feature)
Medial limit posterior semicircular canal	MPSC	Center point of the ampulla located at the medial-most extension of the posterior semicircular canal (appears as a distinct circular feature)
Lateral limit posterior semicircular canal	LPSC	The lateral most point along the curvature of the posterior semicircular canal (appears as a distinct circular feature)
Center of lateral semicircular canal	CLSC	The point at the center of the semicircular canal when the entire cross section of the canal is visible
Center of vestibule	VBLE	Center point of the vestibule as seen at the level of the semicircular canals
Center of cochlea	COCH	Center point of the cochlea 1 slice below the level of the semicircular canals
Center of middle ear	MID	Center point of the middle ear cavity at the level of the semicircular canals
Stylomastoid foramen	STYM	Center point of the stylomastoid foramen
Center of carotid canal	CARO	Center point of the supero-inferiorly oriented portion of the carotid canal where its entire circumference is visible
Lateral limit of jugular canal	JUG	Lateral most extension of the jugular canal where the carotid canal is also visible
Center of foramen ovale	OVAL	Center point of foramen ovale
Center of foramen spinosum	SPIN	Center point of foramen spinosum
Ant-lat extension of sigmoid sinus	SIG	Lateral most extension of sigmoid sinus where the posterior wall of the petrous extends medailly to the petrous apex
Auriculare	AUR	The point on the lateral aspect of the root of the zygomatic process at its deepest incurvature.
Basion	BAS	The point of intersection between the anterior margin of the foramen magnum and the median sagittal plane
Anterior limit of middle ear	AIE	Anterior-most point of the inner ear cavity at the level of the cochlea
Posterior limit of middle ear	PIE	Posterior-most point of the inner ear cavity at the level of the cochlea
Anterior border of EAM	AEAM	Point of intersection between the bony and cartilaginous parts of the external auditory meatus parts on the anterior wall where the entire length of the meatus is visible
Posterior border of EAM	PEAM	Point of intersection between the bony and cartilaginous parts of the external auditory meatus on the posterior wall where the entire length of the meatus is visible
Anterior border at IAC	APIAC	Point on the anterior wall of the petrous portion along a sagittal plane drawn through the center of the internal auditory canal at the level of the internal auditory canals
Posterior border at IAC	PPIAC	Point on the posterior wall of the petrous portion along a sagittal plane drawn through the center of the internal auditory canal at the level of the internal auditory canals

Table 5.1 Continued

Location	Label	Definition
Anterior border at semicircular canals	APSEM	Point on the anterior wall of the petrous portion along a sagittal plane drawn through the MPSC at the level of the semicircular canals
Posterior border at semicircular canals	PPSEM	Point on the posterior wall of the petrous portion along a sagittal plane drawn through the MPSC at the level of the semicircular canals
Lateral limit of IAC	LIAC	Lateral-most extension of the internal auditory canal (at the oval window) where the entire length of the canal is visible
Medial limit of IAC	MIAC	Point at the center of the posterior opening of the internal auditory canal where it intersects the posterior wall of the petrous portion where the entire length of the canal is visible
Petrous apex at IAC level	PAPE	Point at the apex of the petrous triangle
Lateral most point at level of IAC	LAT	Lateral-most point of the skull, between the sigmoid sinus posteriorly and the external auditory meatus anteriorly, at the level of the internal auditory canal
Anterior border of IAC	AIAC	Point on the anterior border of the internal auditory canal (IAC) along a sagittal plane drawn anteriorly from the intersection of the posterior wall of the IAC and the posterior wall of the petrous portion
Posterior border of IAC	PIAC	Point at the intersection of the posterior wall of the IAC and the posterior wall of the petrous portion
Vestibular aqueduct elevation	VAE	Point of elevation over the vestibular aqueduct on the posterior wall of the petrous portion
Spinous process	SPIPRO	Center point of spinous process
Mastoid antrum	MAN	Center point of the mastoid antrum at the level of the internal auditory canal
Sinus tympani	SINT	Point located on the center of the posterior wall of the sinus tympani at the level of the internal auditory canal
Scutum	SCU	Point located at the medial extension of the scutum at the level of the cochlea
Eustachian tube	EUST	Point at the center of the eustachian tube at the level of the temporo-mandibular joint
Pyramidal eminence	PYRE	Point located at the apex of the pyramidal eminence at the level of the cochlea

CHAPTER VI

REPEATABILITY AND DATA REDUCTION

This chapter provides a discussion of the statistical methods used to evaluate the precision and repeatability of the data collection process used in this research. It also presents the results of the precision and repeatability tests. Precision is defined as the mean absolute difference between repeat measurements of the same feature (Richtsmeier et al., 1995). Repeatability is a measure of the precision of measurements relative to the variation between two separate images (Richtsmeier et al., 1995), and is typically measured using a repeated measures analysis of variance. I investigated the precision with which the landmarks used in this research could be located on the same image multiple times and the repeatability of the measurements that extend between those landmarks on repeat images. I eliminated both the landmarks and measurements that showed unacceptable error rates by the process described in detail in the following paragraphs.

Following the evaluation of repeatability and demographic constraints, I employ two distinct models to further reduce my data set. The first model is based on a consideration of the developmental, structural, and functional characteristics of the petrous part of the temporal bone, and will be henceforth referred to as the biological model. The second model is based on the results of a principal components factor analysis of the measurement set without

consideration of the biological characteristics of the petrous part of the temporal bone. This model is henceforth referred to as the PCFA model. Detailed descriptions of both models follow, as does a detailed discussion of the similarities and differences that characterize the measurement sets selected according to them.

LANDMARK PRECISION

I evaluated the precision of the placement of each of the original 36 landmarks using a blind repeatability study. To do this, I analyzed a single image set from each of ten individuals four separate times over the course of three months, and calculated the means and standard deviations for the x and y values collected during the four trials. With a few exceptions, the standard deviations are very low, indicating a high level of accuracy in overall repeated landmark placement. I eliminated all landmarks with standard deviations that exceeded 10% of the mean of either the x or y values. This was intended to minimize error in the subsequent calculation of the distances between them, particularly in the case of landmarks located in close proximity to one another. Using this method, I eliminated five landmarks and retained 31 landmarks for use in the remainder of the analysis. Table 6.1 contains the means and standard deviations for each of the original landmarks.

TABLE 6.1. Means and standard deviations for each of the 36 original landmarks

Landmark	Mean		Standard Deviation	
	x	y	x	y
LSC	360.476	269.642	0.0733	0.0663
MPSC	353.277	264.132	0.0821	0.0872
LPSC	367.531	335.582	0.0097	0.0640
CLSC	377.468	294.324	0.0874	0.1405
VBLE	357.688	318.507	0.9405	1.0214
COCH	361.202	261.295	0.7451	0.6631
MID	384.556	274.791	0.6331	0.7212
STYM	391.635	320.588	0.0874	0.0797
CARO	353.023	270.275	1.0522	1.3031
JUG	372.973	289.626	1.2217	0.9971
OVAL	336.934	230.282	0.8080	0.6234
SPIN	353.023	243.828	0.0604	0.0457
SIG	414.126	339.924	1.3321	1.4251
AUR	421.882	274.749	1.2013	1.0388
BAS	275.797	281.241	1.0152	1.9191
AIE	378.121	266.404	0.0971	0.0663
PIE	379.408	290.916	0.0631	0.0977
AEAM	398.071	268.341	0.9104	0.8421
PEAM	399.358	283.821	0.8405	0.6045
APIAC	351.617	265.336	1.3328	1.4751
PPIAC	351.617	305.476	1.6756	1.2391
APSEM	379.408	320.588	1.3371	1.9121
PPSEM	377.477	262.534	0.9105	1.5942
LIAC	366.537	283.821	0.0997	0.3541
MIAC	332.429	285.756	1.6632	1.9122
PAPE	294.461	236.732	1.6321	1.3573
LAT	432.823	316.718	1.9645	1.6555
AIAC	340.152	277.317	0.9981	0.7541
PIAC	340.795	296.722	0.3544	0.5691
VAE	344.013	303.172	0.4557	0.3125
MAN	422.054	306.405	*8.0454*	*11.2220*
SINT	334.355	294.321	*6.9341*	*8.0045*
SCU	320.397	298.330	*5.0312*	*4.9282*
EUST	304.521	281.441	*5.033*	*7.811*
PYRE	383.012	288.301	*6.997*	*6.904*

MEASUREMENT REPEATABILITY

It is critical to demonstrate the intra-observer repeatability of measurement data for the effective usage of any anthropometric data (Jamison and Zegura, 1974; Gordon and Bradtmiller, 1992). In the present research it was important to evaluate the repeatability of the distance measures between the landmarks since these are the data that were actually analyzed. The pairwise calculation of the distances between each of the 30 landmarks produced 465 measurements.

There are various sources of error in anthropometric measurement, and the terminology used to describe them is not standardized (Cameron, 1986; Ulijaszek and Kerr, 1999). However, Ulijaszek and Kerr (1999) note that the influence of these various types of error can be divided into two categories: (1) error associated with inconsistency in repeated measures of the same value, which henceforth refer to as *reliability*, following Habicht et al. (1979), and (2) error associated with a departure of measurements from the actual value of the dimension, which I henceforth refer to as *inaccuracy,* following Heymsfield et al. (1984). I examine the extent to which both reliability and accuracy influence the repeatability of the present data set.

MEASUREMENT RELIABILITY

Mueller and Martorell (1988) suggested that there are two specific indicators that, in combination, yield the most valuable information regarding the reliability of anthropometric measurements, and that are also useful to evaluate the relative influence of biological variation and measurement error on repeatability. These are the technical error of measurement (TEM) and the reliability coefficient, both of which are described in detail in the following paragraphs.

TEM is very similar to the standard deviation of repeated measurement, and is calculated by entering the repeat measurement of the same subject by the same observer, as well as the difference in measurement between them, into an appropriate equation. The equation used in this research is appropriate for the calculation of the intra-observer TEM for a single measurement:

$$\mathrm{TEM} = \sqrt{(\Sigma D^2)/2N},$$

where D is the difference between measurements and N is the number of individuals measured. Similar methodologies have been used to evaluate the validity of measurement data collected from CT imagery in the clinical setting (Hildebolt et al., 1990; Cavalcanti et al., 2004). The resultant TEM measurement is in the same units as the anthropometric data entered into the equation.

Independently, the TEM results are difficult to interpret, but are critical to the subsequent calculation of measurement reliability.

To evaluate the reliability of each of the measurements based on the TEM values, I generated reliability coefficients. These coefficients facilitate comparison of the relative influence of measurement error and biological variability by revealing the proportion of the variation in a particular measurement that is free from error (Jamison and Ward, 1993; Meunier and Yin, 2000). I calculated the reliability coefficients by using Microsoft Excel software according to the following equation:

$$R = 1 - \left(\frac{r^2}{s^2} \right)$$

where r is the TEM, and s is the sample standard deviation. The resultant reliability value represents a direct measure of the proportion of variance that results from error in repeated measurement. The value will be high if the measurement error is small relative to the standard deviation of the sample. Thus, the higher the reliability coefficient, the more reliable the measurement.

The results of these analyses showed high reliability and low technical error in measurement for all of the 465 distances, an indication that little error is associated with the repeated analysis of the same image, meaning that image and biological variation are well controlled. This might have been presumed since I excluded the non-repeatable landmarks on which the distance measures

are based before calculating the estimates of reliability and precision. The mean reliability coefficient for the entire measurement set is .97, meaning that 97% of the overall variation in the sample is between groups rather than within them. The relationship between the TEM and reliability coefficients is displayed in Appendix II for each of the measurements.

Measurement accuracy

Mueller and Martorell (1988) define accuracy as the degree to which a measurement value reflects the "true" value of a morphological dimension. Inaccuracy results from systematic bias associated with instrument error or biased technique. It is important to establish the extent of inaccuracy in cases in which evidence collected using different equipment or by different users is compared. Since I used the same technique and the same equipment to collect my entire data set, any systematic bias in accuracy should be consistent throughout the sample, and the statistics used to identify inaccuracy of this type should not detect significant error.

Repeatability of repeat measurements

I used repeated measures analyses of variance (ANOVA) to evaluate the hypothesis that a decreased level of repeatability of would be associated with the collection of measurements from repeat images, and I used Pearson's R correlations to provide information regarding the strength of the associations between repeat measurements. Repeated measures ANOVA is appropriate for

use when the same characteristic is measured on each sample member on repeated occasions. Repeated measures ANOVA were performed on the measurements using the Statistica software package to extract the intra-group correlation coefficients as a measure of the relative amounts of inter and intra-group variability that characterized the measurement data collected from repeat images. Presumably, significantly more variation in each measurement would exist between individuals within a single trial than between measurements taken on a single individual measured during different trials. Only measurements with an intra-group correlation coefficient of .05 or less were included, meaning that at least 95% of the variation that characterizes a particular measurement is within rather than between groups. The results of the repeated measures ANOVA support the hypothesis that lower repeatability would be associated with repeated measurement from repeat images than with repeated measurement from the same image. The intra-group correlation coefficient exceeded .05 for 383 measurements. These measurements were excluded from the remainder of the analysis to maximize the overall repeatability of measurement set used in the method. A total of 82 measurements were retained for further analysis. The Pearsons's R correlation for each of these 82 measurements was very high. Table 6.2 displays the remaining 82 measurements as well as both the intra-group correlation coefficients and Pearsons R correlations associated with them.

TABLE 6.2. The 82 measurements and associated intra-group correlation coefficients.

Measurement	Intra-group correlation coefficient	Pearson's R	Measurement	Intra-group correlation coefficient	Pearson's R
MPSC-AIAC	0.0023	0.9841	MPSC-PAPE	0.0074	0.9971
STYM-CARO	0.0087	0.9749	LPSC-VBLE	0.0067	0.9877
STYM-MIAC	0.0097	0.9713	CLSC-COCH	0.0141	0.9881
MPSC-PIE	0.0076	0.9425	CLSC-STYM	0.0016	0.9987
LPSC-MIAC	0.0250	0.9621	VBLE-AIAC	0.0271	0.9863
COCH-SPIPRO	0.0347	0.9531	VBLE-PIAC	0.0068	0.9971
SIG-LAT	0.0097	0.9745	VBLE-AIE	0.0074	0.9799
AUR-LAT	0.0057	0.9829	VBLE-PIE	0.0014	0.9887
AUR-APIAC	0.0145	0.9901	VBLE-SPIPRO	0.0157	0.9931
PIAC-PAPE	0.0098	0.9903	COCH-MID	0.0047	0.9912
APIAC-PAPE	0.0240	0.9721	COCH-STYM	0.0015	0.9911
PPIAC-LAT	0.0134	0.9699	COCH-VAE	0.0067	0.9876
SIG-PIAC	0.0257	0.9703	MID-VAE	0.0157	0.9871
MPSC-LAT	0.0075	0.9874	MID-AIAC	0.0348	0.9931
LPSC-LAT	0.0047	0.9981	MID-PIAC	0.0154	0.9841
LSC-LAT	0.0145	0.9781	MID-AIE	0.0025	0.9911
CARO-AUR	0.0147	0.9831	MID-PIE	0.0019	0.9873
CARO-APIAC	0.0199	0.9877	MID-MIAC	0.0046	0.9911
CARO-MIAC	0.0039	0.9721	MID-PAPE	0.0056	0.9903
CARO-PAPE	0.0064	0.9837	MID-LAT	0.0063	0.9821
CARO-LAT	0.0084	0.9674	MID-SPIPRO	0.0017	0.9891
AIE-PPIAC	0.0068	0.9788	STYL-SIG	0.0094	0.9967
AIE-APSEM	0.0047	0.9634	STYL-AUR	0.0099	0.9852
AIE-PPSEM	0.0191	0.9891	STYL-VAE	0.0074	0.9843
AIE-PAPE	0.0236	0.9714	STYL-AIAC	0.0076	0.9984
AIE-LAT	0.0247	0.9872	STYL-PIAC	0.0016	0.9831
LAT-SPIPRO	0.0096	0.9987	CARO-VAE	0.0031	0.9887
CLSC-VAE	0.0087	0.9879	SIG-LIAC	0.0091	0.9981
SIG-APIAC	0.0301	0.9987	SIG-MIAC	0.0033	0.9911
APSEM-PPSEM	0.0091	0.9912	SIG-PAPE	0.0091	0.9931
PAPE-LAT	0.0071	0.9936	AUR-AIAC	0.0097	0.9789
LSC COCH	0.0091	0.9945	AUR-PIAC	0.0064	0.9917
LSC-AIE	0.0087	0.9970	AUR-AIE	0.0047	0.9897
LSC-LIAC	0.0071	0.9845	AUR-PIE	0.0079	0.9863
LSC-MIAC	0.0157	0.9798	AIAC-PIAC	0.0074	0.9971
LSC-PAPE	0.0168	0.9712	AIAC-PIE	0.0037	0.9731
MPSC-STYM	0.0264	0.9826	PIAC-LIAC	0.0066	0.9910
MPSC-CARO	0.0083	0.9865	PIAC-MIAC	0.0037	0.9908

Table 6.2 Continued

Measurement	Intra-group correlation coefficient	Pearson's R	Measurement	Intra-group correlation coefficient	Pearson's R
MPSC-JUG	0.0079	0.9911	PIAC-LAT	0.0129	0.9971
MPSC-SPIPRO	0.0093	0.9787	PIAC-SPIPRO	0.0311	0.9914
MPSC-AIE	0.0081	0.9981			0.9713

VARIATION RELATED TO SEX, AGE AND LENGTH OF TIME BETWEEN SCANS

The individual and combined influences of age, sex and variation in the length of time between repeat scans are important variables to study with regard to variability in petrous portion anatomy. This section presents the methods and results of the analyses that I use to evaluate whether these demographic factors influence the morphology of the petrous portion of the temporal bone. I discuss the procedures used to test the implications of these factors on the method developed in Chapter VII.

I used multivariate general linear models (GLM) to evaluate the potential influence of age, sex, and duration, as well as potential higher order interactions between the three, on each of the petrous portion measurements used in this research. These tests compute independent analyses of variance with regard to each of the factors, sex, age and duration between scans, and between every combination of these factors (sex by age, sex by duration, duration by age, and sex by duration by age). The GLM results are in Appendix III. Summary results are discussed in the following paragraphs.

Age variation

Several authors have suggested age-related growth in various dimensions of the adult skull (Zuckerman, 1955; Israel, 1973, 1977; Ruff, 1980). However, this change seems to be limited to the larger dimensions of the cranial vault (Zuckerman, 1955). The unique ossification characteristics of the petrous portion of the temporal bone presumably spare it from this type of adult age-related change. The petrous portion ossifies endochondrally, but unlike other endochondral bones, the "first formed bone is not replaced by Haversion bone, but keeps its primitive, relatively avascular structure" (Scheuer and Black, 2000: 75). Once ossified, this bone is retained throughout life, and does not undergo subsequent remodeling (Scheuer and Black, 2000).

Thus barring pathological activity, there is little reason to expect age related changes in the dimensions of the adult petrous portion of the temporal bone. Few of the bony dimensions of the petrous portion are susceptible to ontogenetic influence (Anson and Donaldson, 1972). While hearing loss resulting from aging (presbycusis) is common, the process typically only affects the soft tissues of the ear apparatus (Belal, 1975). Belal (1975) demonstrated that the pathological and physiological varieties of age-related hearing loss effect different parts of the hearing apparatus, but that in both cases, the affected tissues are associated with either nerve tissue or the various membranes, ligaments, and muscles that contribute to the hearing process. The orientation and interaction of the ear ossicles can be influenced by these

processes as well. However, the ossicles do not provide any of the landmarks used in this research, both because of their elevated susceptibility to pathological change relative to the surrounding temporal bone, and their tendency to move during the decomposition process.

Nevertheless, the high prevalence of age-related soft-tissue changes in the ear necessitates consideration of potential associated changes in the dimensions of the surrounding bone. Age influence was investigated by comparing the mean values for each of the measurements between the groups. I subdivided the sample into age categories, 18-35, 36-50, and >50 years. These categories represent a compromise between age milestones related to hearing loss, and sample size. Age-related hearing loss typically begins at around age 50 (Belal, 1975), thus it is important to evaluate the dimensions of individuals over fifty relative to the younger individuals in the sample. The 18-35 and 36-50 year categories represent early adulthood and middle adulthood respectively, as well as categories within which sufficient numbers of individuals fit.

The general linear model showed no significant differences in the particular dimensions of the petrous portion of the temporal bone recorded in this analysis. Table 6.3 displays the sample sizes in each of the age groups, Appendix III displays the p values for each measurement.

TABLE 6.3. Sample sizes in each of the age groups.

Age group	Sample size
18-35 years	42
36-50 years	38
Greater than 50 years	48

Variation related to duration of time between images

Perhaps more important than age is the potential influence of the variable that measures the duration of time between first and second scans on the dimensions of the petrous part of the temporal bone. To investigate this variation, I subdivided the sample into four categories based on the length of time between their scans. The categories were: (1) Less than 3 months, (2) 3 months to 1 year, (3) 1 to 3 years, and (4) greater than 3 years. These categories were selected largely based on the available sample sizes; unfortunately, very few of the individuals in the sample had sets of images taken more than 5 years apart. The mean differences between the repeat measurement values were calculated for each of the categories listed above and compared using the GLM procedure. Barring significant pathological or ontogenetic change, the dimensions should not change significantly, especially since the measurements were selected because they were not associated with the segments of the petrous part of the temporal bone that are known to be most susceptible to this type of change. For example, with the possible exception of LAT (the lateral-most projection of the petrous temporal bone on the ectocranial surface), the landmarks used in this analysis are not associated with areas of

muscular attachment that have the propensity to change with muscle activity levels, etc. The GLM procedure uncovered no significant variation in the repeatability of measurement related to the variation in the amount of time between scans. Table 6.4 displays the size of the samples for each of the duration groups. The *p* values for each measurement are also presented in Appendix III.

TABLE 6.4. Sample sizes of each of the duration groups.

Duration group	Sample size
Less than 3 months	35
3months to year	40
1 to 3 years	26
Greater than 3 years	27

Sex variation

Numerous authors have demonstrated that some of the dimensions of the cranial base (Holland, 1986; Wescott and Moore-Jansen, 2001), and specifically the petrous portion of the temporal bone (Kalmey and Rathbun, 1996; Graw et al., 1999; Noren et al., 2005) vary significantly by sex. There is no record of research regarding sex-related variation specific to the measurements used in this research.

Sex-related variation in the dimensions of the petrous part of the temporal bone was analyzed: (1) to determine the extent of sexual dimorphism in the petrous portion, and (2) to determine the influence of this dimorphism on the

accuracy of the method. As with age and duration of time between scans, I used ANOVA, embedded within the GLM procedures described above to investigate sexual dimorphism in the dimensions of the petrous part of the temporal bone. A detailed presentation of the GLM results is located in Appendix III. In summary, 25 measurements show significant sex-related variation. Table 6.5 contains these 25 measurements and their associated p values.

Most of the measurements that show significant dimorphism are associated with the medio-lateral and anterior posterior dimensions of the petrous bone. A few measurements are associated with the smaller dimensions of the ear apparatus. Interestingly, these three measurements (PIAC-LIAC, PIAC-MIAC, and AIAC-PIAC) are all associated with the dimensions of the internal auditory canal and its relationship to the surrounding bone. As mentioned in Chapter IV, this is a region of the petrous portion that has received considerable attention in the literature with regard to sexual dimorphism (Kalmey and Rathbun, 1996; Noren et al., 2005).

The significance of sex-related variation in these measurements of the petrous portion necessitates the quantification of the extent to which this relationship influences the accuracy of the identification method proposed in this research. These analyses are discussed later in relation to the success of the nearest neighbor analyses.

TABLE 6.5. Measurements that display significance sex variation and their associated p values

Measurement	p value
SIG-LAT	.0019
AUR-APIAC	.0034
PIAC-PAPE	.0029
APIAC-PAPE	.0013
PPIAC-LAT	.0034
MPSC-LAT	.0017
LSC-LAT	.0023
CARO-APIAC	.0078
CARO-LAT	.0315
AIE-PPIAC	.0127
AIE-APSEM	.0067
AIE-PPSEM	.0214
AIE-PAPE	.0171
AIE-LAT	.0097
APSEM-PPSEM	.0031
PAPE-LAT	.0067
LSC-PAPE	.0163
MPSC-PAPE	.0240
MID-PAPE	.0087
MID-LAT	.0031
PIAC-LAT	.0214
SIG-LIAC	.0181
PIAC-LIAC	.0312
PIAC-MIAC	.0211
AIAC-PIAC	.0097

Covariation

Since covariate relationships in the dimensions of the cranial base are known to exist between sex and age (Moore-Jansen and Jantz, 1989; Wescott, 1996; Wescott and Moore-Jansen, 2001), secular change and sex (Moore-Jansen, 1989), and secular change and age (Jantz and Jantz, 2000), it is necessary to investigate these relationships in the current research. The GLM procedure also provides information regarding the extent of interaction between these demographic constraints. These results are also presented in Appendix III. The GLM results show no significant interaction between any of the three factors, probably since neither age nor duration had significant effects on their own.

DATA REDUCTION

Eighty-two measurements remain after the repeatability study. However, in spite of their repeatability, these particular measurements do not necessarily represent the most efficient means to quantify the morphology of the petrous portion of the temporal bone. Numerous authors have demonstrated that the dimensions of the cranium often vary in conjunction with each other, and thus do not necessarily represent independent morphological characteristics (Cheverud, 1982, 1995). This is even the case between segments of the cranium that represent developmentally or structurally distinct ranges of variation (Enlow, 1990; Enlow and Hans, 1996). For the current research, this means that some

of the 82 repeatable measurements may be redundant in terms of the dimensions of the petrous portion they represent and thus add little to the analysis. It also means that extracting a measurement set based on developmental and structural criteria alone may not reflect independent traits either (Athreya and Glantz, 2003).

The goal of the data reduction process was to determine the most effective method of limiting the measurement set so as to maximize the efficiency of the technique while: (1) incorporating the important variability in the bone, and (2) avoiding redundant measurement of the same variation. There clearly are distinct developmental segments of the petrous portion of the temporal bone, and it is important that the dimensions of each be incorporated into the analysis, but it is also true that an unbiased statistical technique may elucidate both important relationships and redundant measures that cannot be predicted based on intuition alone.

I employed two separate models to identify which of the remaining dimensions of the petrous part of the temporal bone represented meaningful, individually variable, non-redundant variation. I then evaluated the implications of each model on the resultant method. The first approach involves selecting measurements using a preconceived model based on biological and methodological constraints. The emphasis of this approach is that the resultant set should encompass the various developmental regions of the petrous portion, while avoiding measurements that span regions that are most susceptible to

taphonomic destruction and ontogenetic change. Thus, the first approach involves a judgment based on careful consideration of the developmental variability of the petrous portion of the temporal bone, and the efficiency with which this method could be used in the forensic setting.

The second approach involves the application of statistical techniques of data reduction without regard to an intuitively-conceived construct. This process involves the application of principal components factor analysis to the entire measurement data set, rather than one that had been previously reduced based on a biological model. The combination of measurements that I retain following this analysis is based on their loadings on the principal factors. This is intended to eliminate redundant measurement of the same variation in the petrous part of the temporal bone, and to maximize the efficiency of the remaining measurement set in accounting for its total variation by limiting the data set to a smaller, yet equally representative set of uncorrelated factors. Each of these steps is described in detail in the following paragraphs.

Biological model

Development of the measurement set to be included in the biological model was based on consideration of the relationship of the remaining repeatable measurements with the development and overall shape of the petrous bone. From a biological perspective it is important to select a suite of measurements that adequately encompass each of the various distinct developmental regions of the petrous portion of the temporal bone, and to tie

them together by incorporating measurements that extend beyond the boundaries of the each of the regions. The configuration of the middle and inner ear is largely determined at birth and thus represents a separate developmental unit from the remainder of the petrous part of temporal bone, which grows in various directions around the ear apparatus into adulthood (Gulya and Schuknecht, 1994; Scheuer and Black, 2000). In order to encompass this variability effectively, the measurements can be grouped according to their membership in one of three anatomical categories: (1) dimensions of the inner and/or middle ear, (2) dimensions of the outer (antero-posterior and medio-lateral) contour of the petrous portion of the temporal bone, and (3) measurements that link categories (1) and (2), i.e. the middle/inner ear and the contour of the bone. The logic behind this process is that it would result in a measurement set that is most representative of the overall dimensions of the petrous portion of the temporal bone, and most effectively encompassed the ontogenetic alterations that shape the bone as it grows. A subset of 30 measurements resulted from this process. Those that were eliminated were either those which are most difficult to define, have the lowest repeatability, or represent redundant measurement of the same dimensions of the petrous portion. The 30 measurements included in the biological model are listed in Table 6.6 and are illustrated in Figures 6.2-6.4.

TABLE 6.6. Measurements selected using the biological model

Middle ear	Contour	Middle ear to contour
MPSC-AIAC	SIG-LAT	MPSC-LAT
STYM-CARO	AUR-LAT	LPSC-LAT
STYM-MIAC	AUR-APIAC	LSC-LAT
MPSC-PIE	PIAC-PAPE	CARO-AUR
LPSC-MIAC	APIAC-PAPE	CARO-APIAC
COCH-SPIPRO	PPIAC-LAT	CARO-MIAC
	SIG-PIAC	CARO-PAPE
	PAPE-LAT	CARO-LAT
		AIE-PPIAC
		AIE-APSEM
		AIE-PPSEM
		AIE-LAT
		CLSC-VAE
		LAT-SPIPRO
		SIG-APIAC
		AIE-PAPE

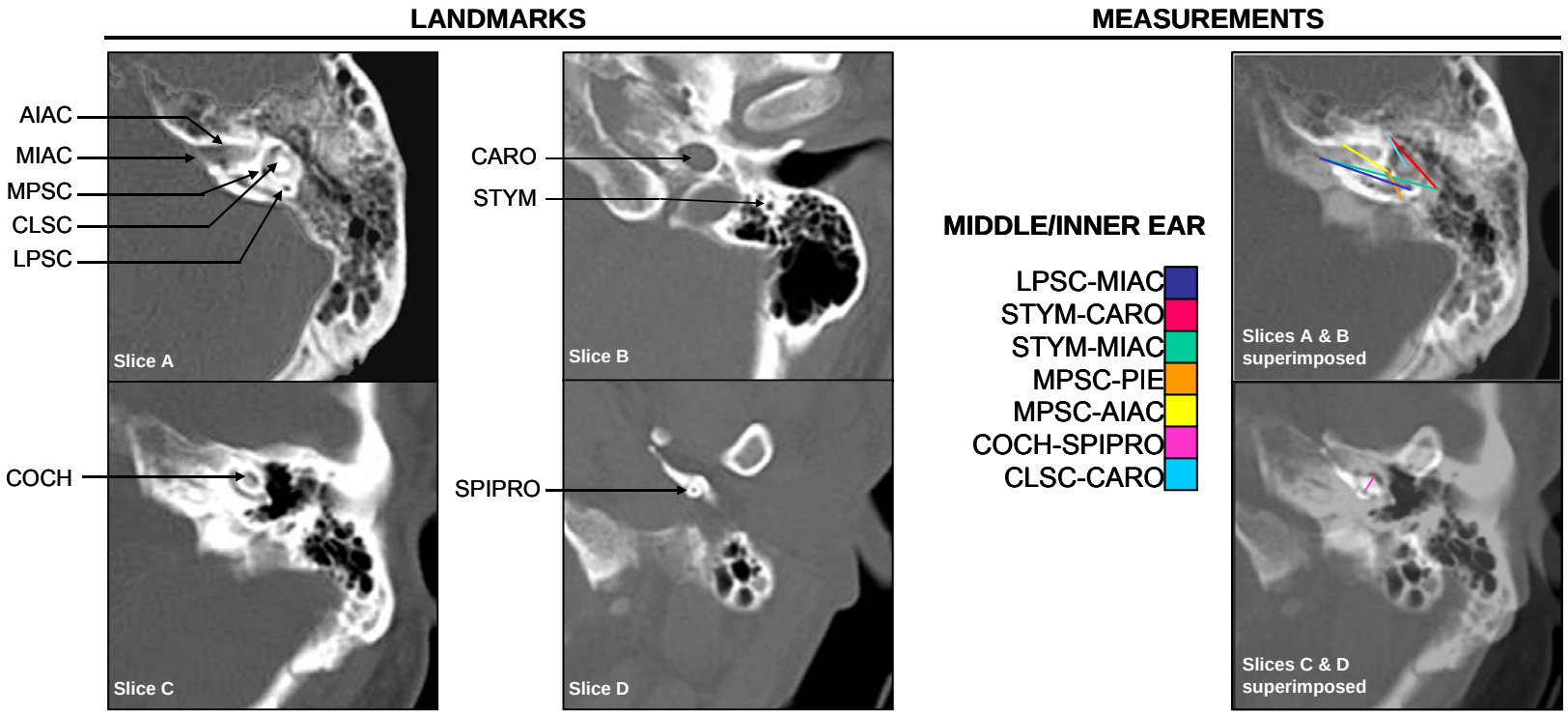

Figure 6.2. *The first two columns illustrate the landmark locations in the inner and middle ear segments of the petrous part of the temporal bone used in this research. The third column illustrates the measurements between the landmarks in the inner and middle ear segments. The measurements are color coded according to the legend located between columns 2 and 3.*

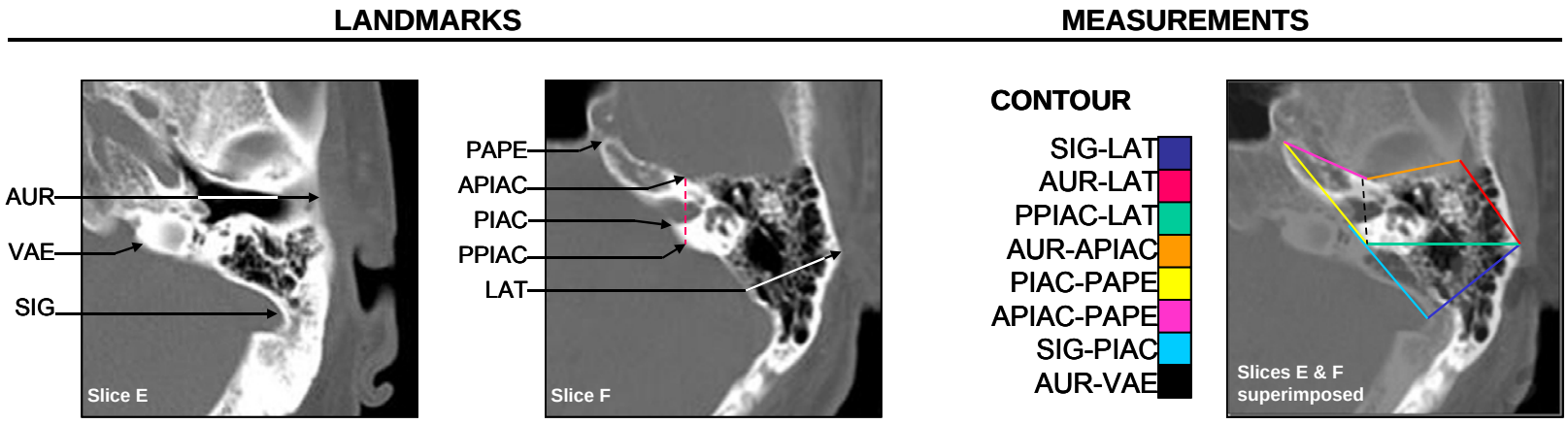

Figure 6.3. *The first two images (labeled slices E&F) illustrate the locations of the landmarks around the contour of the petrous part of the temporal bone. The third image illustrates the measurements between the landmarks around the contour of the petrous part of the temporal bone. The measurements are color coded according to the legend located between the second and third images.*

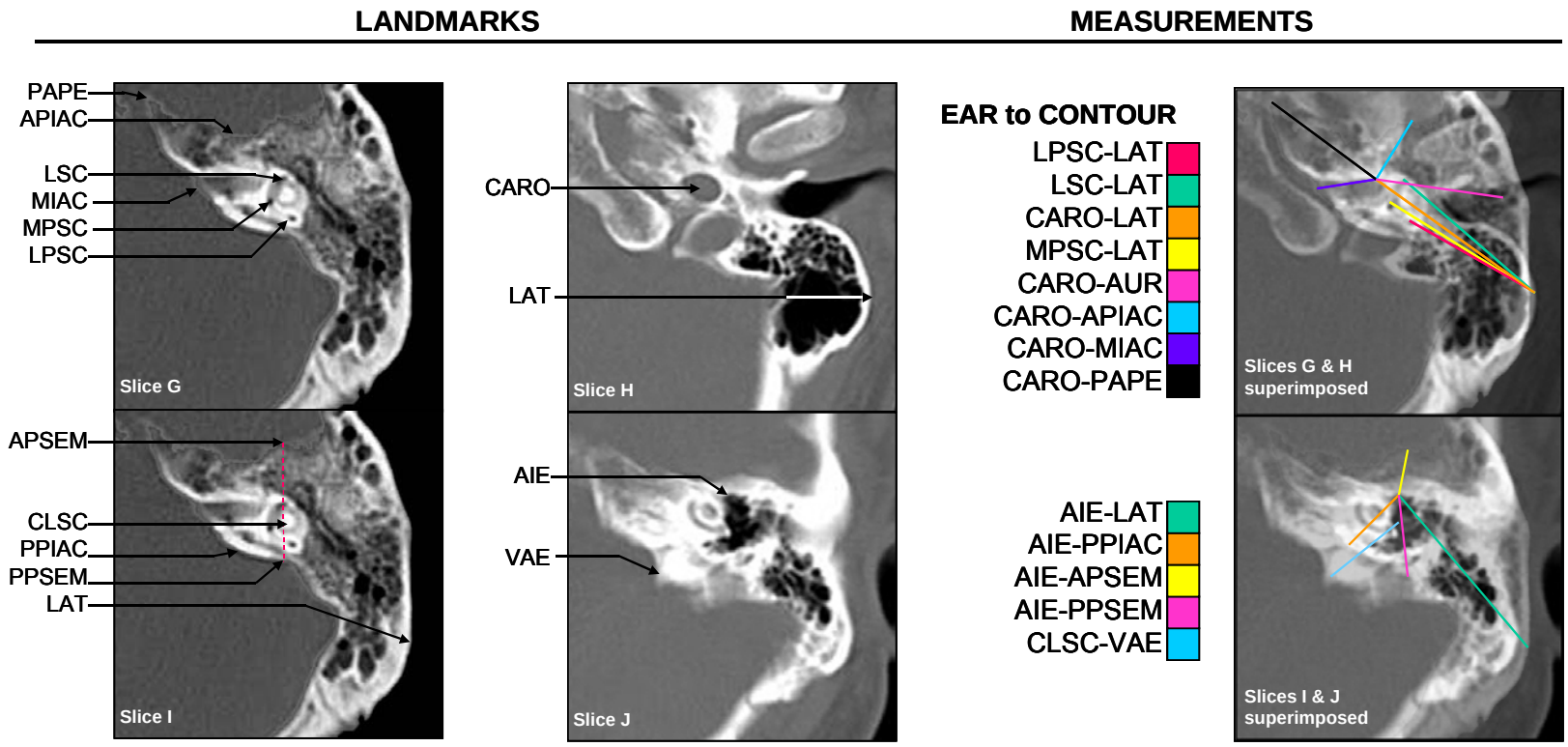

Figure 6.4. *The first two columns illustrate the remaining landmark locations in both the inner and middle ear, and the contour segments of the petrous part of the temporal bone. The third column illustrates the measurements between the measurements that extend between the landmarks of the inner and middle ear, and the contour of the petrous part of the temporal bone. The measurements are color coded according to the legend located between columns 2 and 3.*

Principal Components Factor Analysis Model

The second method of data reduction involves the use of principal components factor analysis (PCFA). PCFA is suited to research in which the investigator has no reason, biological or otherwise, to suspect that any one, or combination of variables is more diagnostic than any other, meaning that the analyst need not have a theoretical reason to expect *a priori* relationships within his or her data (Blackith and Reyment, 1971). In analyses such as these, PCFA acts to reduce a large number of variables according to a smaller set of factors that each represents a portion of the total variation of the data into the variance distance between them. The factors themselves are linear representations of combinations of observable variates, and can be used as variables themselves. In this research, I do not use the factors as variables. Instead, I use the output data to make inferences about the nature of the variation of the data (in this case the shape of the petrous temporal bone) through consideration of which variables load most heavily (either positively or negatively) along which factors, and which measurements combine along a particular factor.

Inclusion of all factors with associated eigenvalues of 0.4 or greater results in the extraction of 29 factors that account for nearly 95% of the cumulative variance in the sample. This particular cut-off allows me to generate a measurement set that approximates the biological model set and thus facilitates comparison of the two models. Table 6.7 shows the eigenvalues, percent of variance, and cumulative variance associated with the first 29 factors.

TABLE 6.7. Eigenvalues, percent of variance, and cumulative variance for first 29 factors.

	Initial Eigenvalues		
Factor	**Eigenvalue**	**% of Variance**	**Cumulative %**
1	9.915	12.091	12.091
2	8.251	10.062	22.153
3	7.076	8.629	30.782
4	6.231	7.598	38.380
5	5.231	6.379	44.759
6	4.424	5.395	50.155
7	4.394	5.358	55.513
8	3.280	4.000	59.513
9	2.805	3.420	62.934
10	2.723	3.321	66.254
11	2.271	2.770	69.024
12	2.148	2.620	71.644
13	2.051	2.502	74.145
14	1.926	2.349	76.495
15	1.658	2.022	78.517
16	1.494	1.823	80.339
17	1.416	1.726	82.065
18	1.264	1.541	83.607
19	1.191	1.452	85.059
20	1.041	1.270	86.329
21	1.008	1.229	87.558
22	0.931	1.135	88.693
23	0.864	1.054	89.747
24	0.813	0.991	90.738
25	0.742	0.904	91.643
26	0.685	0.835	92.478
27	0.634	0.774	93.252
28	0.603	0.736	93.987
29	0.480	0.586	94.573

Close inspection of the factor loadings for the first 29 components provides information regarding: (1) the morphological relationships between the

measurements that loaded on each component and (2) potential redundancy in the measurement set. Appendix IV displays the Varimax rotated factor matrix for the first 29 components. Seventy-seven measurements loaded heavily (>.6) on the first 29 components.

Morphological relationships

As expected, the measurements that load heavily on the first factor somewhat reflect the overall size of the petrous part of the temporal bone. For instance, PAPE-LAT is a measure of the maximum medio-lateral dimension of the petrous portion, and loads heavily on the first factor. The distance extending from APSEM to PPSEM represents the maximum anterior posterior dimension of the body of the petrous triangle at the level of the semicircular canals. Two measurements associate central components of the petrous part of the temporal bone to its boundaries. MID-PIAC extends from the center of the middle ear cavity, posteriorly to the intersection of the posterior wall of the IAC and the posterior wall of the petrous triangle, and STYL-SIG encompasses the distance between the stylomastoid foramen and the lateral-most extension of the sigmoid sinus. Various small dimensions of the middle and inner ear complexes extending from the vestibule also load highly on the first component. In combination, these measurements represent a detailed picture of the location of the vestibule in relation to the ear, internal auditory canal and spinous process.

The rest of the factors incorporate measurements that extend from singular central landmarks. For example, the measurements that load heavily

on the second factor are all extensions from the stylomastoid foramen to various landmarks located nearby. Based on the similarity of their loadings, most of the measurements on the second factor appear to be redundant measurements of the same dimensions. A similar pattern characterizes the third through thirteenth factors, representing variable dimensions around centralized landmarks. Some of these factors incorporate measurements that extend from landmarks that are located in the middle or inner ear complexes like the vestibule (VBLE), and the center point of the middle ear (MID), and others are located along the periphery of petrous part of the temporal bone like auriculare (AUR) and the sigmoid sinus (SIG). Collectively, the various factor loadings resemble a series of overlapping spoked wheels that in combination encompass a large portion of the morphology of the petrous part of the temporal bone. However, there is considerable redundancy in these measurements, and a much more efficient suite of measurements can be derived through careful elimination of multiple measures of the same variation.

Reduction of measurement set

Thirty-eight of the 77 measurements were excluded from further analysis because they: (1) represent redundant measurement of variation already accounted for by other measurements and (2) are associated with smaller loadings than other measurements that account for the same variation. However, the biological relationships between the measurements were considered during the exclusion process. I excluded measurements only on the

basis of statistical considerations. The 38 measurements that I eliminated using this process are listed in Table 6.8, as is the justification for the exclusion of each from the remainder of the analysis.

TABLE 6.8. Measurements excluded from analysis following PCFA.

	Measurement	PCFA Factor	Loading	Reason for Exclusion
1	VBLE-AIAC	1	0.932	redundant with LPSC-VBLE and harder to measure
2	VBLE-PIAC	1	0.917	redundant with LPSC-VBLE and harder to measure
3	VBLE-PIP	1	0.748	redundant with STYL-SIG and harder to measure
4	MID-PIAC	1	0.951	redundant with LPSC-VBLE and harder to measure
5	STYL-PIAC	2	0.673	low loading
6	COCH-STYM	2	0.934	redundant with STYL-CARO
7	CLSC-STYM	2	0.968	redundant with STYM-MIAC and harder to measure
8	MPSC-STYM	2	0.969	redundant with STYM-MIAC and harder to measure
9	STYM-VAE	2	0.952	redundant with STYM-MIAC and harder to measure
10	STYM-AIAC	2	0.977	redundant with STYM-MIAC and harder to measure
11	STYM-CARO	2	0.949	redundant with STYM-MIAC and has lower loading
12	VBLE-PIE	3	0.991	redundant with MPSC-PIE and harder to measure
13	MID-PIE	3	0.993	redundant with MPSC-PIE and harder to measure
14	AUR-PIE	3	0.992	redundant with MPSC-PIE and harder to measure
15	AIAC-PIE	3	0.993	redundant with MPSC-PIE and harder to measure
16	AIE-PIE	3	0.994	redundant with MPSC-PIE and harder to measure
17	AUR-PIAC	4	0.941	redundant with AUR-APIAC and does not incorporate AP dimension as well
18	AUR-PIE	4	0.941	redundant with AUR-APIAC and does not incorporate AP dimension as well
19	AUR-AIAC	4	0.963	redundant with AUR-APIAC and does not incorporate AP dimension as well
20	CARO-AUR	4	0.914	redundant with AUR-APIAC with lower loading
21	SIG-MIAC	5	0.918	redundant with SIG-LIAC and harder to measure
22	SIG-PIAC	5	0.922	Redundant with SIG-LIAC with lower loading
23	SIG-PAPE	5	0.671	low loading
24	SIG-APIAC	5	0.849	redundant with SIG-LIAC with lower loading
25	CLSC-COCH	6	0.955	redundant with LSC-COCH and harder to measure
26	COCH-VAE	6	0.745	redundant with COCH-MID and harder to measure
27	PIAC-LAT	7	0.875	redundant with PPIAC-LAT and harder to measure
28	AIE-LAT	7	0.828	redundant with PPIAC-LAT with lower loading
29	APIAC-PAPE	8	0.839	redundant with PIAC-PAPE

Table 6.8 Continued

	Measurement	PCFA Factor	Loading	Reason for Exclusion
30	CARO-PAPE	8	0.744	redundant with AIE-PAPE with lower loading
31	CARO-MIAC	9	0.859	redundant with MPSC-CARO and harder to measure
32	MPSC-CARO	9	0.802	redundant with CARO-VAE and measures same dimension
33	LPSC-LAT	10	0.686	redundant with MPSC-LAT with lower loading
34	MID-LAT	10	0.946	redundant with LSC-LAT and harder to measure
35	MID-SPIPRO	11	0.948	redundant with COCH-SPIPRO and harder to measure
36	MID-VAE	12	0.867	redundant with CLSC-VAE and harder to measure
37	MPSC-PAPE	13	0.882	redundant with LSC-PAPE
38	MID-AIAC	16	0.742	redundant with MPSC-AIAC and harder to measure

Excluding the 38 redundant measurements from the set of 77 that load highly on the 29 factors, leaves 39 measurements to be included in the rest of the analysis. This collection of measurements represents the PCFA model data set, and is similar in number to the set included in the biological model. The similarity in the number of measurements in the two models makes it unlikely that differences in their relative accuracy are the result of a difference in the number of variables. The PCFA model measurements, their loadings and factor numbers are listed in Table 6.9. The table also indicates whether or not each measurement is also among those selected for use in the biological model.

TABLE 6.9. Measurements selected using the PCFA model

	Measurement	PC Factor	Loading	In Biological model
1	MPSC-AIAC	16	0.899	Y
2	STYM-MIAC	2	0.977	Y
3	MPSC-PIE	3	0.993	Y
4	LPSC-MIAC	1	-0.665	Y
5	COCH-SPIPRO	11	0.899	Y

Table 6.9 Continued

	Measurement	PC Factor	Loading	In Biological model
6	SIG-LAT	20	0.876	Y
7	AUR-LAT	22	0.916	Y
8	AUR-APIAC	4	0.932	Y
9	PIAC-PAPE	8	0.841	Y
10	PPIAC-LAT	7	0.884	Y
11	MPSC-LAT	10	0.731	Y
12	LSC-LAT	10	0.946	Y
13	CARO-APIAC	17	-0.625	Y
14	CARO-LAT	7	0.692	Y
15	AIE-PPIAC	1	-0.658	Y
16	AIE-APSEM	28	0.919	Y
17	AIE-PPSEM	26	0.883	Y
18	CLSC-VAE	12	0.877	Y
19	AIE-PAPE	8	0.786	Y
20	PAPE-LAT	1	-0.936	Y
21	LSC-COCH	6	0.965	N
22	LSC-LIAC	24	0.913	N
23	LSC-PAPE	13	0.889	N
24	MPSC-JUG	29	0.873	N
25	MPSC-AIE	14	0.922	N
26	LPSC-VBLE	18	0.946	N
27	VBLE-AIE	1	0.970	N
28	COCH-MID	6	0.757	N
29	MID-AIE	15	0.940	N
30	MID-PAPE	23	0.844	N
31	STYL-SIG	1	0.809	N
32	STYL-AUR	2	0.861	N
33	CARO-VAE	9	0.932	N
34	SIG-LIAC	5	0.946	N
35	AIAC-PIAC	27	0.944	N
36	PIAC-LIAC	21	0.828	N
37	PIAC-MIAC	19	0.875	N
38	PIAC-SPIP	25	0.837	N
39	APSEM-PPSEM	1	-0.909	N

Twenty of the 39 measurements included in the PCFA model are also included in the measurement set used in the biological model. This means that 19 of the measurements selected using the PCFA model are not considered in the biological model and that 10 of the measurements used in the biological model are not incorporated into the PCFA model. However, there is considerable overlap of measurements between the two methods, suggesting that the measurements selected for use in the biological model may indeed statistically reflect meaningful dimensions of the petrous part of the temporal bone. In addition, 7 of the measurements that are excluded from the PCFA model (SIG-PIAC, STYM-CARO, AIE-LAT, LPSC-LAT, CARO-AUR, SIG-APIAC, and CARO-PAPE) were excluded as redundant measures because of their slightly lower loadings than certain measurements that are included in this model (SIG-LIAC, STYM-MIAC, PPIAC-LAT, MPSC-LAT, AUR-APIAC, SIG-LIAC, AIE-PAPE, respectively). However, considering the biological relationship of these measurements to the dimensions of the surrounding bone would result in the selection of measurements with lower loadings in favor of their more meaningful representation of petrous temporal bone morphology. In fact, if biological considerations had been included in the development of the PCFA model, 27 of the PCFA model measurements would be in common with the set selected for the biological model. However, since these relationships are statistically redundant, the difference in relative accuracy of the two models related to the juxtaposition of these few measurements is likely minimal.

The measurement sets selected using the biological and PCFA models are independently submitted to nearest neighbor analysis in the next chapter (Chapter VII) as a means to evaluate the relative accuracy of each in correctly matching CT images from the same individual. The results of this evaluation are also presented in Chapter VII.

CHAPTER VII

NEAREST NEIGHBOR COMPARISONS, LIKELIHOOD ESTIMATES, AND POSTERIOR PROBABILITIES

The distances in Euclidean space between the measurement values for repeat images taken from each individual and those between individuals were calculated for each of the measurements, first for the set of 30 measurements incorporated into the biological model and again for the 38 measurements that resulted from the PCFA model. This chapter presents: (1) the nearest neighbor analysis of the Euclidean distances used to evaluate each model, (2) summary results of the nearest neighbor analyses of both measurement sets, (3) summary statistics regarding the mean Euclidean distances between repeat and non-repeat images for both models, and (4) various measures of the probability of correct nearest neighbor matches including typicalities, likelihood estimates and posterior probabilities. Nearest neighbor analysis in this context refers simply to the association of values that are closest in numerical detail and differs from nearest neighbor analysis used in cluster analysis in that it does not involve the calculation of centroids.

There is little in the way of direct precedent for this method in the forensic anthropological literature. Christensen (2004) used perhaps the most relevant method to evaluate the identification potential of frontal sinus outlines as seen on anterior posterior radiographs of the head. She compared the Euclidean

distances between coefficients generated from Elliptical Fourier Analysis of the outline of individual frontal sinuses and found that the summed Euclidean distances between repeat images taken from the same individual were significantly smaller than those from different individuals (Christensen 2004). Jain and Chen (2004) developed a technique by which radiographic dental identifications can be standardized using nearest neighbor analysis. The process involves the "semi-automatic" extraction of tooth contour images, and the nearest neighbor comparison of coefficients based on those contours (Jain and Chen, 2004:1519).

In fact, there is a large amount of research using various nearest neighbor algorithms in the biometrics and pattern recognition arenas (Wayman et al. 2005). Nearest neighbor methodologies are particularly prevalent in the development of identification techniques based on photographic representations of human faces (Wechslet et al., 1998; Weng and Swets, 1999). These techniques generally compare the Euclidean distances between coefficients generated from a collection of points on the human face to facilitate nearest neighbor matches (Weng and Swets 1999). Recent techniques have also been developed to make individual identifications using nearest neighbor comparisons of coefficients generated from minutiae in the human iris (Ma et al., 2003).

NEAREST NEIGHBOR ANALYSIS

I used nearest neighbor analysis to make associations between individuals in the sample. I calculated the Euclidean (data space) distances

between pairs of measurement sets by first summing the values of the 30 or 38 measurements for each individual, and then making nearest neighbor comparisons of these values (the sums of measurements) between each individual, and every other individual in the sample. However, I only compare images in the first set to images in the second set. In other words, if this was a forensic data set composed of ante- and postmortem images, comparisons would only be made between an image in the postmortem collection and the images in the antemortem collection, and no comparisons would be made between any two images in the postmortem collection. I made the comparisons using a nearest neighbor program written using the FOXPRO software. The program associates individuals whose summed measurement values are closest in Euclidean distance. I used the nearest neighbor algorithm on the measurement sets that result from each of the data reduction models.

I made nearest neighbor associations using: (1) the set of thirty measurements that are included in the biological model, and (2) the set of 38 measurements that are included in the PCFA.

Nearest neighbor accuracy

Summary statistics regarding the numbers of correct and incorrect matches using the nearest neighbor algorithm are presented for the complete sample and independently for males and females in Table 7.1. Overall accuracy of the biological model is 97% (112 of 115 comparisons resulted in correct matches), versus 95% for the PCFA model (109 of 115 matches are correct).

TABLE 7.1. Number of incorrect nearest neighbor association using both models

	Biological model		PCFA model	
	n	**Number of misses**	**n**	**Number of misses**
Females	65	0	65	0
Males	50	3	50	5
Combined	115	3	115	5

SUMMARY STATISTICS

Summary statistics regarding the Euclidean distances between the summed measurements of repeat images (two images from the same individual) are presented in Tables 7.2 and 7.3 for the biological and PCFA models, respectively, as are the summary statistics for the Euclidean distances between the summed measurements of different individuals. For the sake of clarity, the two images taken from a single individual at different times are henceforth referred to as “repeats.” and comparisons between repeats are referred to as “repeat comparisons.” “Non-repeats” refer to any two images that are not from the same individual. Thus a “non-repeat comparison” refers to a comparison between the image of one individual and the image of any other individual. There were 115 comparisons between repeat images and 13,110 between non-repeat images (distances between an individual and every other individual).

TABLE 7.2. Summary of Distances between Repeats and Between Different Individuals (Biological Model)

Repeats		**Different Individuals**	
Statistic	**Value**	**Statistic**	**Value**
N of comparisons	115	N of comparisons	13,110
Mean	17.0733	Mean	87.0981
Standard Deviation	10.2047	Standard Deviation	13.3727

TABLE 7.3. Summary of Distances between Repeats and Between Different Individuals (PCFA Model)

Repeats		**Different Individuals**	
Statistic	**Value**	**Statistic**	**Value**
N of comparisons	115	N of comparisons	13,110
Mean	23.1354	Mean	92.1178
Standard Deviation	16.1955	Standard Deviation	11.2861

The histograms that follow show the range and distribution of the Euclidean distances between the summed measurements of repeats and non-repeats. Figures 7.1 and 7.2 for the biological model measurements, and 7.3 and 7.4 for the PCFA model measurements, facilitate visual comparison of the significant difference in the ranges of Euclidean distances that separate repeats from one another versus the distances that separate non-repeats from one another. The average Euclidean distance between repeat image sets for the biological and PCFA models are 14.4957, and 16.9631, respectively. This is significantly lower than the average Euclidean distance between the images of non-repeats from the biological model (84.720) and the PCFA model (92.1178).

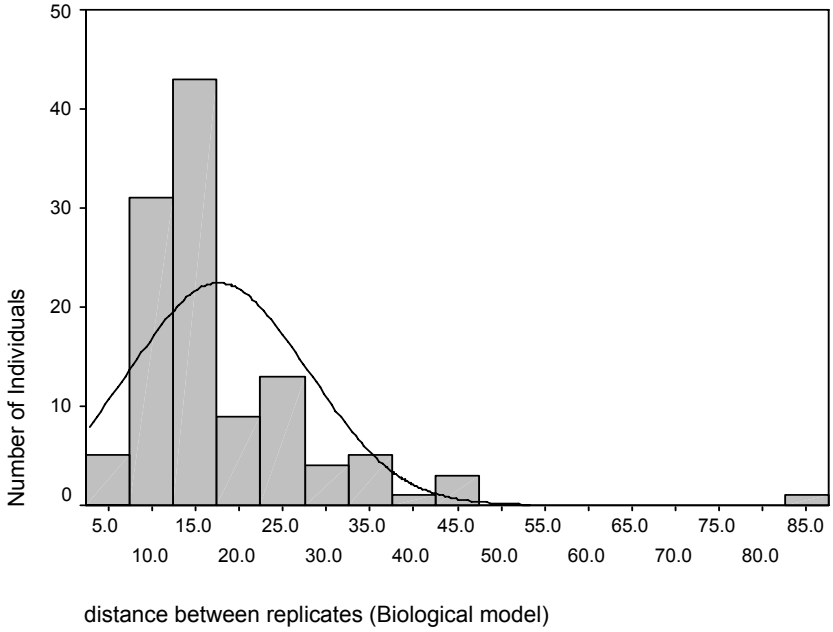

Figure 7.1. *Frequency of Euclidean distances between repeats for the biological model*

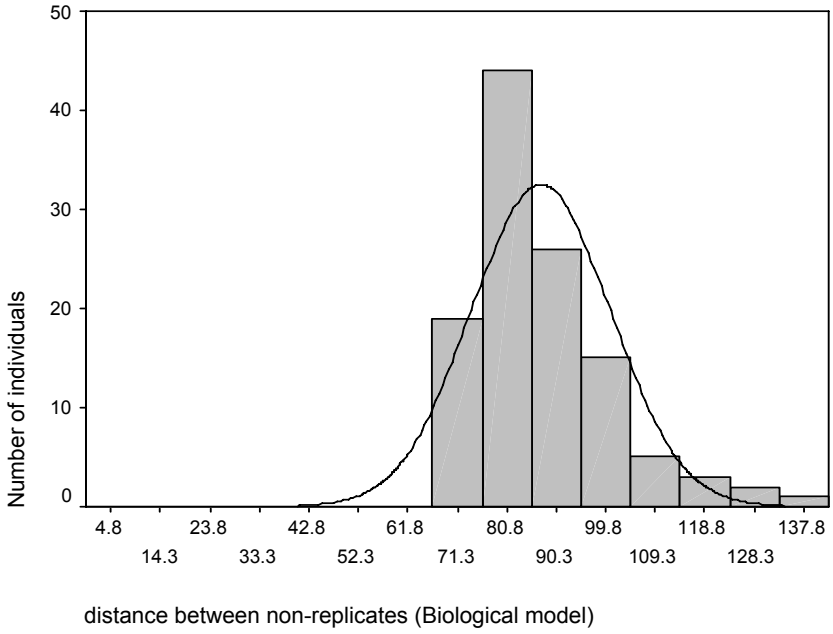

Figure 7.2. *Frequency of Euclidean distances between non-repeats for the biological model*

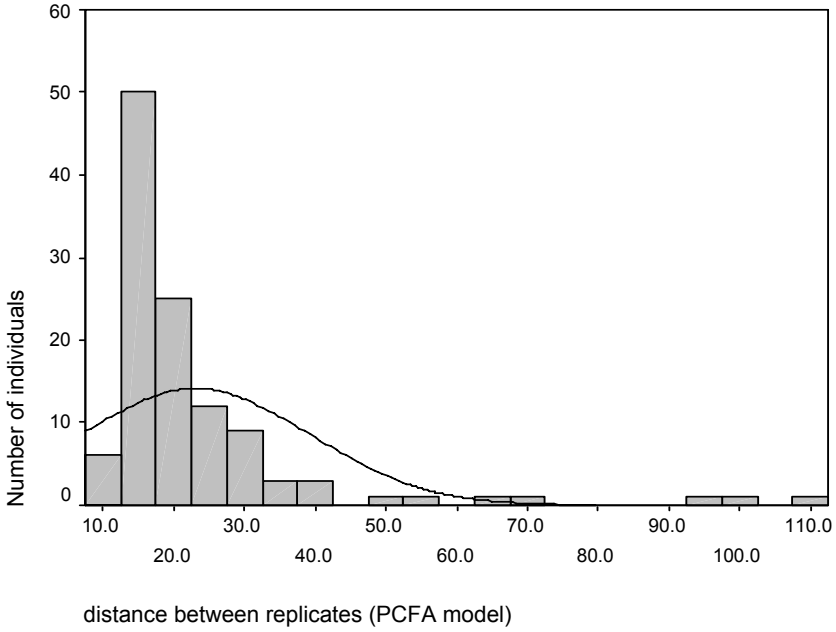

Figure 7.3. *Frequency of Euclidean distances between repeats for the PCFA model*

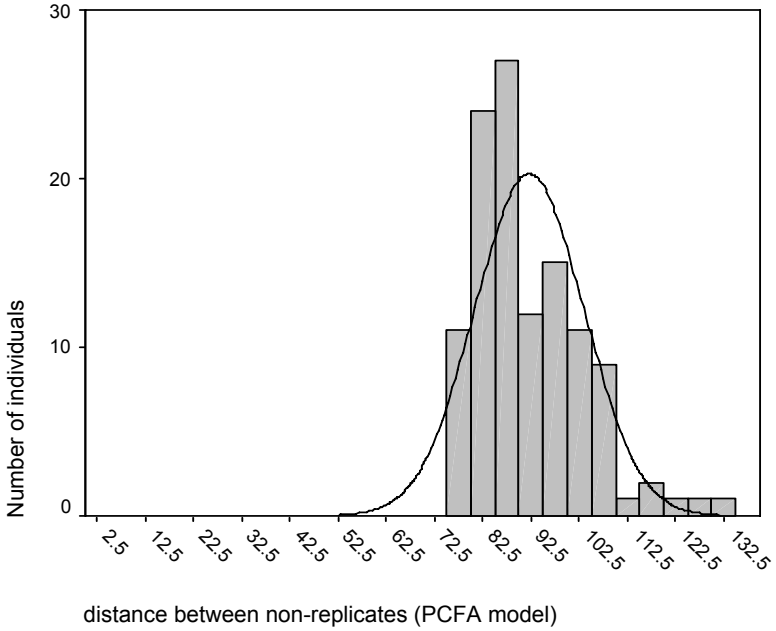

Figure 7.4. *Frequency of Euclidean distances between non-repeats for the PCFA model*

I calculated the percentiles of distribution of the Euclidean distances of both the repeat and non-repeat image comparisons to illustrate the relative percentage of the sample represented by various Euclidean distances between images. The distances that represent various percentiles between repeat and non-repeat images are presented in Table 7.4 (biological model) and 7.5 (PCFA model). For example, the percentage in the left column of Table 7.4 represents the proportion of the sample that is taken into account if the distance between the images being compared is equal to the value in second column from the right. As such, these tables provide a means to compare the extent and characteristics of overlap between repeat and non-repeat distances. There is considerable overlap between the repeat and non-repeat mean distances for both models.

TABLE 7.4. Comparison of Percentiles of Distance Variation Between Repeat and Non Repeat Images for Biological Model

Percentiles of Variation			
Distances Between Repeats		**Distances Between Non-Repeats**	
100%	82.79	100%	140.83
99%	44.65	99%	129.88
95%	33.54	95%	117.90
90%	31.52	90%	104.43
75%	21.58	75%	93.75
50%	13.74	50%	83.58
25%	11.94	25%	77.74
10%	10.71	10%	73.53
5%	9.94	5%	72.28
1%	6.01	1%	70.12
0%	5.79	0%	68.75

TABLE 7.5. Comparison of Percentiles of Distance Variation Between Repeat and Non Repeat Images for PCFA Model

Percentiles of Variation			
Distances Between Repeats		**Distances Between Non-repeats**	
100%	108.40	100%	131.29
99%	99.52	99%	126.55
95%	53.37	95%	112.08
90%	34.42	90%	106.61
75%	24.81	75%	98.59
50%	17.93	50%	89.33
25%	15.28	25%	83.56
10%	13.98	10%	80.01
5%	12.27	5%	77.77
1%	10.28	1%	75.88
0%	9.96	0%	75.46

For both models the Kolmogorov-Smirnov tests of means showed that the differences between the repeat and non-repeat mean summed distances are indeed significant ($p \leq 0.000$) despite the different variances, and in spite of the overlap between them. The Kolmogorov-Smirnov test is designed to determine whether two datasets differ significantly, without making any assumptions about the distribution of the data. Significant variation in mean summed distance between sets of measurements has been shown to reflect shape variation between groups (Christensen, 2005). The results of the test of means displayed in Table 7.6 signify that the petrous portion varies significantly in shape among different individuals.

TABLE 7.6. Kolmogorov-Smirnov tests of means

	Biological model		**PCFA model**	
	Statistic	***p***	**Statistic**	***p***
distance between non-repeats	.121	.000	.131	.000
distance between repeats	.238	.000	.247	.000

I calculated typicality probabilities for both models as a measure of the statistical similarity between repeat images. The typicality probabilities were calculated as relative frequencies for each case by summing the occurrences in the non-repeat (images from different individuals) comparisons of a distance greater than or equal to the distance between that case and its repeat and dividing it by the total number comparisons. The typicality values for the entire set of comparisons are presented in Figures 7.5 and 7.6 for the biological and PCFA models, respectively. Most of the values are very close to one, indicating that the likelihood of the Euclidean distance between an image and any non-repeat being smaller than between that image and its repeat is very small.

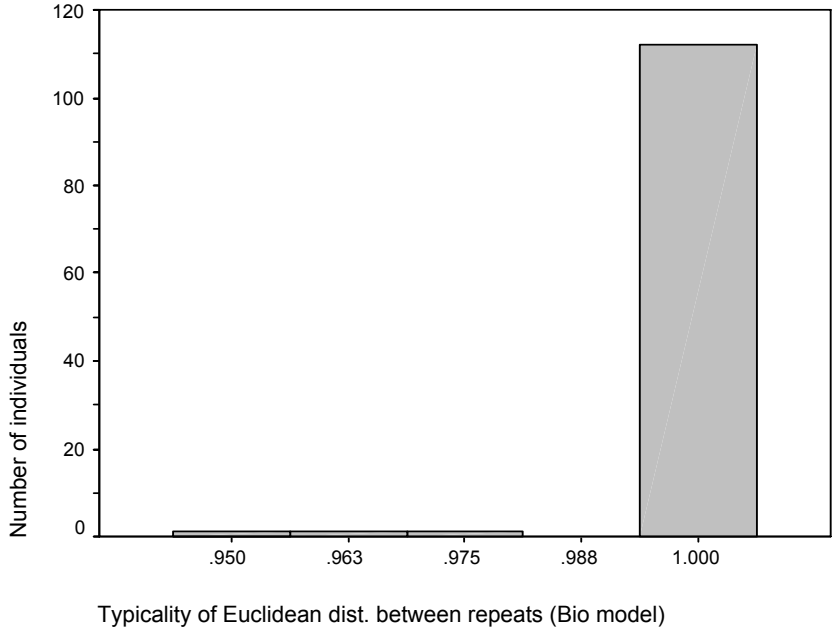

Figure 7.5. *Typicalities of repeat measurement sets (Biological model) Mean=0.999, range=0.950-1.0*

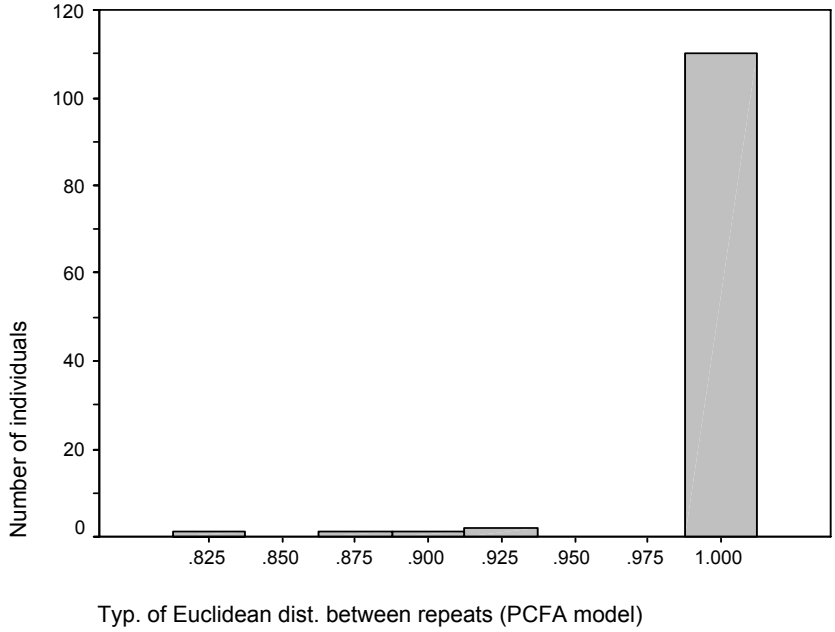

Figure 7.6. *Typicalities of repeat measurement sets (PCFA model) Mean=0.995, range=0.825-1.0*

Visual inspection of the Cartesian coordinates of the points recorded on the images to be compared is a valuable source of evidence regarding the source of error in Euclidean distance comparisons (Christensen, 2005). A plot of the X and Y coordinates of a pair of repeats that are separated by a very small Euclidean distance, is presented in Figure 7.7 to illustrate the proximity that typically characterizes analogous coordinate points between closely matching repeat images. On the other hand, Figure 7.8 is a plot of the coordinate points of and individual whose first and second images were sufficiently separated in Euclidean distance to result in an incorrect match.

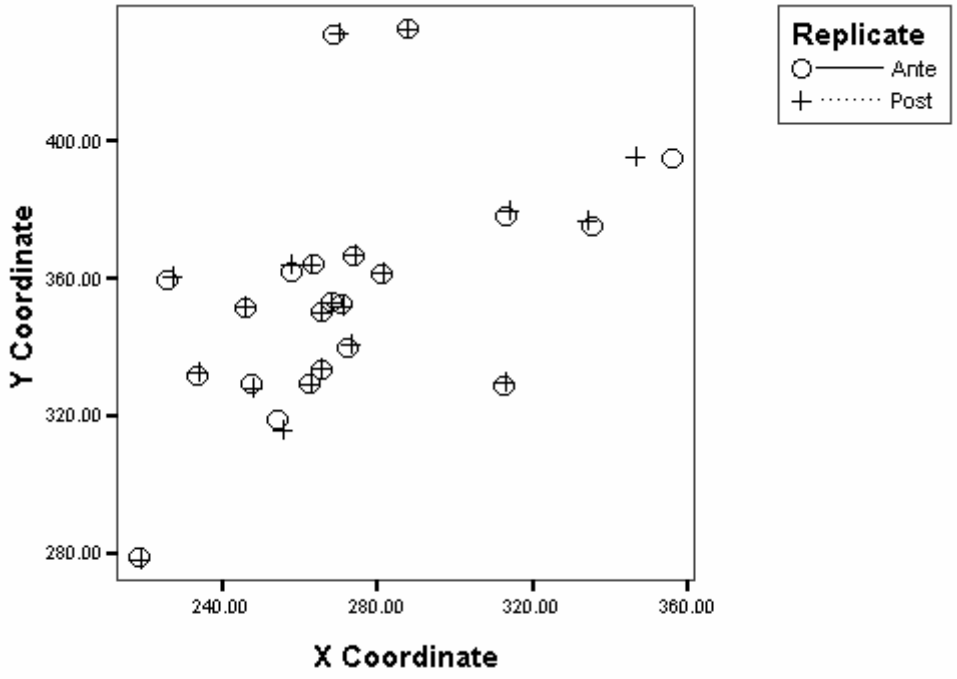

Figure 7.7. *Plot of coordinate points of repeat images that were close to one another in Euclidean distance.*

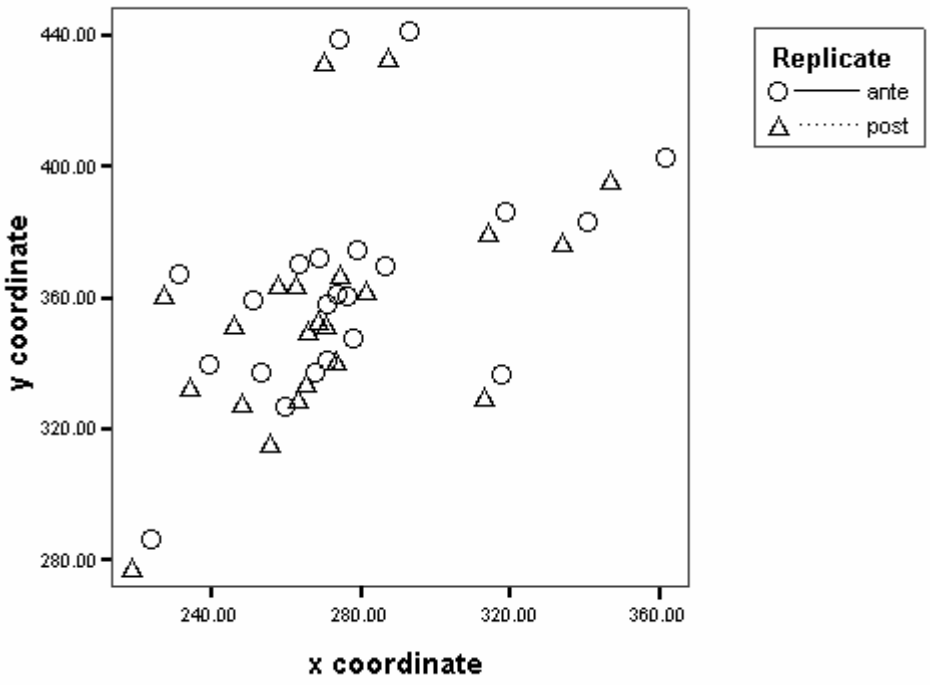

Figure 7.8. *Example plot of the coordinate points from repeat images of an individual whose first and second scans were not nearest neighbors*

These plots allow for visual comparison of the Cartesian relationships between the coordinate points of the first and second images as a means to make inferences about matching errors, and to confirm correct matches. The regularity that characterizes the direction of the shift of each of the landmarks in the postero-lateral direction between the first and second scans shown in Figure 7.8 suggests that the difference resulted from a single factor. Inspection of the CT image sets themselves suggests that the variation between the scans is the result of a difference in the orientation of the axial plane between the first and second scans, possibly the result of a change in the position of the patient between the first and second scans. A similar pattern characterizes the

difference between the repeat scans of each of the individuals (3 in the biological model and 5 in the PCFA model) whose repeat images were not closest in Euclidean distance. Thus caution should be exercised in reproducing the antemortem axial plane in postmortem imagery when this method is applied in the forensic setting.

LIKELIHOOD ESTIMATES

From a legal standpoint, it is necessary to provide an estimate of the reliability of the nearest neighbor associations to satisfy the requirements of the Daubert Guidelines of evidence admissibility. Both a quantified assessment of each individual's uniqueness and the likelihood of misidentification using a method are prerequisites to the determination of its reliability (Robertson and Vignaux, 1995). As such, any statement of individual uniqueness is best presented as the relative probabilities of a match to the correct individual, and to an individual in the general population (Christensen, 2003; Steadman, 2006). I calculated likelihood ratios as a means to make these comparisons.

Likelihood is an estimate of the probability that a hypothesis is true, and in this case, that an association made using this method is correct. The likelihood ratio is the probability of a correct match divided by the probability that it is false (Robertson and Vignaux, 1995). For the sake of continuity, the formulae, methods, and results of the likelihood ratio calculations are presented in the following paragraphs.

Calculation of likelihood ratios

I calculated likelihood ratios for both the biological and PCFA models to use as measures of the relative reliability of nearest neighbor associations made using each of them. The likelihood ratios used in this research were calculated according to the following equation:

$$\text{likelihood ratio} = \frac{\text{positive predictive value}}{\text{(1-negative predictive value)}}$$

where:

$$\text{positive predictive value} = \frac{\text{positive matches}}{\text{(positive matches + false non-matches)}}$$

and:

$$\text{negative predictive value} = \frac{\text{non-matches}}{\text{(false matches + non-matches)}}$$

Figures 7.9 and 7.10 graphically illustrate the results of the nearest neighbor comparison that are relevant to the calculation of the likelihood ratios for this research for the biological and PCFA models respectively. There are four categories of data presented in Figures 7.9 and 7.10 as represented by boxes a-d. Since there are 115 total matches, and 12,996 total non-matches: box **a** represents the number of correct nearest neighbor matches, box **b** contains the number of nearest neighbor matches that were not correct, box **c** represents the number of times a non-match should have been a match, and box **d** the number of correct non-matches. The values within boxes a through d

can be inserted into the equations above to calculate the positive and negative predictive values.

	Correct	Incorrect	Totals
Match	112	3	115
Non match	3	12,993	= 12,996
Totals	= 115	= 12,996	13,111

Figure 7.9. *Values used to calculate the likelihood ratio for the biological model*

	Correct	Incorrect	Totals
Match	110	5	= 115
Non match	5	12,991	= 12,996
Totals	= 115	= 12996	= 13,111

Figure 7.10. *Values used to calculate the likelihood ratio for the PCFA model*

Using the values presented in Figures 7.9 and 7.10, the positive predictive values and negative predictive values used are calculated as follows and the results are presented in Table 7.7.

positive predictive value = a/(a+c)

negative predictive value = 1-(d/(b+d))

The likelihood ratios for the biological and PCFA models were then generated from the positive and negative predictive values according to the formulae:

$$\frac{\text{positive predictive value}}{\text{negative predictive value}}$$

The positive and negative predictive values and the likelihood ratios for both models are presented in Table 7.7. The likelihood ratios for both models are extremely high, suggesting a very high level of probability that a match made using either is correct. Any likelihood ratio greater than 1 favors the correctness of a match, while a ratio less than one represents evidence against a match, with a likelihood of exactly 1 being neutral. Thus any likelihood ratio greater than 1 favors a match, and the further from 1 the ratio is, the greater the probative value of the evidence (Robertson and Vignaux, 1995). For example a likelihood ratio of 10, means that the two images that constitute a match are 10 times (10:1) more likely to belong to the same individual than two any other person in the general population. There is no necessary upper limit for likelihood ratios, and in the case of forensic identification, it is not unusual to attain ratios of several thousand, meaning that two images are several thousand times more likely to belong to the same individual than to any two other individuals.

TABLE 7.7. Likelihood ratios for the biological and PCFA models

	Negative predictive value	Positive predictive value	Likelihood ratio
Biological model	0.0002308403	0.973913	4218.99
PCFA model	0.0003847331	0.956522	2486.19

Posterior probabilities were calculated for both the biological and PCFA models by dividing the likelihood ratios for each by the likelihood ratio plus one. These values represent the probability that an identification is correct assuming that it is as likely to be correct as incorrect. Thus, posterior probabilities are indications of the reliability of a method. For example a posterior probability of .999 means that the probability of a correct identification given a match would be 99%. The posterior probabilities generated from the present data are presented in Table 7.8.

TABLE 7.8. Posterior probabilities for the biological and PCFA models

Model	Posterior probability
Biological model	0.99976803 (99%)
PCFA model	0.99956617 (99%)

Nomograms are useful tools for visualizing the interaction between the likelihood ratio and posterior probability for a particular relationship. Nomograms show pretest probabilities and likelihood ratios along sliding scales that facilitate estimation of the posterior probability that a particular relationship is statistically

meaningful. Their results are generally illustrative rather than exact, but are nevertheless useful in understanding the dynamics of the relationship between likelihood and probability in this research.

Nomograms are presented in Figures 7.11 and 7.12 to illustrate the relationship between the likelihood ratios generated in this research and the probability that nearest neighbor matches made using this method are correct.

The calculator used to generate the nomograms presented in Figures 7.11 and 7.12 (Schwartz, 2006) assumes a prior probability of 1, meaning that there is no corroborative evidence with regard to the correctness of matches made using this method (this idea is discussed in detail in Chapter VIII). Thus for the biological model, a line drawn from a prior probability value of 1 along the left column, through a likelihood ratio of 4218.99 generates a posterior probability above 95%. For the PCFA model, a line drawn from a prior probability of 1 through a likelihood ratio of 2486.19 also generates a posterior probability higher than 95%.

This chapter illustrates the accuracy of the models generated in this research, as well as the potential accuracy with which identifications made be made using this method in the forensic context. These results also illustrate the extent to which the petrous portion of the temporal bone varies between individuals. The size and regularity of the distinction between repeats and non-repeats, as well as the high likelihood ratios and posterior probabilities indicate a very high level of variation between individuals. These results support the

broader notion suggested by biometrics researchers that individual level variability can be extracted from most segments of human anatomy for which there are a sufficient number reliable landmarks available to quantify it (Maltoni et al., 2003).

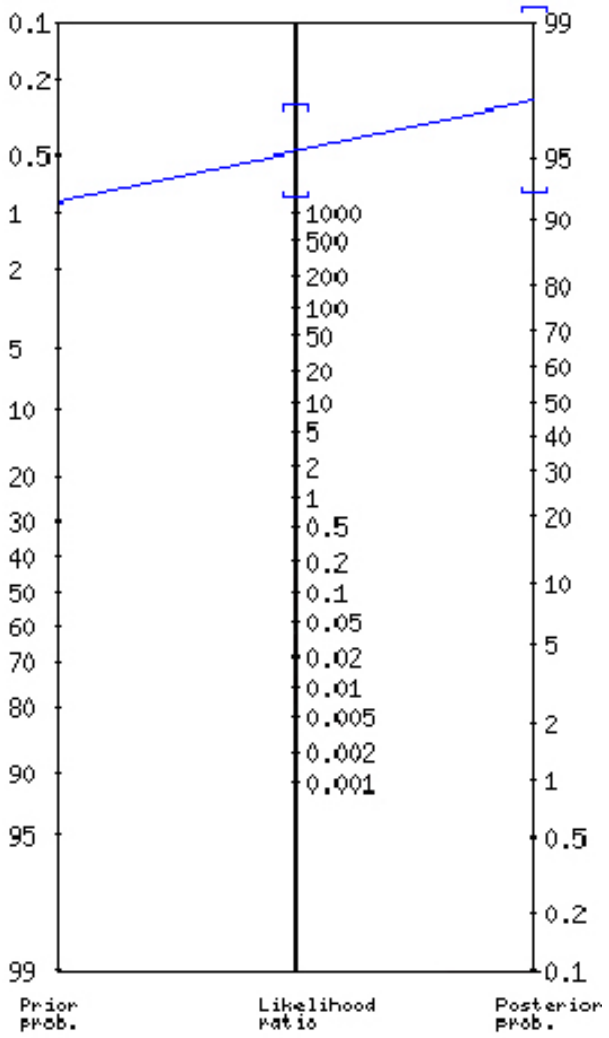

Figure 7.11. *Nomogram illustrating relationship between likelihood ratio and posterior probability for the biological model*

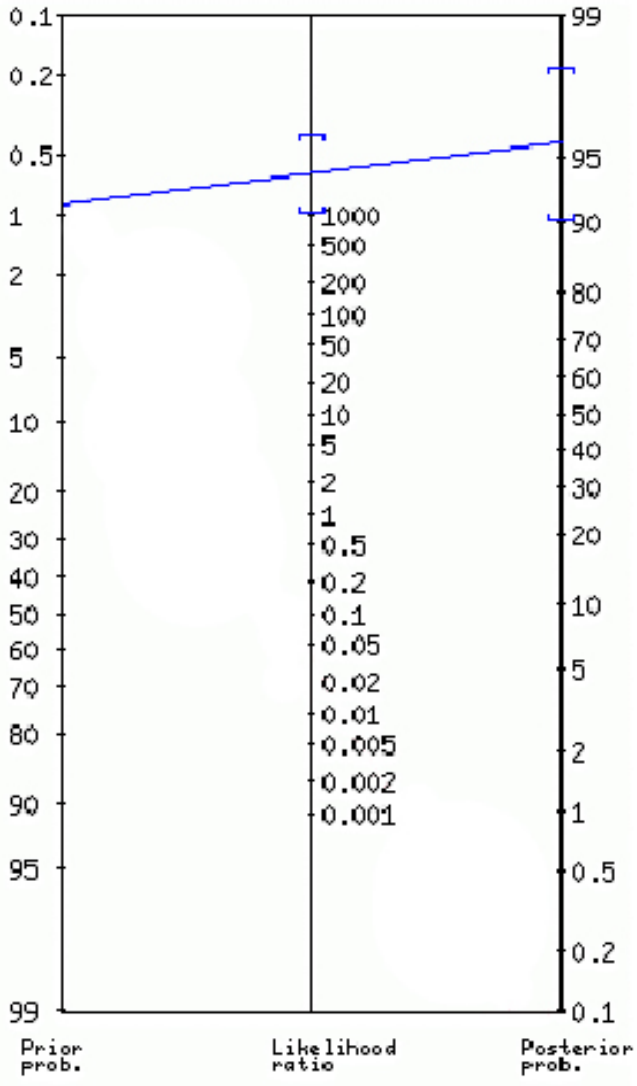

Figure 7.12. *Nomogram illustrating relationship between likelihood ratio and posterior probability for the PCFA model*

CHAPTER VIII

DISCUSSION AND CONCLUSION

This research aimed to evaluate the utility of a morphometric representation of the petrous portion of the human temporal bone in the identification of fragmentary human remains. I addressed several questions in the process. Are there a sufficient number of identifiable and repeatable landmarks to capture individual variation in the human petrous temporal bone? What method of measurement selection yields the highest degree of accuracy in generating correct matches between CT images? Are the measurements of the petrous portion collected in this research sufficiently variable to either verify or dispute that two axial head CT scans of the petrous portion were taken from the same individual? Is the probability of the matches made using this method sufficient to claim a definitive identification? What level of probability is sufficient to make this claim? There is obviously no existing standard with regard to this particular method, but the results presented in the preceding chapters demonstrate that a high level of accuracy and very high likelihood of correct attribution are associated with matches made using this method.

However, it is a misconception that the statistical probabilities used in forensic identification are independent of human judgment. Even DNA evidence is presented only within a framework of assumptions made by the observer (Evett and Weir, 1998). Thus, there is no complete objectivity in forensic

identification (Evett and Weir, 1998). As such, the probabilities associated with assertions of forensic identifications merely represent information to present in support of a professional opinion. In recent years, the courts have begun to require quantification of professional opinion regarding forensic identifications in addition to the quantification of the evidence presented in support of that opinion. The following paragraphs consider the results of the current research within the theoretical framework used in the most rigorous sciences of forensic identification.

BAYES' THEOREM

Since the Daubert ruling (1993) and the amendments to the Federal Rules of Evidence (2000), Bayesian statistics have become the standard in presenting professional opinion regarding the results of forensic DNA identifications (Krawczak and Schmidtke, 1992; Evett and Weir, 1998; Thompson et al., 2003). However, Bayesian statistics have only been applied to evaluate a small number anthropological and/or radiological methods of identification (Christensen, 2005). A recent article encourages more widespread application of Bayesian statistics in anthropological identifications (Steadman et al., 2006). Bayes theorem allows the forensic scientist to generate a quantitative estimate of the chance that an identification is correct using likelihood ratios, prior and posterior odds, and represents a useful and standardized means to convey the strength of identifications in court.

Including those regarding forensic identifications, opinions can vary in strength and, according to Bayes (1764), a rational person's graded beliefs can be represented by a *subjective probability function,* P. For each hypothesis, *H,* about which the person has an opinion, P(*H*) measures his or her level of confidence in *H*'s truth. Conditional beliefs are represented by conditional probabilities, so that $P_E(H)$ measures the person's confidence in *H* on the supposition that *E* is a fact. In other words, Bayes theorem provides a means to calculate the likelihood that an opinion is true based on a known piece of information.

In the present research, this means that there are two probabilities that can be calculated with regard to the strength of an identification. The first is the probability of a match based on petrous temporal bone morphology given that the identification is correct (i.e. that the images compared are known to represent the same individual). This is the probability established in the results of this research. The second probability is a measure of the likelihood that an identification is correct given a match in petrous bone morphology. This is the probability that is generated in forensic identifications, and calculating it requires the application of Bayes theorem (Bayes, 1763), along with some other information. Adapted to this research, Bayes Theorem reads:

Posterior Odds = Likelihood Ratio * Prior Odds

In the case of this research, the posterior odds are a measure of the confidence of a particular identification and are calculated by multiplying the prior odds by the likelihood ratio. Prior odds are a measure of the likelihood of a match given other information that is suggestive of a match (i.e. suspected identity). In other words, the posterior odds represent the likelihood of a correct identification when other evidence is taken into account. The posterior and prior odds are equal (both 1) in cases in which the probability that an identification is correct is the same as the probability that it is incorrect. The results indicate that this is not the case in the current research. The prior odds are greater than 1 in any case in which any information regarding the potential identification of an individual exists, though quantification of these odds is often difficult.

The results of this research as presented in the previous chapter assume a prior odds value of one (the most conservative estimate of correct identification in cases in which there is no other information from which to increase the prior odds), and achieve posterior probabilities that exceed 95% for both models. Any increase in the prior odds will simply further increase the posterior odds associated with this method. Thus from a Bayesian perspective, a very high level of confidence is associated with matches made using this technique without prior information regarding the likelihood of the match, and the consideration of prior information can only increase this confidence.

APPLICATION OF THE METHOD IN FORENSIC IDENTIFICATION

The measures of likelihood discussed above are population level estimates of the accuracy of the method and refer to the strength of matches between images that are known to have repeats in a test population. These results beg two questions regarding the application of this method in the forensic setting. First, how will this method be applicable in the forensic setting and second, what is the probability of an individual match using this method?

The answer to the first question is that the method can be applied in the identification of a set of forensic remains by incorporating the measurement data collected from the image of the deceased into the present data set, and using the nearest neighbor algorithm to generate a match from within that population. The answer to the second question is the most important measure of the accuracy of matches made with this method, and is discussed in detail in the following paragraphs.

Probability of a correct match

In answer to the second question, the actual Euclidean distance between matched images was used to evaluate to the strength of the relationship between them, and the probability that they represent the same individual. The smaller the distance, the more likely it is that the association between them represents a correct match. Thus it was important to generate an estimate of the probability of a correct match for the various Euclidean distances that separate the matches in this data set. This involved establishing: (1) the

approximate Euclidean distance greater than which matches lost sufficient probability of correctness to be considered accurate, and (2) the approximate Euclidean distance below which the probability of a match is high enough to consider the match to be accurate.

There were no incorrect matches made using the biological model when the Euclidean distance between the nearest neighbors was 32 or less, and no incorrect matches were made using the PCFA model when the distance between repeats was 37 or less. This is because there was no smaller distance between any of the comparisons than between the repeat images. This means that the probability that a match between nearest neighbors would represent a correct match is 100% when the Euclidean distance between them is less than 32 or 37 for the biological and PCFA models, respectively.

However, this does not mean that either 32 or 37 represent thresholds past which all matches are suspect. Instead, these numbers represent indicators of the range of distances beyond which incorrect matches become increasingly common. For instance, the Euclidean distance between images was 33 for eight comparisons. Of those, three were comparisons between repeat images, and the other five were between non-repeats. This means that if the Euclidean distance between ante- and postmortem images used in a forensic case is 33, there is only a 37% chance that the two images represent the repeat images from the same individual. Figure 8.1 displays this relationship graphically.

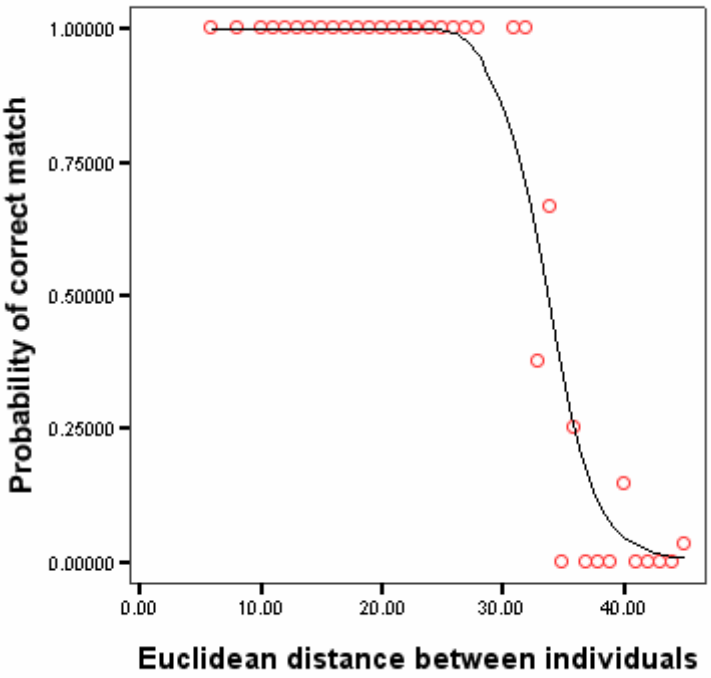

Figure 8.1. *Scatterplot of distances between compared images and the probability that those comparisons represent a correct match with fitted regression line for the Biological Model.*

The regression line in Figure 7.1 suggests that the probability of a correct match diminishes dramatically when the Euclidean distance between images approaches 30. Thus, in the forensic setting, a nearest neighbor match of images that are separated by less than 30 Euclidean distance units can be considered very reliable, and this reliability diminishes dramatically with larger distances. Nearest neighbor matches between images that are 40 or more Euclidean distance units apart rarely represent a correct match.

In theory this is because there should technically be no separation in Euclidean space between two images taken from the same individual if all error is eliminated. However, since error in measurement is unavoidable, the small

distances that separate repeat images in this sample are probably the result of summed measurement error, and generally don't result in a total distance of more than 30. On the other hand, real biological variation in landmark location is less systematic and often more significant than measurement error, and generally results in a distance between images that is greater than 45. Those individuals whose images are separated by Euclidean distances between these two values are marked by a less systematic pattern of measurement error, but not by biological variation in their dimensions. The greater differences between the images of these individuals appears to be the result of combined error of measurement in landmark placement and slight variation in the axial plane between the images being compared. Repeat measurement of a sample of both of the images of ten of these individuals yielded variation that was within the range of variation of standard measurement error, and did not result in change sufficient to move the images significantly, either closer in Euclidean distance or farther apart. This suggests that the repeat measures recaptured variation due to variation in the axial plane, and supports the notion that variation in the axial plane is what resulted in the placement of these individuals within the range of overlap between matches and non-matches.

Similar accuracy characterizes both the biological and PCFA models. Both achieve more than 95% correct classification, and very high likelihood ratios. It is thus difficult to favor one over the other for use in the forensic setting. The PCFA model incorporates 39 measurements between 26

landmarks, and the biological model incorporates 30 measurements between 23 landmarks. Whereas the number of measurements incorporated does not complicate the use of a model because the measurents are calculated from the landmarks and not directly measured, the increased number of landmarks incorporated in the PCFA model may make it more difficult to apply in forensic investigations as well as more prone to error in data collection. The three landmarks that are incorporated into the PCFA model but not in the biological model are the center point of the middle ear (MID), the lateral limit of the jugular canal (JUG), and the vestibule (VBLE). Of these, JUG and MID are both difficult to locate relative to the other landmarks because of their less definitive location. For example, the large diameter of the middle ear may result in more variable estimation of its center (MID) in relation to features with smaller diameters like the semi-circular canals. Locating JUG requires placement of a control point on the boundary of a foramen that also has a large diameter. The open nature of the resultant curve of the boundary along which the point is placed may also result in greater error than the smaller landmarks incorporated in the biological model. The vestibule should not introduce any further error into the model because it is easily located and there is little variation in the location of its center point.

Nevertheless, because the PCFA model requires the collection of more landmark data (3 more landmarks than the biological model), and because of the more diffuse nature of two of the additional landmarks (MID and JUG), I suggest

that the biological model represents a more efficient, and perhaps more reliable measurement set upon which to base this method.

POSSIBLE SOURCES OF ERROR AND LIMITATIONS OF THE METHOD

Variation in the alignment of the axial plane between images is the largest source of error in the present study and represents a considerable source of error in the application of this method in the forensic setting. It is incumbent on the user of this method to approximate the orientation of the antemortem image as closely as possible in postmortem scans. This can best be done using sagittal scout scans taken to correctly orient the patient prior to scanning the axial plane.

Another potential source of error in and possible limitation of this method is variation in landmark placement (and thus measurement values) between skulls with and without soft tissue. Each of the landmarks employed falls on a distinct boundary between bony and soft tissue and thus should represent a minimal source of error, but the possibility of error has not been evaluated. It is possible that differences between images with and without soft tissue may result from variation in the amount of radiation that passes through the specimens as related to the presence or absence of soft tissue. Postmortem user settings may have to be adjusted to approximate the appearance of tissues on the antemortem image.

Availability of antemortem CT imagery is a limiting factor in the applicability of this method. CT images of the head are taken for a variety of

diagnoses and are becoming more and more frequently available for comparison. However, their frequent use is generally limited to industrialized parts of the world, and to individuals who can afford the costs associated with them. Thus, the current utility of this method is likely limited to North America, Europe and parts of Asia, with periodic applicability in other areas. This is an unfortunate limitation since many of the most significant disasters take place in parts of the world with far less pervasive availability of CT technology. However, the method would still be useful for the identification of citizens of industrialized countries who die as a result of terrorism or disasters in other parts of the world. These types of situations may in fact represent some of the most useful contexts for the application of this method, since they will often be associated with air crashes, or terrorist attacks on political targets that have closed populations, with reliable records of victim identities.

Even in areas where CT is used frequently including the United States, there are issues regarding the length of time that hospitals curate the images, the format in which they are stored, and the user parameters of the images. In the United States, federal law requires storage of radiographic imagery for a minimum of five years (Code of Federal Regulations, - 42 CFR 482.26(d)(2)), and most hospitals curate them for considerably longer than that. Variation in the curation time is related in large part to storage space, and is greater in countries other than the U.S. Most U.S. hospitals now curate images in a digital format, which minimizes the costs associated with storing them for long periods

of time. However, some digital formats including JPEG record only the image and whatever information is recorded on the image, and as a result do not facilitate postmortem adjustment of the user parameters, including scale and window settings. Variation in window setting has significant effect on the appearance of different tissue types, and could render this method useless, though fairly accurate replication of the antemortem window settings can typically be achieved in the postmortem image by an experienced radiologist. Similarly, variation in scale between ante- and postmortem imagery represents a considerable obstacle to identification using this method, but an experienced observer should be able to repeat the scale of the antemortem image fairly accurately.

I did not evaluate the influence of scanning film copies of CT images for comparison, but future research should evaluate possible variation in measurement accuracy associated with the use of film copies. The quality of available imagery is also a limiting factor in the use of this method, as the accuracy of this method depends on image quality.

Just as with all other identifiers, corroborative evidence must be used to limit the number of comparisons made in attempts to identify human remains. This presents a far more significant problem in large scale disasters like the recent tsunami in Asia, which killed large numbers of European tourists for whom there were more likely to be available CT images, but whose remains are far removed from locations or possessions that might facilitate their

identification. Thus, this method is most applicable in attempts to identify members of closed populations including air disasters, and terrorist bombings of closed buildings.

Ontogenetic influence is another potential limitation of this method, as it can cloud individual level variability in the temporal bone, especially in measurements between the closest features of the petrous bone. From an ontogenetic standpoint, it is important to avoid dimensions of the petrous portion of the temporal bone that are most susceptible to ontogenetic changes due to musculature, age or any other factor. In terms of musculature, it is important to avoid the mastoid processes, in spite of their utility as indicators of the lateral extent of the temporal bone, and the variation in their patterns of pneumatization.

Developmental change has considerable influence on some of the dimensions of the petrous portion. Whereas the structure of the inner and middle ear reach their adult dimensions at or near birth, the segments of the petrous that lie medially and laterally of the ear apparatus continue to grow into adolescence to form the adult bone. The current research incorporated only adult images for this reason, and the accuracy of this method would likely be compromised considerably if comparisons were made between images taken at different developmental stages. Thus it is recommended that the application of this method be limited to adult skeletal remains. However a smaller measurement set, incorporating only the smaller dimensions of the inner and

middle ear components might allow comparison of subadult remains, and represents an interesting avenue for future research.

In addition, I did not include the ear ossicles because they undergo considerable are age-related degenerative changes that can influence their structure. The ossicles are also prone to postmortem positional changes associated with decomposition of their ligamentous attachments to the surrounding bone.

Pathological change in the morphology of the petrous portion of the temporal bone associated with disease may also be a source of error in the application of this method. Various diseases can have rather slight, but in this case critical, influences on the morphology of the temporal bone, particularly with regard to the smaller apparatuses within the petrous portion that are associated with hearing and balance. I only included images that were free of obvious signs of pathological change, but there is obviously a correlation between disease and the CT imagery. Individuals for whom there are antemortem CTs available clearly suffered from symptoms that required CT imagery to diagnose. Thus, it is probably more likely to find pathological changes in individuals with CT scans than in the general population. Careful consideration of the clinical history of a missing person may be important to the achievement of a successful identification. However, only a small number (eight) of images from my original image set showed any signs of pathology.

FUTURE RESEARCH

Future research should focus on answering questions raised during the current research, and in the development of other, perhaps easier methods of quantifying the morphology of the petrous portion. First, it is important to evaluate this method on an actual forensic sample composed of fragmentary remains, as well as to evaluate the difference in measurement values collected from skulls with and without soft tissue. There is also a need to evaluate the potential for error associated with comparing measurements collected from printed and digital CT images.

The most important factor to contend with in future research will likely be the extent to which difficulty in approximating the antemortem axial plane in the postmortem image influences the accuracy of this method. Forensic remains are often fragmentary, and successful orientation of cranial fragments in the CT gantry will be difficult to achieve. In the interest of circumventing this complication, future research should investigate the use of three-dimensional reconstructions of postmortem scans as a means to facilitate the approximation of the antemortem image by allowing rotation of the reconstructed image into the desired plane.

In the interest of developing a simpler method of quantifying the morphology of the petrous portion, it may be useful to attempt to apply Elliptical Fourier analysis to the shape of the posterior wall of the petrous portion. Comparison of the Euclidean distances between the coefficients generated by

the Fourier analysis will be used in the same way as they are in the current research. There is a successful precedent for this research using outlines of the frontal sinuses (Christensen, 2005).

It may also be useful to repeat the technique using MRI imagery. MRI is much preferred to CT in the visualization of the soft tissue and fluid anatomy, and for this reason MRI essentially represents an independent, and additional source of antemortem data. Whereas CT of the inner ear for example allows for visualization of the bony labyrinth including the cochlea, vestibule and semi-circular canals, MRI images of the inner ear are generated by the membranous labyrinth, endolymph and periplymph (Jackler, 1988; Jackler and Dillon, 1988). My landmark set involves a variety of the features of the inner, and middle ear, most of which have soft tissue analogs in MRI imagery. The cochlea, for example is usually visible at the anterior terminus of the internal auditory canal. The vestibular apparatus is also visible on MRI, typically as two ovoid masses in the region of the vestibule. Most of the ear structures are visible in this way. The bony dimensions of features outside of the ear apparatus, including the internal auditory canal can also often be inferred from their soft tissue contents. The neural bundles within the internal auditory canal for example are well demonstrated on MRI, and the location of the bony confines of these tissues can be fairly accurate. Thus, a more inferential landmark set based on the placement of bony landmarks within the surrounding soft tissue context

represented on MRI will likely yield accurate results. In fact this is the intended focus of future research because of the increase in MRI usage relative to CT.

The major complicating factor in the use of MRI in comparison of ante and postmortem imagery is decomposition. For the same reason that one cannot reliably use the ear ossicles as landmarks --namely that decomposition irreparably disassociates soft tissues as well as the bones suspended by them-- one cannot use soft tissue landmarks in postmortem imagery. Just as in CT, there are means by which MRI images can be used to more effectively represent bone, but the problem with this is two-fold: 1) CT would most likely have been used to visualize postmortem bony anatomy; and as a result, 1) postmortem images taken after this adjustment will not be reproductions of the antemortem imagery, since MRI would more likely have been used to visualize soft tissue anatomy in the ante mortem setting.

A potential solution to this paradox, and the focus of future research, is to make comparisons of antemortem MRI images to postmortem CT images. The CT images taken after death would represent bone as in life, and as such, their accuracy would not be compromised by decompositional changes to the soft tissue. At the same time, if I use MRI ante mortem imagery I would, have a potentially greater number of ante mortem records with which to make comparisons. The problem is then how do I compare drastically different CT and MRI images? This is the emphasis of future research that will undoubtedly involve demonstrating the degree of association between soft tissue and bony

landmarks as seen separately on MRI and CT scans, respectively. This will introduce an entirely new set of methodologically oriented concerns, the most important of which will be measurement error. Nonetheless, comparison of this type is more methodologically sound than comparison of ante- and postmortem MRI images of the cranial base. It should be noted that the 3D Doctor program used in the current research can be effectively use in the analysis of MRI imagery.

CONCLUSION

In conclusion, the purposes of this research were: (1) to empirically investigate variability in the shape of the petrous portion of the human temporal bone using two-dimensional morphometric analysis, (2) to evaluate the reliability of the resultant method in identification, and to estimate the probabilities of identifications and misidentifications associated with it, and (3) to consider the utility of the method within the framework of Bayesian theory in light of recent rulings regarding the admissibility of forensic testimony.

This research demonstrates that the Euclidean distances between the summed measurements of the petrous portion used in this research are significantly larger between different individuals than between repeats of the same individual, and thus that the morphology of each individuals' petrous temporal bone is quantifiably distinct.

The high rates of correct matches, high likelihood ratios and high posterior probabilities generated for both the biological and PCFA models

demonstrate that nearest neighbor matches made using either of the models are reliable methods of either confirming or rejecting a putative identification, particularly if prior probabilities are taken into consideration. In addition, the probabilities of a correct match relative to the Euclidean distance between repeat images were generated to facilitate evaluation of the strength of matches made when this method is applied in the forensic setting.

The current method lends itself to evaluation according to Bayes' theorem, which is important given the courts' history of emphasizing the *Daubert* guidelines (such as in the case of fingerprint evidence). Whereas most of the anthropological methods of positive identification fail in this regard, as reviewed in Chapter II, the current method has the potential to achieve levels of accuracy and reliability that should precipitate convincing arguments in courts of law. I suggest that the method presented in this research represents a valuable means to identify individual remains, particularly in the mass disaster context both because of its accuracy, and because of the resistance of the petrous portion to taphonomic destruction, and consequently frequent preservation following mass disasters. I also hope that this research will generate interest among forensic scientists in general, and forensic anthropologists specifically, in evaluating the accuracy of existing and future methods of identification with the Daubert guidelines in mind.

REFERENCES

3D Doctor. 1993. Able Software. Lexington, Mass.

Adams WS. 1951. The Aetiology of Swimmer's Exostoses of the External Auditory Canals and of Associated Changes in Hearing. Journal of Laryngology and Otology 65: 133-153.

Aiello L, Dean C. 2002. An Introduction to Human Evolutionary Anatomy. London: Elsevier

Anderson JE. 1960. The Development of the Tympanic Plate. National Museum of Canada Bulletin 180: 143-153.

Andrews P. 1984. An Alternative Interpretation of Characters Used to Define *Homo erectus*: The Early Evolution of Man with Special Emphasis on Southeast Asia and Africa. Courier Forschungsinstitut Senckenberg 69: 167–175.

Anson BJ, Donaldson JA. 1972. Surgical Anatomy of the Temporal Bone and Ear. New York: W.B. Saunders Company.

Anson BJ, Bast TH, Cauldwell EW. 1948. The Development of the Auditory Ossicles, the Otic Capsule and the Extracapsular Tissues. Annals of Otology, Rhinology and Laryngology 57: 603-632.

Anson BJ, Bast TH, Richamy SF. 1955. The Fetal and Early Postnatal Development of the Tympanic Ring and Related Structures in Man. Annals of Otology, Rhinology and Laryngology 64: 802-822.

Anson BJ, Bast TH. 1958. Anatomical Structure of the Stapes and the Relation of the Stapedial Footplate to Vital Parts of the Otic Labyrinth. Annals of Otology, Rhinology, and Laryngology 67: 389-399.

Anson BJ, Hanson JS, Richamy SF. 1960. Early Embryology of the Auditory Ossicles and Associated Structures in Relation to Certain Anomalies Observed Clinically. Annals of Otology, Rhinology and Laryngology 69: 427-447.

Anton SC. 2002. Evolutionary Significance of Cranial Variation in Asian *Homo erectus*. American Journal of Physical Anthropology 117: 301-323.

Anton SC. 2003. Natural History of *Homo erectus*. Yearbook of Physical Anthropology 46:126-170.

Asherson N. 1965. Identification by Frontal Sinus Prints: A Forensic Medical Pilot Survey. London: H.K. Lewis.

Athreya S, Glanz M. 2003. Impact of Character Correlation and Variable Groupings on Modern Human Population Tree Resolution. American Journal of Physical Anthropology 122: 134-146.

Bach-Petersen S, Kjaer I. 1993. Ossification of Lateral Components of the Prenatal Cranial Base. Journal of Craniofacial Genetics and Developmental Biology 13: 76-82.

Balzeau A, Grimaud-Herve D. 2006. Cranial Base Morphology and Temporal Bone Pneumatization in Asian *Homo erectus*. Journal of Human Evolution 48(6): 535-553.

Bast TH. 1930. Ossification of the Otic Capsule in Human Fetuses. Contributions to Embryology 21: 53-82.

Baxter BS, Sorenson JA. 1981. Factors Affecting the Measurement of Size and CT Number in Computed Tomography. Investigative Radiology 15: 337-341.

Bayes T. 1764. An Essay Toward Solving a Problem in the Doctrine of Chances. Philosophical Transactions of the Royal Society of London 53: 370-418

Beatty CW, Suh KW, Harris LD, Reese DF. 1981. Comparative Study Using Computed Tomographic Thin-Section Zoom Reconstructions and Anatomic Macrosections of the Temporal Bone. Annals of Otology, Rhinology, and Laryngology 90(6): 643-649.

Belal A. 1975. Prebycusis: Physiological or Pathological. Journal of Laryngology and Otology 89(10): 1011-1025.

Blackith RE, Reyment RA. 1971. Multivariate Morphometrics. London: Academic Press.

Bluestone CD. 2000. Clinical Course, Complications, and Sequelae of Acute Otitis Media. The Pediatric Infectious Disease Journal 19(5): 37-46.

Bonaldi LV, de Angelis MA, Smith RL. 1997. Developmental Study of the Round Window Region. Acta Anatomica 159: 25-29.

Boule M, Vallois HV. 1957. Fossil Men. New York: Dryden Press.

Brogan M, Chakeres DW. 1989. Computed Tomography and Magnetic Resonance Imaging of the Normal Anatomy of the Temporal Bone. Seminars in Ultrasound, CT, and MR 10(3): 178-194.

Cameron N. 1986. The Methods of Auxological Anthropometry. In Human Growth: A Comprehensive Treatise, vol 3. eds. Falkner F, Tanner JM. New York, Plenum Press. p. 3-46.

Camps FE. 1969. Radiology and its Forensic Application. In: Camps RD, editor. Recent Advances in Forensic Pathology. London: Churchill. p 149-160.

Casselman JW. 1996. Temporal Bone Imaging. Head and Neck Imaging 6(2): 265-289.

Castellote AA, Torres J, Whyte T, Sarrat R. 1997. Contribution to the Morphological Knowledge of the Articulations of the Human Tympanic Ossicular Chain. Acta Otorhinologica 48(4): 269-274.

Cavalcanti MGP, Rocha SS, Rocha M, Vannier MW. 2004. Craniofacial Measurements Based on 3D-CT volume rendering: Implications for Clinical Applications. Dentomaxillofacial Radiology 33:170-176.

Chakeres DW, Spiegel PK. 1983. A Systematic Technique for Comprehensive Evaluation of the Temporal Bone by Computed Tomography. Radiology 146: 97-106.

Chakeres DW, Weider DJ. 1985. Computed Tomography of the Ossicles. Neuroradiology 27(2): 99-107.

Chandra-Sekharan P. 1985. Identification of Skull from its Suture Pattern. Forensic Science International 27: 205-214.

Checkley DR, Zhu WP, Antoun N, Chen SZ, Isherwood I. 1984. An Investigation into the Problems of Attenuation and Area Measurements Made From CT Images of Pulmonary Nodules. Journal of Computer Assisted Tomography 8(2): 237-243.

Cheverud JM. 1982. Phenotypic, Genetic, and Environmental Morphological Integration in the Cranium. Evolution 36: 499-516.

Cheverud JM. 1995. Morphological Integration in the Saddlebacked Tamarin (*Saguinis fuscicollis*) Cranium. American Naturalist 145: 63-89.

Christiansen EL, Thomson JR, Kipp S. 1986. Intra and Interobserver Variability and Accuracy in the Determination of Linear and Angular Measurements in Computed Tomography: An In Vitro and In Situ Study of Human Mandibles. Acta Odontologica Scandinavica 44: 221-229.

Christensen A. 2004. Assessing the Variation in Individual Frontal Sinus Outlines. American Journal of Physical Anthropology 127(3): 291-295.

Clunie DA, Carrino J. 2001. DICOM. In: Mehta A. editor. PACS: A Guide to the Digital Revolution. New York: Springer Verlag.

Code of Federal Regulations 42 482.26(d)(2)

Colbert E, Morales M. 1991. Evolution of the Vertebrates: A History of Backboned Animals Through Time. New York: Wiley-Liss.

Condemi S. 1991. Circeo I and Variability Among Classic Neanderthals. In: Piperno M,Scichilone G, editors. The Circeo 1 Neanderthal Skull: Studies and Documentation. Rome: Instituto Poligraphico e Zecca dello Stato.

Culbert WL, Law FM. 1927. Identification by Comparison With Roentgenograms of Nasal Accessory Sinuses and Mastoid Processes. Journal of the American Medical Association 88: 1634-1636.

Dahm MC, Shepherd RK, Clark GM. 1993. The Postnatal Growth of the Temporal Bone and its Implications for Cochlear Implantation in Children. Acta Oto-Laryngologica 505:1-27.

Daubert v. Merrel Dow Pharmaceuticals, Inc., 509 U.S. 579 (1993)

Davidson HC. 2002. Imaging of the Temporal Bone. Magnetic Resonance Imaging Clinics of North America 10: 573-613.

Dean MC, Wood DA. 1981. Metrical Analysis of the Basicranium of Extant Hominoids and Australopithecus. American Journal of Physical Anthropology 59: 53-71.

Dean D, Hublin JJ, Holloway R, Ziegler R. 1998. On the Phylogenetic Position of the Pre-Neanderthal Specimen from Reilingen, Germany. Journal of Human Evolution 34: 485-508.

Delson E, Harvati K, Reddy D, Marcus LF, Mowbray K, Sawyer FJ, Jacob T, Marquez S. 2001. Sambungmachan 3 *Homo erectus* Calvaria: A Comparative Morphometric and Morphological Analysis. Anatomical Record 262: 297-380.

de Ruiter DJ, Steininger CM, Berger LR. 2006. A Cranial Base of *Australopithecus robustus* from the Hanging Remnant of Member 1, Swartkrans, South Africa. Unpublished manuscript.

Eby TL, Nadol JB. 1986. Postnatal Growth of the Human Temporal Bone. Implications for Cochlear Implants in Children. Annals of Otology, Rhinology and Laryngology 95: 356-364.

Enlow DH. 1990. The Plan of the Human Face. Facial Growth. 3rd ed. Philadelphia: W.B. Saunders.

Enlow DH, Hans MG. 1996. Essentials of Facial Growth. Philadelphia: W.B. Saunders.

Eubanks BA, Cann CE, Brant-Zawadzki M. 1985. CT Measurement of the Diameter of Spinal Cord and other Bony Canals: Effects of Section Angle and Thickness. Radiology 157(1): 243-246.

Evett IW, Wier BS. 1998. Interpreting DNA Evidence: Statistical Genetics for Forensic Scientists. Sunderland: Sinauer Associates Inc.

Federal Rules of Evidence. 1975; 2000.

Feng Z, Ziv I. Rho J. 1996. The Accuracy of Computed Tomography-Based Linear Measurements of Human Femora and Titanium Stem. Investigative Radiology 31(6): 333-337.

Frye v. United States, 54 App.D.C. 46, 293F. 1013 1923.

Goodenough DK, Weaver K, Davis D, La Falce S. 1981. Averaging Limitations of Computed Tomography. American Journal of Neuroradiology 2: 585-588.

Gordon CC, Bradtmiller B. 1992. Interobserver Error in Large-Scale Anthropometric Survey. American Journal of Human Biology 4: 253-263.

Graw M, Czarnetzki A, Haffner HT. 1999. The Form of the Supraorbital Margin as a Criterion in Identification of Sex From the Skull: Investigations Based on Modern Human Skulls. American Journal of Physical Anthropology 108(1): 91-96.

Greulich WW. 1960. Skeletal Feature: Visible on Roentgenogram of Hand and Wrist Which Can Be Used For Establishing Individual Identification. American Journal of Roentgenology Radiation and Thermonuclear Medicine 83(4): 756-764.

Gulya J, Schuknecht H. 1995. Anatomy of the Temporal Bone with Surgical Implications. New York: Parthenon Publishing Group.

Haaga J, Sartoris DJ, Zerhouni EA, Lanzieri CF. 1994. Computed Tomography and Magnetic Resonance Imaging of the Whole Body. Volume 1. New York: Mosby International.

Habicht JP, Yarbrough C, Martorell R. 1979. Anthropometric Field Methods: Criteria for Selection. In Jeliffe DB, Jeliffe EFP. Nutrition and Growth. New York: Plenum Press, p 365-387.

Harvati K. 2003. Quantitative Analysis of Neanderthal Temporal Bone Morphology Using Three Dimensional Geometric Morphometrics. American Journal of Physical Anthropology 120: 323-338.

Heymsfield SB, McManus CB, Sietz SB, Nixon DW, Andrews JS. 1984. Anthropometric Assesement of Adult Protein-Energy Malnutrition. In Wright RA, Heymsfield SB, McManus CB, editors. Nutritional Assessment. Boston, MA: Blackwell Scientific Publications, p 27-81.

Hildebolt CF, Vannier MW. 1988. Three-Dimensional Measurement Accuracy of Skull Surface Landmarks. American Journal of Physical Anthropollogy 76(4): 497-503.

Hildebolt CF, Vannier MW, Knapp RH. 1990. Validation Study of Skull Three Dimensional Computerized Tomography Measurements. American Journal of Physical Anthropology 82:283-294.

Holland TD. 1986. Sex Determination of Fragmentary Crania by Analysis of the Cranial Base. American Journal of Physical Anthropology 70: 203-208.

Hounsfield GN. 1976. Picture Quality of Computed Tomography. American Journal of Roentgenology 127:3-9.

Hsieh J. 2003. CT: Principals, Design, Artifacts and Recent Advances. Bellingham, Washington: International Society for Optical Engineering Press.

Hyman L. 1961. Comparative Vertebrate Anatomy. Chicago: University of Chicago Press.

Israel H. 1973. Age Factor and the Pattern of Change in Craniofacial Structures. American Journal of Physical Anthropology 39: 111-128.

Israel H. 1977. The Dichotomous Pattern of Craniofacial Expansion During Aging. American Journal of Physical Anthropology 47: 47-51.

Jackler RK, Dillon WP. 1988. Computed Tomography and Magnetic Resonance Imaging of the Inner Ear. Otolaryngology 99(5): 494-504.

Jackler RK. 1988. CT and MRI of the Ear and the Temporal Bone: Current State of the Art and Future Prospects. The American Journal of Otology 9(3): 232-239.

Jain A, Chen H. 2004. Matching of Dental X-ray Images for Human Identification. Pattern Recognition 37: 1519-1532.

Jamison P, Zegura S. 1974. A Univariate and Multivariate Examination of Measurement Error in Anthropometry. American Journal of Physical Anthropology 40: 197-204.

Janvier P. 1996. Early Vertebrates. London: Oxford University Press.

Kalendar WA. 2006. Fundamentals, System, Technology, Image Quality, Applications. New York: Wiley and Sons.

Kalmey JK, Rathbun TA. 1996. Sex Determination by Discriminant Function Analysis of the Petrous Portion of the Temporal Bone. Journal of Forensic Sciences 41(5): 865-867.

Kennedy GE. 1991. On the Autapomorphic Traits of *Homo erectus*. Journal of Human Evolution 20:375-412.

Kennedy GE. 1986. The Relationship Between Auditory Exostoses and Cold Water: A Latitudinal Analysis. American Journal of Physical Anthropology 71(4): 401-405.

Kidder JH, Durband AC. 2004. A Re-evaluation of the Metric Diversity within *Homo Erectus*. Journal of Human Evolution 46: 297-313.

Kim SJ, Jang YJ, Jeon SJ. 2003. Anomalous Vein in the Middle Cranial Fossa Associated with the Tegmen Tympani Defect. Otology and Neurotology 24(6): 935-938.

Kimbel WH , White TD, Johanson DC. 1984. Cranial Morphology of *Australopithecus afarensis*: a Comparative Study Based on a Composite Reconstruction of the Adult Skull. American Journal of Physical Anthropology 64(4): 337-388.

Kirk NJ, Wood RE. 2002. Skeletal Identification using the Frontal Sinus Region: a Retrospective Study of 39 Cases. Journal of Forensic Sciences 47(2): 318-323.

Koehler PR, Anderson RE, Baxter B. 1979. The Effect of Computed Tomography Viewer Controls on Anatomical Measurements. Radiology 130: 189-194.

Krawckzak M, Schmidtke J. 1992. The Decision Theory of Paternity Disputes: Optimization Considerations Applied to Multilocus DNA Fingerprinting. Journal of Forensic Sciences 37(6): 1525-1533.

Lande R, Arnold SJ. 1983. The Measurement of Selection on Correlated Characters. Evolution 37: 1210-1226.

Le Gros Clark WE. 1947. Observations of the Anatomy of the Fossil Australopithecine. Journal of Anatomy 81: 300-333.

Lieberman DE, Ross CF, Ravosa MJ. 2000. The Primate Cranial Base: Ontogeny, Function, and Integration. Yearbook of Physical Anthropology 43: 117-169.

Littleton JT, Shaffer KA. 1981. Temporal Bone: Comparison of Pluridirectional Tomography and High Resolution Computed Tomography. American Journal of Roentgenology 137: 835-845.

Lockwood CA, Lynch JM, Kimbel WH. 2002. Quantifying Temporal Bone Morphology of Great Apes and Humans: An Approach Using Geometric Morphometrics. Journal of Anatomy 201: 447-464.

Ma L, Tan T, Wang Y, Zhang D. 2003. Personal Identification Based on Iris Texture Analysis. IEEE Transactions on Pattern Analysis and Machine Intelligence 25 (12): 1519-1533.

Magnusson A. 1987. Object Size Determination at Computed Tomography. Upsala Journal of Medical Science 92:276-286.

Mao JJ, Wang X, Kopher RA. 2003. Biomechanics of Craniofacial Sutures: Orthopedic Implications. Angle Orthodontist 73(2): 128-135.

Maltoni D, Maio D, Jain AK, Prabhakar S. 2003. Handbook of Fingerprint Recognition. New York: Springer-Verlag.

Marlin DC, Clark MA. 1991. Identification of Human Remains by Comparison of Frontal Sinus Radiographs. Journal of Forensic Sciences 36: 1765-1772.

Martinez I, Arsuaga JL. 1994. The Temporal Bones from Sima de los Huesos Middle Pleistocene Site (Sierra de Atapuerca, Spain): A Phylogenetic Approach. Journal of Human Evolution 33: 283-318.

Mayer J. 1935. Identification by Sinus Prints. Virginia Medical Monthly 62: 517-519.

Matteson SR, Bechtold W, Phillips C. Staab EV. 1989. A Method for Three-Dimensional Image Reformation for Quantitative Cephalometric Analysis. Journal of Oral and Maxillofacial Surgery 47(10): 1053-1061.

Meunier P, Yin S. 2000. Performance of a 2D Image-Based Anthropometric Measurement and Clothing Sizing System. Applied Ergonomics 5: 445-451.

Moore-Jansen PH, Jantz RL. 1989. Craniometric Analysis of a Nineteenth Century Afro-American Skeletal Population. American Journal of Physical Anthropology 78(2): 275.

Moser RP, Wagner GN. 1989. Nutrient Groove of the Ilium, A Subtle but Important Forensic Radiographic Marker in the Identification of Victims of Severe Trauma. Skeletal Radiology 19: 15-19.

Mueller, W.H., and R. Martorell. 1988. Reliability and Accuracy of Measurement. In Lohman TG, Roche F, Martorel R editors. Anthropometric Standardization Reference Manual. Champaign, Ill.: Human Kinetics Books, p 8-86.

Muren C, Ytterbergh C. 1986. Computed Tomography of Temporal Bone Specimens. A Test of the Resolution Capacity. Acta Radiologica: Diagnosis 27(6): 645-651.

Nager GT, Nager M. 1953. The Arteries of the Middle Ear with Particular Regard to the Blood Supply of the Auditory Ossicles. Annals of Otology, Rhinology and Laryngology 62(4): 923-949.

Noren A, Lynnerup N, Czarnetzki A, Graw M. 2005. Lateral Angle: A Method of Sexing Using the Petrous Bone. American Journal of Physical Anthropology 128(2): 318-323.

Owsley DW, Mann RW. 1989. Positive Identification Based on Radiographic Examination of the Leg and Foot. A Case Report. Journal of the American Podiatric Medical Association 79(10): 511-513.

Owsley DW, Mann RW. 1992. Positive Personal Identity of Skeletonized Remains Using Abdominal and Pelvic Radiographs. Journal of Forensic Anthropology 37: 332-336.

Paprocki A, Biskup B, Kozlowska K, Kuniszyk A, Bien D, Niemczyk K. 2004. The Topographical Anatomy of the Round Window and Related Structures for the Purpose of Cochlear Implant Surgery. Folia Morphologica 63(3): 309-312.

Popper AN, Fay RR. 1997. Evolution of the Ear and Hearing: Issues and Questions. Brain, Behavior, and Evolution 50: 213-221.

Portmann M, Doutremepuich C, Bebear JP, Vazel P. 1975. Further Data on the Study of Meniere's Disease and Menieriform Syndromes. Review of Laryngology Otology and Rhinology 96(5): 281-291

Quatrehomme GP, Fronty A. 1996. Identification by Frontal Sinus Pattern in Forensic Anthropology. Forensic Science International 83(2): 147-153.

Rak Y. 1978. The Functional Significance of the Squamosal Suture in *Australopithecus Boisei*. American Journal of Physical Anthropology 49(1): 71-78.

Reichs KJ. 1993. Quantified Comparison of Frontal Sinus Patterns by Means of Computed Tomography. Forensic Science International 61: 141-168.

Reichs KJ, Dorion JD. 1992. The Use of Computed Tomography (CT) Scans in the Comparison of Frontal Sinus Configurations. Canadian Society of Forensic Sciences Journal 25: 10-16.

Reipert TD, Ulmcke D. 2001. Identification of Unknown Dead Bodies by X-ray Image Comparison of the Skull using the X-ray Simulation Program FoXSIS. Forensic Science International 117: 89-98.

Rhine S, Sperry K. 1991. Radiographic Identification by Mastoid Sinus and Arterial Pattern. Journal of Forensic Sciences 36(1): 272-279.

Rho JY, Feng Z, Ziv I. 1995. Qualitative Assessment of Femoral Stem Fit and Fill Using Computed Tomography and Image Processing. Proceedings of the American Society of Mechanical Engineering 29: 557-558.

Richardson ML, Van Vu M, Vincent LM, Sanborzan BJ, Benirshke SK. 1993. CT Measurement of the Calcaneal Varus Angle in the Normal and Fractured Foot. Journal of Computer Assisted Tomography 16: 261-264.

Richtsmeier JT, Paik CK, Elfert PC, Cole II TM, Dahlman HR. 1995. Precision, Repeatability, and Validation of the Localization of Cranial Landmarks Using Computed Tomography Scans. The Cleft Palate-Craniofacial Journal 32: 217-227.

Robertson B, Vignaux GA. 1995. DNA Evidence: Wrong Answers or Wrong Questions? Genetica 96(1): 145-152.

Romer AS. 1967. The Vertebrate Story. Chicago: University of Chicago Press.

Romer AS, Parsons TS. 1977. The Vertebrate Body. Philadelphia: W.B. Saunders Company.

Rubin PJ, Leyvraz PF, Aubaniac JM, Argenson JN, Esteve P, de Roguin B. 1992. The Morphology of the Proximal Femur. A Three Dimensional Radiographic Analysis. Journal of Bone and Joint Surgery, Britain 74(1): 28-32.

Ruff CB. 1980. Age Differences in Craniofacial Dimensions Among Adults from Indian Knoll, Kentucky. American Journal of Physical Anthropology 53: 101-108.

Sakashita T, Sando I. 1994. Postnatal Development of the Internal Auditory Canal Studied by Computer-Aided Three-Dimensional reconstruction and Measurement. The Annals of Otology, Rhinology, and Laryngology

Saks MJ. Koehler M. 2005. The Coming Paradigm Shift in Forensic Identification Science. Science 309: 892-895.

Scheuer L. Black S. 2000. Developmental Juvenile Osteology. London: Academic Press: p 63-84.

Schwartz A. 2006. Diagnostic Test Calculator, Version 2006032401 [Internet]. PennMush; 2006 [cited 2006 Mar 30]. Available from: http://www.pennmush.org/cgi-bin/testcalc.pl

Schwartz JH, TattersalI. 1996. Toward Distinguishing *Homo neanderthalensis* from *Homo sapiens* and vice versa. Anthropologie 34: 79-88.

Schaffer KA, Haughton VM, Wilson CR. 1980. High Resolution Computed Tomography of the Temporal Bone. Radiology 134: 409-414.

Schulter FP. 1976. A Comparative Study of the Temporal Bone in Three Populations of Man. American Journal of Physical Anthropology 44: 453-468.

Schulter-Ellis FP. 1979. Population Differences in Cellularity of the Mastoid Process. Acta Oto-Laryngologica 87: 461-465.

Seibert CE, Barnes JE, Dreisbach JN, Swanson WB, Heck RJ. 1981. Accurate CT Measurement of the Spinal Cord Using Metrizamide: Physical Factors. American Journal of Roentgenology 136(4): 777-80.

Sherwood RJ. 1999. Pneumatic Processes in the Temporal Bone of the Chimpanzee (*Pan troglodytes*) and gorilla (*Gorilla gorilla*). Journal of Morphology 241:127-137.

Sherwood RJ, Ward SC, Hill A. 2002. The Taxonomic Status of the Chemeron Temporal Bone(KNM-BC 1). Journal of Human Evolution 42:153-184.

Shipman P, Walker A, Bichell D. 1985. The Human Skeleton. Boston: Harvard University Press.

Simmons T. 2006. Appropriate Procedures, Applications and Ethics. Proceedings of the American Academy of Forensic Sciences Annual Meeting, Seattle, WA: 303.

Simms DL, Neely JF. 1989. Growth of the Lateral Surface of the Temporal Bone in Children. Laryngoscope 99: 795-799.

Spoor CF. 1993. The Comparative Morphology and Phylogeny of the Human Bony Labyrinth. PhD dissertation, University of Utrecht.

Spoor CF, Wood B, Zonnefeld F. 1994. Implications of Early Hominid Labyrinthine Morphology for the Evolution of Human Bipedal Locomotion. Nature 369: 645-648.

Spoor F. Zonnefeld F. 1998. Comparative Review of the Human Bony Labyrinth. Yearbook of Physical Anthropology 41: 211-251.

Steadman DW, Adams BJ, Konigsberg LW. 2006. Statistical Basis for Positive Identification in Forensic Anthropology. American Journal of Physical Anthropology [Internet]. [cited 2006 Mar 1]. Available from: http://www3.interscience.wiley.com/cgi-bin/abstract/112438240/abstract

Steele DG, Bramblett C. 1988. Anatomy and Biology of the Human Skeleton. College Station, Texas: Texas A&M University Press.

Strait DS, Grine FE, Moniz MA. 1997. A Reappraisal of Early Hominid Phylogeny. Journal of Human Evolution 32: 17-82.

Stringer CB. 1984. Definition of *Homo erectus* and the Existence of the Species in Africa and Europe: In Andrews P, Franzen J editors. The Early Evolution of Man with Special Emphasis on Southeast Asia and Africa. Courier. Forschungsinstitut Senckenberg 69:131-143.

Sumner DR, Olson CL, Freeman PM, Lobick JJ, Andriacchi TP. 1988. Computed Tomographic Measurement of Cortical Geometry. Journal of Biomechanics 22: 649-653.

Taylor S. 1982. The Petrous Temporal Bone (Including the Cerebellopontine Angle). Radiologic Clinics of North America 20(1): 67-86.

Tekdemir I, Tuccar E. 1998. The Jugular Foramen: A Comparative Radioanatomic Study. Neurology 50: 557-562.

Tobias PV. 1967. Olduvai Gorge: The Cranium and Maxillary Dentition of Australopithecus Boisei. Volume II. London: Cambridge University Press.

Tobias PV. 1991. Olduvai Gorge: The Skulls, Endocasts, and Teeth of *Homo habilis*. Volume IV. London: Cambridge University Press.

Toth M, Alpar A, Patonay L, Otah I. 2006. Developmental and Surgical Anatomy of the Round Window. Annals of Anatomy 188(2): 93-101.

Turner A, Porter WA. 1922. The Structural Type of the Mastoid Process Based on the Skiagraphic Examination of 1000 Crania of Various Races of Mankind. Journal of Laryngology 37: 115-121.

Ubelaker DH. 1984. Positive identification from the radiographic comparison of frontal sinus patterns. In Rathbun TA, Buikstra JE, editors. Case Studies in Forensic Anthropology. Springfield: C.C. Thomas.

Ulijaszek SJ, Kerr DA. 1999. Anthropometric Measurement Error and the Assessment of Nutritional Status. British Journal of Nutrition 82(3): 165-177.

United States of America v. Carlos Ivan Lleva Plaza, Wilfredo Martinez Acosta, and Victor Rodriguez CR. NO. 98-362-10, 11, 12 2002.

Virapongse C, Rothman SLG, Kier EL, Sarwar M. 1982. Computed Tomographic Anatomy of the Temporal Bone. American Journal of Neuroradiology 3: 379-389.

Waitzman AA, Posnick JC, Armstrong MB, Pron GE. 1992. Craniofacial Measurements Based on Computed Tomography: Part I. Accuracy and Reproducibility. The Cleft Palate-Craniofacial Journal 29:112-117.

Waldron T. 1987. The Relative Survival of The Human Skeleton: Implications for Paleopathology. In Boddington A, Garland AN, Janaway RC editors. Death, Decay and Reconstruction: Approaches to Archaeology and Forensic Science. Manchester: Manchester University Press, p 55-64.

Wayman J, Jain A, Maltoni D, Maio D. 2005. Biometric Systems: Technology, Design and Performance Evaluation. London: Springer-Verlag.

Webb WR, Gamsu G, Wall S, Cann CE, Proctor E. 1984. CT of a bronchial phantom. Factors Affecting Appearance and Size Measurements. Investigative Radiology 19(5): 394-398.

Webster DB, Fay RR, Popper AN. 1992. Evolutionary Biology of Hearing, New York: Springer-Verlag.

Weidenreich F. 1948. About the Morphological Character of the Australopithecine Skull. Cape Town, South Africa: Royal Society of South Africa, p 153-158.

Weschlet J, Phillips J, Bruse V, Soulie F, Hauhg. 1998. Face Recognition: From Theory to Application. Berlin: Springer-Verlag.

Weng JJ, Swets M. 1999. Face Recognition. In Biometrics: Personal Identification in a Networked Society. New York: Kluwer Academic Publishers.

Wescott D, Moore-Jansen P. 2001. Metric Variation in the Human Occipital Bone: Forensic Anthropological Applications. Journal of Forensic Sciences 46(5): 1159-1163.

White TD. 1991. Human Osteology. San Diego, California: Academic Press.

White TD, Johanson DC, Kimbel WH. 1981. *Australopithecus africanus*: Its Phylogenetic Position Reconsidered. South African Journal of Science 77: 445-470.

Wilbrand HF. 1984. The Vestibular and Cochlear Aqueducts. Review of Laryngology, Otology, and Rhinology 105(2): 101-109.

Winkler E-M, Kirchengast S. 1993. Metric Characters of the Hard Palate and their Cephalometric Correlations in Namibian !Kung San and Kenyan tribes. Human Biology 65: 139-150.

Yoshino M, Miyasaka H. 1987. Classification System of Frontal Sinus Patterns by Radiography: Its Application to the Identification of Unknown Skeletal Remains. Forensic Science International 22: 289-299.

Yoshino M, Miyasaka H. 1989. Classification System of Frontal Sinus Patterns. Canadian Society of Forensic Sciences Journal 22: 135-146.

Zuckerman S. 1955. Age Changes in the Basicranial Axis of the Human Skull. American Journal of Physical Anthropology 13: 521-539.

APPENDIX I

TABLE A-I. COMPLETE MEASUREMENT SET BEFORE REPEATABILITY TESTS

Measurement Set			
LSC-MPSC	CLSC-PIAC	STYL-PIE	VAE-PIE
LSC-LPSC	CLSC-AIE	STYL-AEAM	VAE-AEAM
LSC-CLSC	CLSC-PIE	STYL-PEAM	VAE-PEAM
LSC-VBLE	CLSC-AEAM	STYL-APIAC	VAE-APIAC
LSC-COCH	CLSC-PEAM	STYL-PPIAC	VAE-PPIAC
LSC-MID	CLSC-APIAC	STYL-APSEM	VAE-APSEM
LSC-STYM	CLSC-PPIAC	STYL-PPSEM	VAE-PPSEM
LSC-OVAL	CLSC-APSEM	STYL-LIAC	VAE-LIAC
LSC-CAR	CLSC-PPSEM	STYL-MIAC	VAE-MIAC
LSC-JUG	CLSC-LIAC	STYL-PAPE	VAE-PAPE
LSC-SPIN	CLSC-MIAC	STYL-LAT	VAE-LAT
LSC-SIG	CLSC-PAPE	STYL-SPIPRO	VAE-SPIPRO
LSC-AUR	CLSC-LAT	OVAL-CAR	AIAC-PIAC
LSC-BAS	CLSC-SPIPRO	OVAL-JUG	AIAC-AIE
LSC-VAE	VBLE-COCH	OVAL-SPIN	AIAC-PIE
LSC-AIAC	VBLE-MID	OVAL-SIG	AIAC-AEAM
LSC-PIAC	VBLE-STYL	OVAL-AUR	AIAC-PEAM
LSC-AIE	VBLE-OVAL	OVAL-BAS	AIAC-APIAC
LSC-PIE	VBLE-CAR	OVAL-VAE	AAIC-PPIAC
LSC-AEAM	VBLE-JUG	OVAL-AIAC	AIAC-APSEM
LSC-PEAM	VBLE-SPIN	OVAL-PIAC	AIAC-PPSEM
LSC-APIAC	VBLE-SIG	OVAL-AIE	AIAC-LIAC
LSC-PPIAC	VBLE-AUR	OVAL-PIE	AIAC-MIAC
LSC-APSEM	VBLE-BAS	OVAL-AEAM	AIAC-PAPE
LSC-PPSEM	VBLE-VAE	OVAL-PEAM	AIAC-LAT
LSC-LIAC	VBLE-AIAC	OVAL-APIAC	AIAC-SPIPRO
LSC-MIAC	VBLE-PIAC	OVAL-PPIAC	PIAC-AIE
LSC-PAPE	VBLE-AIE	OVAL-APSEM	PIAC-PIE
LSC-LAT	VBLE-PIE	OVAL-PPSEM	PIAC-AEAM
LSC-SPIPRO	VBLE-AEAM	OVAL-LIAC	PIAC-PEAM
MPSC-LPSC	VBLE-PEAM	OVAL-MIAC	PIAC-APIAC
MPSC-CLSC	VBLE-APIAC	OVAL-PAPE	PIAC-PPIAC
MPSC-VBLE	VBLE-PPIAC	OVAL-LAT	PIAC-APSEM
MPSC-COCH	VBLE-APSEM	OVAL-SPIPRO	PIAC-PPSEM
MPSC-MID	VBLE-PPSEM	CARO-JUG	PIAC-LIAC
MPSC-STYL	VBLE-LIAC	CARO-SPIN	PIAC-MIAC

Table A-I (Continued)

Measurement Set			
MPSC-OVAL	VBLE-MIAC	CARO-SIG	PIAC-PAPE
MPSC-CAR	VBLE-PAPE	CARO-AUR	PIAC-LAT
MPSC-JUG	VBLE-LAT	CARO-BAS	PIAC-SPIPRO
MPSC-SPIN	VBLE-SPIPRO	CARO-VAE	AIE-PIE
MPSC-SIG	COCH-MID	CARO-AIAC	AIE-AEAM
MPSC-AUR	COCH-STYL	CARO-PIAC	AIE-PEAM
MPSC-BAS	COCH-OVAL	CARO-AIE	AIE-APIAC
MPSC-VAE	COCH-CAR	CARO-PIE	AIE-PPIAC
MPSC-AIAC	COCH-JUG	CARO-AEAM	AIE-APSEM
MPSC-PIAC	COCH-SPIN	CARO-PEAM	AIE-PPSEM
MPSC-AIE	COCH-SIG	CARO-APIAC	AIE-LIAC
MPSC-PIE	COCH-AUR	CARO-PPIAC	AIE-MIAC
MPSC-AEAM	COCH-BAS	CARO-APSEM	AIE-PAPE
MPSC-PEAM	COCH-VAE	CARO-PPSEM	AIE-LAT
MPSC-APIAC	COCH-AIAC	CARO-LIAC	AIE-SPIPRO
MPSC-PPIAC	COCH-PIAC	CARO-MIAC	PIE-AEAM
MPSC-APSEM	COCH-AIE	CARO-PAPE	PIE-PEAM
MPSC-PPSEM	COCH-PIE	CARO-LAT	PIE-APIAC
MPSC-LIAC	COCH-AEAM	CARO-SPIPRO	PIE-PPIAC
MPSC-MIAC	COCH-PEAM	JUG-SPIN	PIE-APSEM
MPSC-PAPE	COCH-APIAC	JUG-SIG	PIE-PPSEM
MPSC-LAT	COCH-PPIAC	JUG-AUR	PIE-LIAC
MPSC-SPIPRO	COCH-APSEM	JUG-BAS	PIE-MIAC
LPSC-CLSC	COCH-PPSEM	JUG-VAE	PIE-PAPE
LPSC-VBLE	COCH-LIAC	JUG-AIAC	PIE-LAT
LPSC-COCH	COCH-MIAC	JUG-PIAC	PIE-SPIPRO
LPSC-MID	COCH-PAPE	JUG-AIE	AEAM-PEAM
LPSC-STYL	COCH-LAT	JUG-PIE	AEAM-APIAC
LPSC-OVAL	COCH-SPIPRO	JUG-AEAM	AEAM-PPIAC
LPSC-CAR	MID-STYL	JUG-PEAM	AEAM-APSEM
LPSC-JUG	MID-OVAL	JUG-APIAC	AEAM-PPSEM
LPSC-SPIN	MID-CAR	SIG-AIE	AEAM-LIAC
LPSC-SIG	MID-JUG	SIG-PIE	AEAM-MIAC
LPSC-AUR	MID-SPIN	SIG-AEAM	AEAM-PAPE
LPSC-BAS	MID-SIG	SIG-PEAM	AEAM-LAT
LPSC-VAE	MID-AUR	SIG-APIAC	AEAM-SPIPRO
LPSC-AIAC	MID-BAS	SIG-PPIAC	PEAM-APIAC
LPSC-PIAC	MID-VAE	SIG-APSEM	PEAM-PPIAC
LPSC-AIE	MID-AIAC	SIG-PPSEM	PEAM-APSEM
LPSC-PIE	MID-PIAC	SIG-LIAC	PEAM-PPSEM

Table A-I (Continued)

Measurement Set			
LPSC-AEAM	MID-AIE	SIG-MIAC	PEAM-LIAC
LPSC-PEAM	MID-PIE	SIG-PAPE	PEAM-MIAC
LPSC-APIAC	MID-AEAM	SIG-LAT	PEAM-PAPE
LPSC-PPIAC	MID-PEAM	SIG-SPIPRO	PEAM-LAT
LPSC-APSEM	MID-APIAC	AUR-BAS	PEAM-SPIPRO
LPSC-PPSEM	MID-PPIAC	AUR-VAE	APIAC-PPIAC
LPSC-LIAC	MID-APSEM	AUR-AIAC	APIAC-APSEM
LPSC-MIAC	MID-PPSEM	AUR-PIAC	APIAC-PPSEM
LPSC-PAPE	JUG-PPIAC	AUR-AIE	APIAC-LIAC
LPSC-LAT	JUG-APSEM	AUR-PIE	APIAC-MIAC
LPSC-SPIPRO	JUG-PPSEM	AUR-AEAM	APIAC-PAPE
CLSC-VBLE	JUG-LIAC	AUR-PEAM	APIAC-LAT
CLSC-COCH	JUG-MIAC	AUR-APIAC	APIAC-SPIPRO
CLSC-MID	JUG-PAPE	AUR-PPIAC	PPIAC-APSEM
CLSC-STYL	JUG-LAT	AUR-APSEM	PPIAC-PPSEM
CLSC-OVAL	JUG-SPIPRO	AUR-PPSEM	PPIAC-LIAC
CLSC-CAR	SPIN-SIG	AUR-LIAC	PPIAC-MIAC
CLSC-JUG	SPIN-AUR	AUR-MIAC	PPIAC-PAPE
CLSC-SPIN	SPIN-BAS	AUR-PAPE	PPIAC-LAT
CLSC-SIG	SPIN-VAE	AUR-LAT	PPIAC-SPIPRO
CLSC-AUR	SPIN-AIAC	AUR-SPIPRO	APSEM-PPSEM
CLSC-BAS	SPIN-PIAC	BAS-VAE	APSEM-LIAC
CLSC-VAE	SPIN-AIE	BAS-AIAC	APSEM-MIAC
CLSC-AIAC	SPIN-PIE	BAS-PIAC	APSEM-PAPE
MID-LIAC	SPIN-AEAM	BAS-AIE	APSEM-LAT
MID-MIAC	SPIN-PEAM	BAS-PIE	APSEM-SPIPRO
MID-PAPE	SPIN-APIAC	BAS-AEAM	PPSEM-LIAC
MID-LAT	SPIN-PPIAC	BAS-PEAM	PPSEM-MIAC
MID-SPIPRO	SPIN-APSEM	BAS-APIAC	PPSEM-PAPE
STYL-OVAL	SPIN-PPSEM	BAS-PPIAC	PPSEM-LAT
STYL-CAR	SPIN-LIAC	BAS-APSEM	PPSEM-SPIPRO
STYL-JUG	SPIN-MIAC	BAS-PPSEM	LIAC-MIAC
STYL-SPIN	SPIN-PAPE	BAS-LIAC	LIAC-PAPE
STYL-SIG	SPIN-LAT	BAS-MIAC	LIAC-LAT
STYL-AUR	SPIN-SPIPRO	BAS-PAPE	LIAC-SPIPRO
STYL-BAS	SIG-AUR	BAS-LAT	MIAC-PAPE
STYL-VAE	SIG-BAS	BAS-SPIPRO	MIAC-LAT
STYL-AIAC	SIG-VAE	VAE-AIAC	MIAC-SPIPRO
STYL-PIAC	SIG-AIAC	VAE-PIAC	PAPE-LAT
STYL-AIE	SIG-PIAC	VAE-AIE	PAPE-SPIPRO

APPENDIX II

TABLE A-II. TECHNICAL ERROR OF MEASUREMENT (TEM) AND RELIABILITY COEFFICIENTS (R) FOR EACH MEASUREMENT

Measurement	TEM	R	Measurement	TEM	R
LSC-MPSC	0.7684	0.97	OVAL-SPIPRO	0.2474	0.98
LSC-LPSC	0.7720	0.98	CARO-JUG	0.0479	0.99
LSC-CLSC	1.1489	0.95	CARO-SPIN	0.0104	0.97
LSC-VBLE	1.1325	0.96	CARO-SIG	0.0570	0.99
LSC-COCH	1.0446	0.95	CARO-AUR	0.0538	0.97
LSC-MID	0.2167	0.99	CARO-BAS	0.0234	0.99
LSC-STYM	0.1761	0.98	CARO-VAE	0.9741	0.95
LSC-OVAL	0.1751	0.97	CARO-AIAC	0.9778	0.95
LSC-CAR	0.0027	0.99	CARO-PIAC	1.0053	0.95
LSC-JUG	0.0164	0.99	CARO-AIE	0.9578	0.96
LSC-SPIN	0.0331	0.99	CARO-PIE	0.5692	0.97
LSC-SIG	0.1768	0.99	CARO-AEAM	0.7846	0.97
LSC-AUR	0.5790	0.97	CARO-PEAM	0.7703	0.96
LSC-BAS	1.1829	0.95	CARO-APIAC	0.7953	0.97
LSC-VAE	0.1934	0.96	CARO-PPIAC	1.0562	0.95
LSC-AIAC	0.6187	0.98	CARO-APSEM	0.4165	0.98
LSC-PIAC	0.0834	0.97	CARO-PPSEM	0.0292	0.99
LSC-AIE	0.1121	0.96	CARO-LIAC	0.0796	0.99
LSC-PIE	0.1039	0.97	CARO-MIAC	0.7837	0.97
LSC-AEAM	0.0073	0.99	CARO-PAPE	0.0092	0.99
LSC-PEAM	0.6575	0.97	CARO-LAT	0.5910	0.95
LSC-APIAC	0.3419	0.96	CARO-SPIPRO	0.9357	0.96
LSC-PPIAC	0.1309	0.97	JUG-SPIN	1.6302	0.95
LSC-APSEM	0.5409	0.98	JUG-SIG	0.4963	0.98
LSC-PPSEM	0.6794	0.97	JUG-AUR	1.1351	0.99
LSC-LIAC	1.2657	0.95	JUG-BAS	0.0949	0.99
LSC-MIAC	0.0138	0.99	JUG-VAE	0.1250	0.98
LSC-PAPE	0.1084	0.99	JUG-AIAC	0.0150	0.99
LSC-LAT	1.3263	0.96	JUG-PIAC	0.3904	0.97
LSC-SPIPRO	0.2369	0.97	JUG-AIE	0.3339	0.97
MPSC-LPSC	0.6474	0.97	JUG-PIE	0.8466	0.96
MPSC-CLSC	0.1056	0.96	JUG-AEAM	0.3138	0.98
MPSC-VBLE	1.8553	0.95	JUG-PEAM	0.0465	0.99
MPSC-COCH	0.6941	0.96	JUG-APIAC	0.8342	0.96
MPSC-MID	0.7653	0.97	JUG-PPIAC	0.6835	0.96

Table A-II (Continued)

Measurement	TEM	R	Measurement	TEM	R
MPSC-STYL	0.0648	0.98	JUG-APSEM	0.4168	0.98
MPSC-OVAL	0.7950	0.98	JUG-PPSEM	0.8265	0.96
MPSC-CAR	0.7919	0.97	JUG-LIAC	0.9490	0.96
MPSC-JUG	0.0056	0.99	JUG-MIAC	0.0086	0.99
MPSC-SPIN	0.0188	0.99	JUG-PAPE	0.4935	0.98
MPSC-SIG	0.1370	0.99	JUG-LAT	0.2369	0.97
MPSC-AUR	0.3651	0.97	JUG-SPIPRO	0.9336	0.95
MPSC-BAS	0.9944	0.96	SPIN-SIG	0.8959	0.96
MPSC-VAE	0.1232	0.97	SPIN-AUR	0.9815	0.96
MPSC-AIAC	0.2148	0.98	SPIN-BAS	0.4955	0.98
MPSC-PIAC	1.8282	0.95	SPIN-VAE	1.4086	0.95
MPSC-AIE	0.0990	0.99	SPIN-AIAC	1.0397	0.96
MPSC-PIE	0.0525	0.99	SPIN-PIAC	0.3875	0.98
MPSC-AEAM	0.0822	0.98	SPIN-AIE	0.2790	0.98
MPSC-PEAM	0.5289	0.97	SPIN-PIE	1.4117	0.96
MPSC-APIAC	0.3723	0.96	SPIN-AEAM	0.3371	0.98
MPSC-PPIAC	0.0073	0.98	SPIN-PEAM	0.0796	0.99
MPSC-APSEM	0.6867	0.97	SPIN-APIAC	0.2832	0.98
MPSC-PPSEM	0.0708	0.99	SPIN-PPIAC	0.1381	0.98
MPSC-LIAC	0.9082	0.97	SPIN-APSEM	0.0381	0.99
MPSC-MIAC	0.0207	0.96	SPIN-PPSEM	0.9588	0.96
MPSC-PAPE	0.7288	0.97	SPIN-LIAC	1.0450	0.95
MPSC-LAT	0.0039	0.99	SPIN-MIAC	0.0130	0.99
MPSC-SPIPRO	0.0851	0.97	SPIN-PAPE	0.1863	0.99
LPSC-CLSC	0.5427	0.96	SPIN-LAT	0.9151	0.95
LPSC-VBLE	0.7802	0.98	SPIN-SPIPRO	0.8837	0.95
LPSC-COCH	0.3186	0.98	SIG-AUR	0.6295	0.97
LPSC-MID	0.1160	0.98	SIG-BAS	0.6525	0.97
LPSC-STYL	0.0254	0.97	SIG-VAE	1.9456	0.95
LPSC-OVAL	0.1042	0.99	SIG-AIAC	0.1580	0.98
LPSC-CAR	0.6333	0.96	SIG-PIAC	0.2863	0.98
LPSC-JUG	0.9557	0.95	SIG-AIE	0.9531	0.96
LPSC-SPIN	0.0078	0.98	SIG-PIE	0.6158	0.96
LPSC-SIG	0.0062	0.99	SIG-AEAM	0.6297	0.97
LPSC-AUR	0.5860	0.97	SIG-PEAM	0.2013	0.97
LPSC-BAS	1.1874	0.95	SIG-APIAC	0.2061	0.97
LPSC-VAE	0.7872	0.97	SIG-PPIAC	0.4435	0.98
LPSC-AIAC	0.6604	0.98	SIG-APSEM	0.5117	0.98
LPSC-PIAC	0.1720	0.99	SIG-PPSEM	0.8421	0.96
LPSC-AIE	0.0821	0.99	SIG-LIAC	0.8970	0.96

Table A-II (Continued)

Measurement	TEM	R	Measurement	TEM	R
LPSC-PIE	0.8455	0.95	SIG-MIAC	0.9255	0.96
LPSC-AEAM	1.0349	0.95	SIG-PAPE	0.0358	0.99
LPSC-PEAM	0.7433	0.96	SIG-LAT	0.0898	0.99
LPSC-APIAC	0.1995	0.98	SIG-SPIPRO	0.1399	0.99
LPSC-PPIAC	0.2279	0.98	AUR-BAS	1.8354	0.95
LPSC-APSEM	0.5737	0.96	AUR-VAE	0.6359	0.98
LPSC-PPSEM	0.2700	0.97	AUR-AIAC	0.6589	0.98
LPSC-LIAC	0.5363	0.98	AUR-PIAC	0.5860	0.97
LPSC-MIAC	0.0207	0.99	AUR-AIE	0.8048	0.96
LPSC-PAPE	1.0137	0.95	AUR-PIE	0.5579	0.98
LPSC-LAT	0.5461	0.96	AUR-AEAM	0.8935	0.96
LPSC-SPIPRO	0.2211	0.97	AUR-PEAM	0.9414	0.96
CLSC-VBLE	0.3057	0.98	AUR-APIAC	0.1864	0.99
CLSC-COCH	0.4126	0.98	AUR-PPIAC	0.0494	0.99
CLSC-MID	0.0191	0.97	AUR-APSEM	0.2045	0.98
CLSC-STYL	0.0404	0.99	AUR-PPSEM	0.9511	0.99
CLSC-OVAL	0.5445	0.98	AUR-LIAC	0.0567	0.96
CLSC-CAR	1.6922	0.95	AUR-MIAC	0.8181	0.98
CLSC-JUG	0.3921	0.97	AUR-PAPE	0.5193	0.97
CLSC-SPIN	0.9057	0.96	AUR-LAT	0.9311	0.96
CLSC-SIG	0.5742	0.96	AUR-SPIPRO	0.9710	0.95
CLSC-AUR	0.1321	0.97	BAS-VAE	0.6035	0.97
CLSC-BAS	1.5881	0.95	BAS-AIAC	0.6178	0.98
CLSC-VAE	0.1568	0.99	BAS-PIAC	0.1009	0.99
CLSC-AIAC	0.0710	0.98	BAS-AIE	0.0662	0.99
CLSC-AIAC	0.4530	0.97	BAS-PIE	0.0343	0.98
CLSC-AIE	0.5754	0.98	BAS-AEAM	0.0265	0.99
CLSC-PIE	0.1491	0.99	BAS-PEAM	0.2674	0.98
CLSC-AEAM	1.9757	0.96	BAS-APIAC	0.0523	0.99
CLSC-PEAM	0.0013	0.96	BAS-PPIAC	0.1835	0.98
CLSC-APIAC	1.0107	0.95	BAS-APSEM	0.0483	0.98
CLSC-PPIAC	0.3529	0.98	BAS-PPSEM	0.4356	0.97
CLSC-APSEM	0.0726	0.99	BAS-LIAC	0.6743	0.97
CLSC-PPSEM	0.6830	0.97	BAS-MIAC	0.8007	0.96
CLSC-LIAC	0.5847	0.97	BAS-PAPE	1.9651	0.95
CLSC-MIAC	0.3125	0.98	BAS-LAT	0.7668	0.96
CLSC-PAPE	0.7106	0.98	BAS-SPIPRO	0.3417	0.98
CLSC-LAT	0.9820	0.95	VAE-AIAC	0.7727	0.98
CLSC-SPIPRO	0.9917	0.95	VAE-PIAC	0.4182	0.97
VBLE-COCH	0.8602	0.96	VAE-AIE	0.8067	0.96

Table A-II (Continued)

Measurement	TEM	R	Measurement	TEM	R
VBLE-MID	0.9922	0.96	VAE-PIE	0.8670	0.96
VBLE-STYL	0.8784	0.95	VAE-AEAM	0.5461	0.97
VBLE-OVAL	0.7469	0.97	VAE-PEAM	0.8574	0.98
VBLE-CAR	0.5082	0.97	VAE-APIAC	0.8765	0.98
VBLE-JUG	0.9677	0.95	VAE-PPIAC	0.7064	0.98
VBLE-SPIN	0.5163	0.96	VAE-APSEM	1.9782	0.96
VBLE-SIG	0.0640	0.99	VAE-PPSEM	0.9401	0.96
VBLE-AUR	0.0131	0.99	VAE-LIAC	2.0229	0.95
VBLE-BAS	0.0952	0.99	VAE-MIAC	0.0821	0.99
VBLE-VAE	0.0441	0.99	VAE-PAPE	0.0035	0.99
VBLE-AIAC	0.0788	0.99	VAE-LAT	0.3685	0.97
VBLE-PIAC	0.3036	0.98	VAE-SPIPRO	0.6439	0.98
VBLE-AIE	0.1821	0.99	AIAC-PIAC	0.3160	0.98
VBLE-PIE	0.2947	0.98	AIAC-AIE	0.9178	0.95
VBLE-AEAM	0.7972	0.97	AIAC-PIE	1.0582	0.95
VBLE-PEAM	0.1742	0.98	AIAC-AEAM	1.0202	0.96
VBLE-APIAC	0.1476	0.98	AIAC-PEAM	0.8811	0.96
VBLE-PPIAC	0.6375	0.98	AIAC-APIAC	0.5116	0.97
VBLE-APSEM	0.2653	0.98	AAIC-PPIAC	0.6052	0.97
VBLE-PPSEM	0.3847	0.98	AIAC-APSEM	0.1049	0.98
VBLE-LIAC	0.0969	0.99	AIAC-PPSEM	0.0525	0.98
VBLE-MIAC	0.4630	0.97	AIAC-LIAC	0.0074	0.99
VBLE-PAPE	0.9523	0.95	AIAC-MIAC	0.0184	0.99
VBLE-LAT	1.3968	0.95	AIAC-PAPE	0.9841	0.96
VBLE-SPIPRO	1.6518	0.95	AIAC-LAT	0.5208	0.98
COCH-MID	1.2929	0.95	AIAC-SPIPRO	0.0057	0.99
COCH-STYL	0.8877	0.95	PIAC-AIE	0.0384	0.99
COCH-OVAL	0.1077	0.99	PIAC-PIE	0.1686	0.98
COCH-CAR	0.0279	0.99	PIAC-AEAM	0.2623	0.98
COCH-JUG	0.9474	0.98	PIAC-PEAM	0.1616	0.98
COCH-SPIN	0.9140	0.95	PIAC-APIAC	0.0964	0.99
COCH-SIG	0.4146	0.97	PIAC-PPIAC	0.0487	0.99
COCH-AUR	0.8881	0.96	PIAC-APSEM	0.1687	0.98
COCH-BAS	0.5246	0.96	PIAC-PPSEM	0.1086	0.98
COCH-VAE	1.5029	0.95	PIAC-LIAC	0.3571	0.97
COCH-AIAC	0.9518	0.96	PIAC-MIAC	0.6873	0.98
COCH-PIAC	0.8173	0.97	PIAC-PAPE	1.5078	0.95
COCH-AIE	0.3078	0.98	PIAC-LAT	0.0165	0.99
COCH-PIE	0.9848	0.96	PIAC-SPIPRO	0.8286	0.95
COCH-AEAM	0.1095	0.98	AIE-PIE	1.6663	0.95

Table A-II (Continued)

Measurement	TEM	R	Measurement	TEM	R
COCH-PEAM	0.4525	0.97	AIE-AEAM	0.1479	0.98
COCH-APIAC	0.8789	0.96	AIE-PEAM	0.2043	0.98
COCH-PPIAC	0.5564	0.97	AIE-APIAC	0.6429	0.97
COCH-APSEM	0.1697	0.98	AIE-PPIAC	0.5759	0.97
COCH-PPSEM	0.2015	0.98	AIE-APSEM	0.0926	0.98
COCH-LIAC	0.2298	0.98	AIE-PPSEM	1.1282	0.95
COCH-MIAC	0.9176	0.95	AIE-LIAC	0.0443	0.99
COCH-PAPE	0.0885	0.99	AIE-MIAC	0.0625	0.99
COCH-LAT	0.1444	0.99	AIE-PAPE	0.9364	0.96
COCH-SPIPRO	1.6821	0.95	AIE-LAT	0.9016	0.96
MID-STYL	0.1771	0.98	AIE-SPIPRO	1.2011	0.95
MID-OVAL	0.5758	0.97	PIE-AEAM	0.0706	0.98
MID-CAR	0.1648	0.98	PIE-PEAM	0.0942	0.98
MID-JUG	0.0623	0.99	PIE-APIAC	0.5096	0.97
MID-SPIN	0.8780	0.95	PIE-PPIAC	0.8431	0.96
MID-SIG	0.1115	0.98	PIE-APSEM	0.6554	0.97
MID-AUR	0.4249	0.97	PIE-PPSEM	0.6099	0.98
MID-BAS	0.2304	0.97	PIE-LIAC	0.0327	0.99
MID-VAE	0.7465	0.96	PIE-MIAC	0.0906	0.99
MID-AIAC	0.9689	0.95	PIE-PAPE	0.5439	0.97
MID-PIAC	0.9523	0.95	PIE-LAT	1.2357	0.96
MID-AIE	0.6258	0.98	PIE-SPIPRO	0.9014	0.96
MID-PIE	0.2142	0.98	AEAM-PEAM	0.2509	0.97
MID-AEAM	0.4098	0.97	AEAM-APIAC	0.5402	0.97
MID-PEAM	0.4622	0.97	AEAM-PPIAC	0.7063	0.97
MID-APIAC	0.0033	0.99	AEAM-APSEM	0.6257	0.97
MID-PPIAC	0.1097	0.98	AEAM-PPSEM	0.0317	0.99
MID-APSEM	0.4822	0.98	AEAM-LIAC	0.1086	0.99
MID-PPSEM	0.8539	0.96	AEAM-MIAC	0.1735	0.98
MID-LIAC	0.2897	0.98	AEAM-PAPE	0.7903	0.95
MID-MIAC	0.4636	0.97	AEAM-LAT	0.8317	0.96
MID-PAPE	0.4951	0.97	AEAM-SPIPRO	0.9489	0.96
MID-LAT	0.1125	0.98	PEAM-APIAC	0.9964	0.95
MID-SPIPRO	0.9125	0.96	PEAM-PPIAC	0.4773	0.97
STYL-OVAL	0.7360	0.97	PEAM-APSEM	0.0605	0.98
STYL-CAR	0.8846	0.97	PEAM-PPSEM	0.5126	0.97
STYL-JUG	0.9657	0.96	PEAM-LIAC	0.2204	0.96
STYL-SPIN	0.7214	0.98	PEAM-MIAC	0.1390	0.96
STYL-SIG	0.0314	0.99	PEAM-PAPE	0.9368	0.95
STYL-AUR	1.0960	0.96	PEAM-LAT	0.2347	0.98

Table A-II (Continued)

Measurement	TEM	R	Measurement	TEM	R
STYL-BAS	0.9318	0.96	PEAM-SPIPRO	0.8345	0.97
STYL-VAE	0.8392	0.98	APIAC-PPIAC	1.4849	0.95
STYL-AIAC	0.0848	0.98	APIAC-APSEM	0.2083	0.97
STYL-PIAC	0.8144	0.96	APIAC-PPSEM	1.4726	0.95
STYL-AIE	0.0206	0.99	APIAC-LIAC	0.2727	0.98
STYL-PIE	0.1500	0.98	APIAC-MIAC	0.9473	0.95
STYL-AEAM	0.0564	0.99	APIAC-PAPE	1.4687	0.96
STYL-PEAM	0.0791	0.99	APIAC-LAT	0.1329	0.99
STYL-APIAC	0.0225	0.99	APIAC-SPIPRO	0.0885	0.99
STYL-PPIAC	0.2551	0.97	PPIAC-APSEM	0.8903	0.95
STYL-APSEM	0.8149	0.96	PPIAC-PPSEM	0.0218	0.99
STYL-PPSEM	1.7508	0.95	PPIAC-LIAC	0.1626	0.98
STYL-LIAC	1.6267	0.95	PPIAC-MIAC	0.3414	0.97
STYL-MIAC	1.4969	0.95	PPIAC-PAPE	0.1008	0.98
STYL-PAPE	0.9388	0.95	PPIAC-LAT	0.8785	0.96
STYL-LAT	0.9738	0.95	PPIAC-SPIPRO	0.8827	0.96
STYL-SPIPRO	0.8793	0.96	APSEM-PPSEM	1.2895	0.95
OVAL-CAR	0.8076	0.96	APSEM-LIAC	0.0869	0.98
OVAL-JUG	0.5320	0.97	APSEM-MIAC	0.6421	0.97
OVAL-SPIN	0.1998	0.98	APSEM-PAPE	0.5270	0.97
OVAL-SIG	0.3478	0.98	APSEM-LAT	1.7175	0.95
OVAL-AUR	0.6272	0.97	APSEM-SPIPRO	0.9094	0.95
OVAL-BAS	0.0342	0.98	PPSEM-LIAC	0.5033	0.97
OVAL-VAE	0.1364	0.98	PPSEM-MIAC	0.7731	0.97
OVAL-AIAC	0.3628	0.97	PPSEM-PAPE	0.9605	0.97
OVAL-PIAC	1.0938	0.96	PPSEM-LAT	0.8866	0.95
OVAL-AIE	0.8075	0.96	PPSEM-SPIPRO	0.8013	0.96
OVAL-PIE	0.8961	0.97	LIAC-MIAC	0.0647	0.98
OVAL-AEAM	0.9581	0.95	LIAC-PAPE	0.2185	0.98
OVAL-PEAM	0.7751	0.96	LIAC-LAT	0.1935	0.98
OVAL-APIAC	0.6421	0.97	LIAC-SPIPRO	1.0487	0.96
OVAL-PPIAC	0.2485	0.98	MIAC-PAPE	0.2144	0.98
OVAL-APSEM	0.1267	0.98	MIAC-LAT	0.1248	0.98
OVAL-PPSEM	0.9441	0.96	MIAC-SPIPRO	0.5487	0.97
OVAL-LIAC	0.8052	0.96	PAPE-LAT	0.5457	0.97
OVAL-MIAC	1.8569	0.95	PAPE-SPIPRO	0.0871	0.96
OVAL-PAPE	0.8454	0.96	LAT-SPIPRO	0.9871	0.96
OVAL-LAT	0.9487	0.96			

APPENDIX III

TABLE A-III. MULTIVARIATE GENERAL LINEAR MODEL RESULTS ILLUSTRATING INTERACTION BETWEEN SEX, AGE, AND DURATION

GLM Significance Values

Measurement	Sex	Age	Duration	Age by Sex	Sex by Duration	Age by Duration
MPSC-AIAC	0.7152	0.9114	0.5836	0.6014	0.8228	0.6310
STYM-CARO	0.9771	0.3517	0.5027	0.0965	0.7299	0.9880
STYM-MIAC	0.6851	0.7888	0.6567	0.4098	0.4256	0.7716
MPSC-PIE	0.1512	0.4493	0.7232	0.5630	0.2818	0.8177
LPSC-MIAC	0.7122	0.0943	0.8942	0.8420	0.4246	0.5932
COCH-SPIPRO	0.3957	0.0749	0.9055	0.4662	0.9488	0.7001
SIG-LAT	**0.0019**	0.0831	0.0784	0.4350	0.0646	0.3870
AUR-LAT	0.7201	0.1625	0.5390	0.8438	0.1900	0.9576
AUR-APIAC	**0.0034**	0.5938	0.4800	0.6489	0.8914	0.3612
PIAC-PAPE	**0.0029**	0.3675	0.0655	0.0880	0.2493	0.2224
APIAC-PAPE	**0.0013**	0.6372	0.2965	0.9519	0.5128	0.7907
PPIAC-LAT	**0.0034**	0.3029	0.6970	0.2683	0.0986	0.2457
SIG-PIAC	0.2144	0.4850	0.8084	0.3277	0.3869	0.4969
MPSC-LAT	**0.0017**	0.7508	0.8463	0.6165	0.9325	0.4085
LPSC-LAT	0.5172	0.7770	0.4305	0.1741	0.9637	0.5809
LSC-LAT	**0.0023**	0.7258	0.2535	0.1462	0.2412	0.5986
CARO-AUR	0.2929	0.0893	0.2788	0.0765	0.6540	0.2479
CARO-APIAC	**0.0078**	0.0794	0.1081	0.5899	0.0970	0.2036
CARO-MIAC	0.5241	0.1978	0.0889	0.4830	0.4453	0.0729
CARO-PAPE	0.3247	0.4686	0.2151	0.5282	0.2527	0.7290
CARO-LAT	**0.0315**	0.4338	0.8844	0.2569	0.9618	0.7123
AIE-PPIAC	**0.0127**	0.7583	0.7154	0.5037	0.2318	0.2372
AIE-APSEM	**0.0067**	0.1896	0.7113	0.4931	0.5367	0.2081
AIE-PPSEM	**0.0214**	0.0985	0.2193	0.4870	0.5934	0.1203
AIE-PAPE	**0.0171**	0.6806	0.6801	0.3011	0.2484	0.5530
AIE-LAT	**0.0097**	0.9178	0.0894	0.1963	0.6740	0.1545
LAT-SPIPRO	0.6154	0.2004	0.2673	0.4524	0.4091	0.5308
CLSC-VAE	0.2671	0.1432	0.3804	0.7113	0.4377	0.1070
SIG-APIAC	0.8741	0.4827	0.3893	0.9081	0.0934	0.1552
APSEM-PPSEM	**0.0031**	0.2161	0.0877	0.3749	0.1457	0.8425
PAPE-LAT	**0.0067**	0.3464	0.1664	0.2827	0.6105	0.3121
LSC COCH	0.0924	0.1429	0.1785	0.2804	0.0235	0.1829
LSC-AIE	0.1249	0.0974	0.0778	0.7451	0.9144	0.3789

Table A-III (Continued)

GLM Significance Values

Measurement	Sex	Age	Duration	Age by Sex	Sex by Duration	Age by Duration
LSC-LIAC	0.2144	0.8068	0.8627	0.3658	0.6768	0.3244
LSC-MIAC	0.1344	0.7663	0.3764	0.8580	0.1550	0.7732
LSC-PAPE	**0.0163**	0.9646	0.2337	0.1711	0.7543	0.7157
MPSC-STYM	0.4871	0.7257	0.1520	0.5030	0.5989	0.9927
MPSC-CARO	0.2148	0.4757	0.3212	0.6370	0.8248	0.8178
MPSC-JUG	0.3548	0.3487	0.8164	0.5766	0.6467	0.3812
MPSC-SPIPRO	0.2647	0.9132	0.4089	0.2100	0.2616	0.5498
MPSC-AIE	0.4657	0.9254	0.1288	0.7898	0.6251	0.3917
MPSC-PAPE	**0.0240**	0.2501	0.0651	0.2299	0.8937	0.7606
LPSC-VBLE	0.2315	0.8345	0.0958	0.6972	0.6620	0.1390
CLSC-COCH	0.6841	0.1816	0.8228	0.6835	0.5859	0.0627
CLSC-STYM	0.3545	0.5679	0.7401	0.4991	0.9655	0.0864
VBLE-AIAC	0.2346	0.5635	0.9362	0.5933	0.2059	0.4558
VBLE-PIAC	0.5123	0.9343	0.3202	0.4636	0.3302	0.6457
VBLE-AIE	0.1545	0.1251	0.1751	0.9222	0.8203	0.2202
VBLE-PIE	0.3541	0.5413	0.1780	0.6748	0.6079	0.2636
VBLE-SPIPRO	0.2678	0.1680	0.7461	0.2894	0.7361	0.3990
COCH-MID	0.4991	0.1646	0.3653	0.0828	0.4159	0.9045
COCH-STYM	0.2501	0.0998	0.0799	0.2459	0.5669	0.5112
COCH-VAE	0.0901	0.7164	0.1945	0.1924	0.9685	0.2444
MID-VAE	0.6592	0.4088	0.9193	0.1142	0.0764	0.0795
MID-AIAC	0.6168	0.4382	0.6994	0.4548	0.9256	0.8181
MID-PIAC	0.5833	0.7267	0.8351	0.9510	0.2781	0.4747
MID-AIE	0.3643	0.7712	0.0737	0.6648	0.1274	0.5728
MID-PIE	0.2282	0.0818	0.0878	0.7810	0.7122	0.4652
MID-MIAC	0.0809	0.3058	0.4218	0.7504	0.0754	0.0940
MID-PAPE	**0.0087**	0.6111	0.8301	0.9116	0.2618	0.6667
MID-LAT	**0.0031**	0.0737	0.5622	0.8421	0.7733	0.5606
MID-SPIPRO	0.6401	0.9659	0.0909	0.8241	0.0730	0.1858
STYL-SIG	0.5860	0.4727	0.2659	0.0698	0.0605	0.9038
STYL-AUR	0.0750	0.7332	0.4782	0.6972	0.0670	0.5380
STYL-VAE	0.5935	0.7706	0.4479	0.0991	0.8519	0.9273
STYL-AIAC	0.7565	0.8025	0.4220	0.5843	0.6352	0.9489
STYL-PIAC	0.8505	0.5295	0.4271	0.5409	0.8748	0.5764
CARO-VAE	0.4006	0.3639	0.7752	0.4844	0.7198	0.4512
SIG-LIAC	**0.0181**	0.7015	0.7068	0.8452	0.7080	0.0793
SIG-MIAC	0.6395	0.5174	0.3974	0.8461	0.5508	0.3051

Table A-III (Continued)

GLM Significance Values

Measurement	Sex	Age	Duration	Age by Sex	Sex by Duration	Age by Duration
SIG-PAPE	0.3790	0.7631	0.0913	0.0758	0.7945	0.0729
AUR-AIAC	0.0741	0.6025	0.6898	0.4838	0.7227	0.2586
AUR-PIAC	0.0978	0.3277	0.4565	0.4780	0.6309	0.6489
AUR-AIE	0.1541	0.6154	0.5238	0.5442	0.3709	0.7409
AUR-PIE	0.0951	0.7278	0.6915	0.1330	0.5237	0.0884
AIAC-PIAC	**0.0097**	0.8919	0.4424	0.4055	0.0787	0.9154
AIAC-PIE	0.0871	0.6384	0.6720	0.4561	0.9196	0.3364
PIAC-LIAC	**0.0312**	0.2193	0.0786	0.3950	0.7162	0.2863
PIAC-MIAC	**0.0211**	0.8238	0.1129	0.4811	0.6157	0.9465
PIAC-LAT	**0.0214**	0.9639	0.6598	0.2812	0.0936	0.9796
PIAC-SPIPRO	0.2576	0.3366	0.3006	0.7830	0.5393	0.7655

VITA

Name: Jason Matthew Wiersema

Address: Horizon Environmental Services, Inc., 2600 Dellana Lane, Suite 200 Austin, TX 78746

Email: jmwiersema@yahoo.com

Education: B.A., Anthropology, Texas State University, 1997
M.A., Anthropology, California State University, 2001
Ph.D., Anthropology, Texas A&M University, 2006